

Molecules in the Deep Interior of Giant Planets

Kumulative Dissertation
zur Erlangung des akademischen Grades
doctor rerum naturalium (Dr. rer. nat.)
der Mathematisch-Naturwissenschaftlichen Fakultät
der Universität Rostock

vorgelegt von
Armin Bergermann,
geb. am 16. Juli 1993 in Hagen

Rostock, den 09. Januar 2024

Gutachter:

Prof. Dr. Ronald Redmer

Institut für Physik, Universität Rostock

Prof. Roi Baer

Fritz Haber Center for Molecular Dynamics, Hebrew University of Jerusalem

Einreichung: 15.01.2024

Verteidigung: 19.04.2024

Adresse: Universität Rostock

Institut für Physik

18051 Rostock

Telefon: 0381 4986916

Internet: <http://www.physik.uni-rostock.de>

E-Mail des Autors: armin.bergemann@uni-rostock.de

Abstract

Exploring the properties of hydrogen, helium, nitrogen, and oxygen, and their mixtures, is a subject of considerable interest. While these elements are well understood under typical pressure and temperature conditions on Earth, their behaviour under the extreme pressure and temperature conditions relevant to giant planets remains unknown. This work addresses key aspects of this challenge.

The miscibility gap of hydrogen and helium is investigated through Monte-Carlo simulations using classical two-body interaction potentials. Predictions of the miscibility gap of hydrogen and water are made with classical Monte-Carlo methods and *ab initio* simulations. This comprehensive investigation sheds light on the interplay between hydrogen and water under extreme pressure and temperature conditions, offering insight in their miscibility gap.

Additionally, this research contributes to our understanding of nitrogen's equation of state using *ab initio* methods. The focus is on unravelling the details of the first-order liquid-liquid phase transition, coupled with a nonmetal-to-metal transition in nitrogen. The results of this analysis are discussed in depth, providing insights into the behaviour of nitrogen under extreme pressure and temperature conditions.

Kurzzusammenfassung

Die Erforschung der Eigenschaften von Wasserstoff, Helium, Stickstoff und Sauerstoff sowie ihrer Mischungen sind ein Thema von großem Interesse. Während diese Elemente unter typischen Druck- und Temperaturbedingungen auf der Erde gut verstanden sind, bleibt ihr Verhalten unter den extremen Druck- und Temperaturbedingungen, die für Riesenplaneten relevant sind, in großen Teilen unbekannt. Diese Arbeit befasst sich mit Schlüsselaspekten dieser Herausforderung.

Die Mischungslücke von Wasserstoff und Helium wird durch Monte-Carlo-Simulationen unter Verwendung klassischer Wechselwirkungspotentiale untersucht. Die Vorhersage der Mischungslücke von Wasserstoff und Wasser wurde mit zwei verschiedenen Ansätzen durchgeführt: klassischen Monte-Carlo-Methoden und *ab-initio*-Simulationen. Diese umfassende Untersuchung beleuchtet das komplexe Zusammenspiel von Wasserstoff und Wasser unter extremen Druck- und Temperaturbedingungen und liefert einen Fortschritt zum Verständnis ihrer Mischbarkeitslücke.

Darüber hinaus trägt diese Forschungsarbeit zu dem Verständnis der Zustandsgleichung von Stickstoff mithilfe von *Ab-initio*-Methoden bei. Der Schwerpunkt liegt auf der Analyse des Phasenübergangs erster Ordnung, welcher von einem Nichtmetall-zu-Metall-Übergang begleitet wird. Die Ergebnisse dieser Analyse werden ausführlich diskutiert und liefern wertvolle Einblicke in das einzigartige Verhalten von Stickstoff unter extremen Druck- und Temperaturbedingungen.

Contents

1. Introduction	1
1.1. Warm dense matter (WDM)	1
1.2. Ice- and gas giant planets	3
1.2.1. Planetary interiors	3
1.2.2. The role of binary mixtures and demixing in giant planets	4
1.3. Phase transitions	5
1.3.1. First-order phase transitions	6
1.3.2. Phase separation in binary mixtures	7
1.4. Outline of this thesis	9
2. Monte-Carlo (MC) simulations	10
2.1. MC simulations using the Metropolis algorithm	10
2.2. Gibbs-ensemble Monte-Carlo (GEMC) simulations	11
3. Density functional theory molecular dynamics (DFT-MD)	13
3.1. The many body Schrödinger equation	13
3.2. Born-Oppenheimer approximation	13
3.3. Density functional theory (DFT)	14
3.3.1. Kohn-Sham formalism for finite temperatures	15
3.3.2. Plane waves and pseudo potentials	17
3.3.3. Approximations for the exchange-correlation functional	18
3.4. Molecular dynamics (MD)	19
3.5. DFT-MD simulations with VASP	20
4. Additional theoretical methods	21
4.1. Nuclear quantum corrections (NQC)	21
4.2. Calculating the nonideal entropy	22
4.2.1. Coupling constant integration (CCI)	22
4.2.2. Numerical details	23
4.3. Electric conductivity from Kubo-Greenwood formalism	23
5. Results	25
5.1. Hydrogen and helium	25
5.2. Hydrogen and water	27
5.2.1. Miscibility gap calculated with the GEMC method	27
5.2.2. Miscibility gap calculated with <i>ab initio</i> methods	29
5.2.3. Comparison of the results	32
5.2.4. Impact on ice giant planets	33
5.3. Nitrogen	33

5.4. Summary and outlook	36
6. Publications	38
6.1. Gibbs-ensemble Monte Carlo simulation of H ₂ -He mixtures	38
6.2. Gibbs-ensemble Monte-Carlo simulation of H ₂ -H ₂ O mixtures	45
6.3. <i>Ab Initio</i> calculation of the miscibility diagram for hydrogen and water	53
6.4. Nonmetal-to-metal transition in dense fluid nitrogen at high pressure	64
A. Convergence	74
A.1. Convergence of the GEMC simulations for hydrogen and helium	74
A.2. Convergence of the DFT-MD simulations	75
A.2.1. Mixtures of hydrogen and water	75
A.2.2. Nitrogen	79
Bibliography	83
Curriculum vitae	97
Acknowledgments	100

Chapter 1.

Introduction

In recent years, significant advancements in the exploration of our solar system exploration, facilitated by enhanced observational capabilities and innovative modelling techniques, have greatly enriched our understanding of celestial bodies. However, this progress has also underscored the profound complexities and lingering mysteries that continue to fascinate the scientific community, see e.g. [1, 2, 3, 4]. Exploring planetary interiors has been interesting for scientists and space enthusiasts alike. Consider, for instance, the interior of Earth, where we uncovered vast reserves of minerals, intricate tectonic plate movements, and a molten outer core generating a protective magnetic field [5]. In the unforgiving desolation of space, our Moon carries the scars of ancient asteroid impacts, while Mars, with its desolate landscapes, raises questions about the possibility of past or present life [6]. Jupiter, the largest of them all, boasts a tumultuous atmosphere with raging storms that have persisted for centuries [7]. Saturn's majestic rings and enigmatic hexagonal cloud pattern at its north pole have confounded scientists [8]. Meanwhile, the ice giants Neptune and Uranus have their own secrets. Neptune, the windswept ice giant, harbours supersonic wind speeds and the Great Dark Spot, a storm system larger than Earth [9]. Uranus, known for its peculiar sideways rotation, challenges our understanding of planetary evolution [10].

Unfortunately, space missions are very costly and challenging and require decade-long preparations. Consequently, our understanding of the interior structures of planetary objects mostly depends on improving models by using the available observational constraints. Crucial physical quantities for characterizing the internal structure and evolution of planets include equations of state (EOS) and fundamental transport properties, such as conductivity, viscosity, and diffusivity. These properties govern the internal structure, thermal evolution, and magnetic fields and are essential for understanding the behaviour of planetary materials, see, e.g. [1, 11, 12, 13, 14, 15]. Hydrogen and helium, as the most abundant ones in the universe, play a crucial role in the composition of gas giant planets such as Jupiter and Saturn but also in ice giant planets such as Uranus and Neptune. However, heavier atoms, such as oxygen, nitrogen, carbon, and their mixtures, are also of great interest in this context.

1.1. Warm dense matter (WDM)

Warm dense matter (WDM) represents states comprising partially ionised atoms or partially dissociated molecules, typically manifesting as dense plasmas [21, 22]. However, WDM can also adopt solid-like [23] or superionic structures [24]. These states occur within a temperature range of 10^3 to 10^6 K and at densities spanning from 10^{-2} to 10^3 g/cm³ [18, 25]. To precisely delineate the WDM region in the density-temperature plane, we employ two essential parameters: the degeneracy parameter Θ (measuring the relevance of quantum mechanical degeneracy) and the coupling parameter Γ (measuring the relevance of correlation effects). The coupling parameter for a particle type a is determined as the ratio of Coulomb

energy, E_C , to thermal energy, E_{th}

$$\Gamma_a = \frac{E_C}{E_{th}} = \frac{q_a^2}{4\pi\epsilon_0 k_B T} \left(\frac{4\pi n_a}{3} \right)^{1/3}, \quad (1.1)$$

where q_a represents the charge, n_a is the density, ϵ_0 is the vacuum permittivity, k_B is the Boltzmann constant, and T is the temperature. The degeneracy parameter of the electrons is defined by the ratio of the thermal energy E_{th} to the Fermi energy E_F :

$$\Theta_e = \frac{E_{th}}{E_F} = \frac{8\pi\epsilon_0 k_B T}{e^2 a_B} \left(\frac{1}{3\pi^2 n_e} \right)^{2/3}, \quad (1.2)$$

where a_B denotes the Bohr radius and n_e is the electron density.

Using these parameters, one can distinguish between:

$$\Gamma_a \geq 1 \begin{cases} \text{strongly coupled (nonideal) plasmas} \\ \text{weakly coupled (ideal) plasmas} \end{cases} \quad (1.3)$$

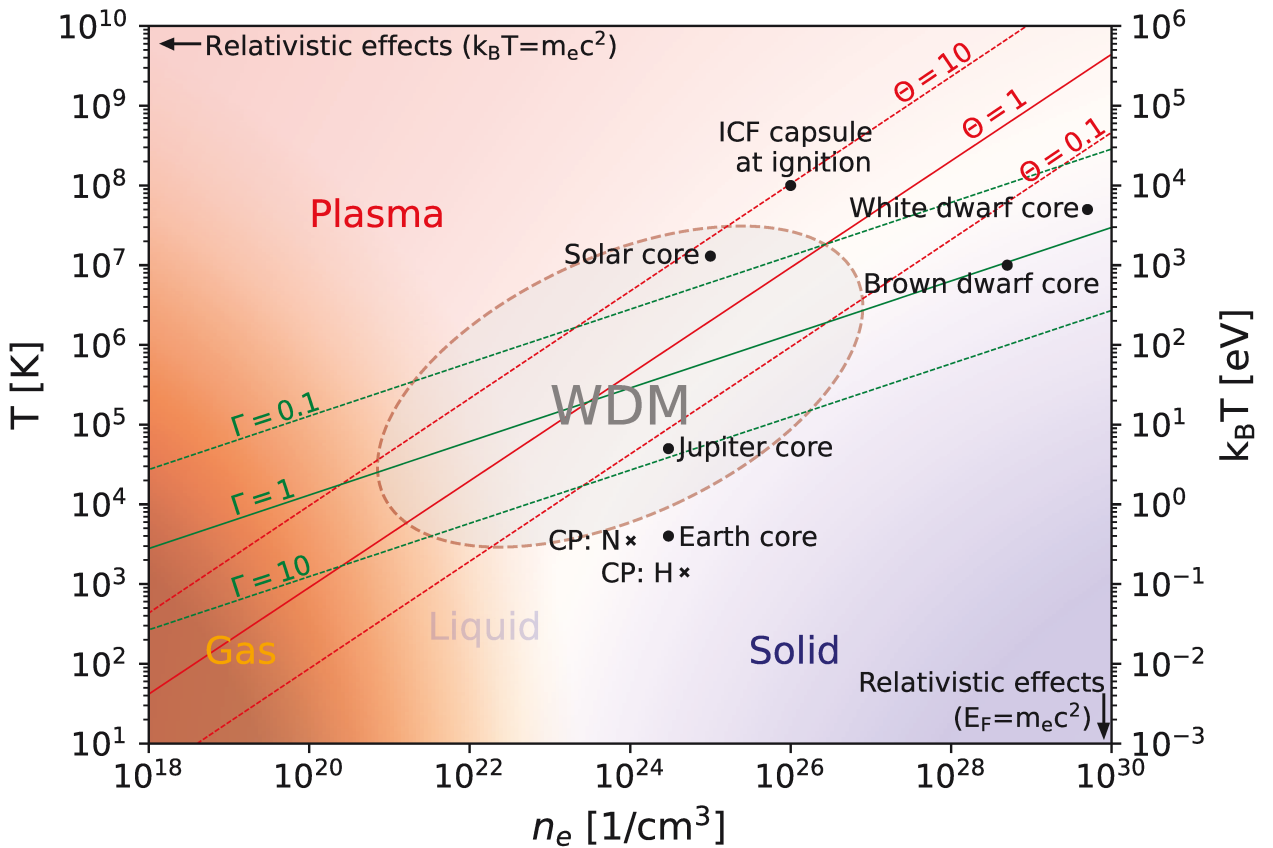


Fig. 1.1.: Non-relativistic electron density and temperature plane of plasmas. The density and temperature conditions relevant for WDM are marked by the grey shaded area. Conditions are characterized by the degeneracy (Θ) and coupling (Γ) parameters. Relevant conditions for inertial confinement fusion (ICF) [16, 17], relativistic effects [18], and some astrophysical objects [18] are indicated by black circles. The critical points (CP) of the first-order liquid-liquid phase transition in hydrogen [19] and nitrogen [20] are depicted by black crosses.

$$\Theta_e \geq 1 \begin{cases} \text{classical plasmas} \\ \text{degenerate plasmas} \end{cases} \quad (1.4)$$

The theoretical description of WDM is done using methods from many-body physics. Among the most popular choices is density functional theory molecular dynamics (DFT-MD) simulations using the Kohn-Sham formulation of DFT, as discussed in Sec. 3. Other post-Hartree-Fock methods such as Coupled Cluster theory [26], the configuration interaction method [27], or path integral Monte Carlo simulations [28, 29, 30] offer high accuracy. However, their computational cost often limits their application to the study of small systems [31].

As depicted in Fig. 1.1, many astrophysical objects, both within our solar system and beyond, are in the proximity of the WDM region [18, 25]. Additionally, practical applications extend to the creation of innovative materials [32, 33] and the execution of inertial confinement fusion, exemplified by facilities like the National Ignition Facility (NIF) where a breakthrough towards ignition has been achieved recently [17, 34, 35].

1.2. Ice- and gas giant planets

Ambitious space missions have been launched to investigate our solar system. Pioneering missions such as Voyager [2, 3] and Pioneer 11 [36], which ventured into the interstellar medium [37, 38], first reached the gas giant planets Saturn and Jupiter. Many more missions were launched to explore Jupiter and Saturn [39, 40, 41, 42], while Voyager 2 [3, 9] remains the only spacecraft which visited Neptune and Uranus. A new space mission to the ice giants might be launched in 2023 [43].

1.2.1. Planetary interiors

Saturn and Jupiter, the gas giants, are different in size, temperature, and density, but they are mainly made up of hydrogen and helium. Nevertheless, comprehending their interior remains a major scientific puzzle [4]. A uniform helium distribution inside these planets can not explain their thermal evolution and is in disagreement with the helium abundance in the outer atmosphere in these planets [12, 44]. More recent models consider an outer layer with a lowered helium value compared to the solar helium fraction and an inner layer rich in helium [12, 45, 46, 47]. Demixing of hydrogen and helium and subsequent helium rain could lead to such a compositional gradient [48, 49, 50, 51]. The core of these planets might carry a large amount of heavy elements mixing with the lighter elements of the middle layer, leading to the so-called core erosion [52, 53, 54].

The ice giant planets Uranus and Neptune are composed predominantly of hydrogen and heavier elements such as water, ammonia, methane, and rocky compounds [55]. However, their precise interior structure remains unknown [1, 14, 15]. A common class of planetary models propose three distinct layers: a rocky core, an inner layer rich in water, ammonia, and methane, and an outer layer rich in hydrogen and helium [1, 11, 56, 57, 58, 59]. Alternative models with a higher rock ratio are possible as well [1, 60]. In general, adiabatic interior models cannot explain the thermal evolution and very different brightnesses of Uranus and Neptune [10, 61], which hints towards more complex interior structures in ice giants [62].

1.2.2. The role of binary mixtures and demixing in giant planets

Understanding the interior dynamics of giant planets hinges on comprehending the role of binary mixtures, particularly those involving hydrogen and heavier elements such as helium and water.

In gas giants like Saturn and Jupiter, the demixing of hydrogen and helium plays a pivotal role. The effect of hydrogen and helium demixing has a profound impact on the interior structure models. These findings were strongly supported by studying the abundance of helium in their atmospheres, which revealed a eluviation in Saturn compared to the amount expected from the Sun's formation [63, 64, 65, 66]. As a result, Saturn has an outer layer primarily composed of hydrogen. The separation between hydrogen and helium leads to a phenomenon known as helium rain, where the gravitational energy released as helium droplets sink significantly boosts the planets' internal heat budgets [48]. Consequently, this process substantially retards the cooling of the planet, potentially explaining Saturn's unusually high luminosity [44, 45, 46, 67]. Moreover, the helium rain might lead to a diffuse, stably stratified core-envelope transition region extending to approximately 60% of the planet's radius [68].

Several theoretical and experimental studies have investigated the miscibility gap of hydrogen and helium [48, 49, 50, 51, 69, 70]. A schematic illustration of hydrogen and helium demixing inside gas giant planets is given in Fig. 1.2.

On the other hand, adiabatic models struggle to explain the thermal evolution and brightness of Uranus and Neptune. Partial immiscibility of hydrogen and water could lead to distinct layers forming in ice giants, inhibiting heat transport by convection between the hydrogen-rich outer layer and the water-rich inner layer [1, 56, 71, 72]. This process leads to a significantly hotter deep interior than assumed in the adiabatic case [58, 73, 74, 75]. However, current experimental studies [76, 77] and theoretical studies based on *ab initio* methods disagree on

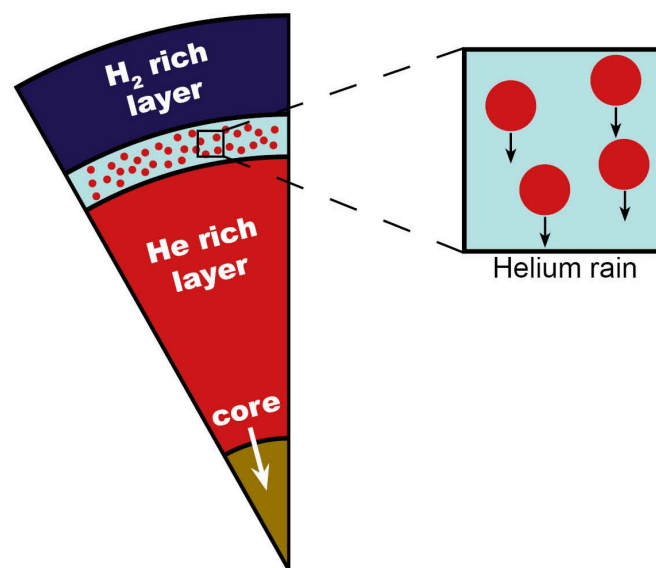


Fig. 1.2.: Schematic illustration of hydrogen and helium demixing in gas giant planets such as Saturn or Jupiter. The outer helium poor envelope is indicated in blue while the helium rich inner layer including the helium rain is indicated in red.

whether hydrogen and water are miscible under high pressure and temperature conditions as relevant for planetary interiors of ice giant planets.

1.3. Phase transitions

A phase is characterized as a region of uniform composition with distinct macroscopic properties and well-defined boundaries [78, 79, 80]. Classical examples include solid, liquid, and gaseous phases, depicted in phase diagrams based on variables such as p , T , and V [78]. Phase transitions manifest in diverse systems, spanning solid-liquid-gaseous transformations [81], structural changes in solids like fcc-hcp, bcc-fcc [82], and magnetic transitions such as para-diamagnetic shifts in iron [83]. Further examples encompass phase separation in liquids, such as the demixing of hydrogen and helium [49], nonmetal-to-metal transitions like the metalization of hydrogen [19], superfluidity in low-temperature liquid helium [84], and Bose-Einstein condensation in liquid helium [85]. Various theoretical models, such as the Ising model [86], Landau theory [87], Potts model [88], Ginzburg-Landau theory [89], XY model [90], and the Renormalization Group theory [91], have been developed to describe different types of phase transitions.

Exploring phase transitions under extreme conditions of high pressure and high temperature provides insight into the behavior of WDM, see, e.g. [17, 35, 92, 93]. This research is crucial for enhancing our understanding of objects such as the Earth's interior, gas giant interiors, and ice giant interiors [19, 49, 51, 69, 94]. Moreover, the study of phase transitions under extreme pressure and temperature conditions holds practical significance for various industrial processes and the development of cutting-edge materials [32, 95].

This work focuses is devoted to the intricacies of first-order liquid-liquid phase transitions and demixing in binary mixtures under high-pressure and high-temperature conditions.

The differential of the internal energy $U(S, V, N)$ is given as

$$dU = TdS - pdV. \quad (1.5)$$

Here, T denotes the temperature, p is the pressure, S the entropy, and V the volume. The most convenient thermodynamic potential for studying phase transitions is the free enthalpy [80, 96, 97] (also called Gibbs free energy) obtained through a Legendre transformation

$$G(T, p, N) = U - TS + pV. \quad (1.6)$$

Its differential is given by

$$dG = -SdT + Vdp + \mu dN, \quad (1.7)$$

where μ is the chemical potential, and N is the number of moles. Entropy, volume, and chemical potential can be calculated using derivatives of the free enthalpy

$$S = - \left(\frac{\partial G}{\partial T} \right)_{p,N}, \quad V = \left(\frac{\partial G}{\partial p} \right)_{T,N}, \quad \mu = \left(\frac{\partial G}{\partial N} \right)_{T,N}. \quad (1.8)$$

For our purpose it is convenient to use the free enthalpy per molecule given by

$$\frac{G}{N} = g = u + pv - Ts, \quad (1.9)$$

where u , v , and s are the internal energy, volume, and entropy per molecule, respectively, and p is the pressure.

1.3.1. First-order phase transitions

Phase transitions are often defined using the Ehrenfest classification [98]. A first-order phase transition is distinguished by the continuity of the free enthalpy at the transformation point, while the first derivative exhibits discontinuities and jumps [98]. In contrast, Fisher's definition characterizes higher-order phase transitions (also known as continuous phase transitions) by the continuity of the first derivatives of the free enthalpy, while the second derivatives at the transformation point are either discontinuous or divergent [99].

First-order phase transitions are characterized by latent heat, representing the energy absorbed or released by a substance or a thermodynamic system during a change of state while maintaining a constant temperature. At a first-order phase transition, two different phases can coexist, and the characteristics of these coexisting states can be calculated by performing Maxwell's equal area construction [80]. This graphical method involves plotting the pressure as a function of temperature for the two phases and constructing lines (tangents) with equal areas on each side of the coexistence curve. The intersection of these tangents indicates the coexistence conditions. At the critical point, the Gibbs free energy of the two coexisting phases is equal, resulting in identical chemical potentials, temperatures, and pressures for both phases [78].

A prominent example of a first-order phase transition is the transition of water from a liquid to a gas, see e.g. [78, 80]. If water reaches its boiling point, it undergoes a phase transition to water vapour. During this transition, water absorbs a significant amount of heat energy without a temperature change, as latent heat is absorbed. This process is reversible when the vapour condenses back into a liquid, releasing the same amount of heat.

Under high-pressure and high-temperature conditions, one of the most prominent examples of a first-order phase transition occurs in hydrogen [19, 30, 92, 100, 101, 102, 103, 104, 105]. This transition is characterized by a remarkable occurrence: the abrupt dissociation of hydrogen molecules alongside a transition from a nonmetallic state to a metallic one. A similar transition has also been observed in nitrogen, analysed in this work [20, 106, 107, 108, 109, 110, 111]. The phase diagram for nitrogen is illustrated in Fig. 1.3, with various models colour-coded to represent different predictions for the coexistence line. The transition pressures vary significantly between the models, underscoring the need for further investigations. Interestingly, the molecular system of oxygen does not show a first-order phase transition [112].

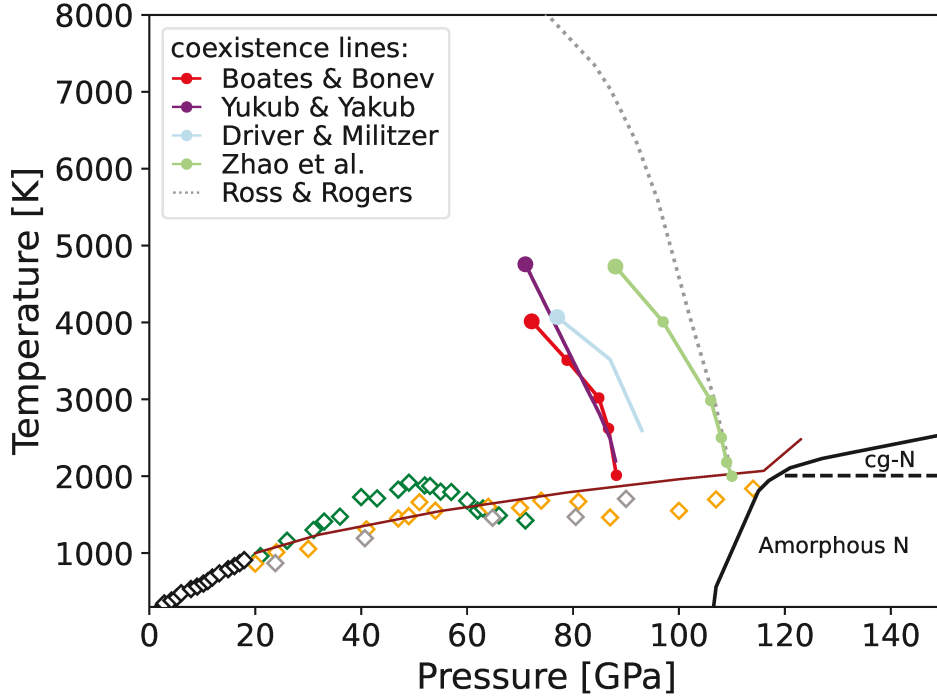


Fig. 1.3.: Phase diagram of nitrogen. The melting line is shown by diamonds: black [113], green [114], orange [115], gray [116] and a dark-red line [93]. Theoretical predictions for the first-order phase transition: Boates and Bonev [107] (red line), Yakub and Yakub [109] (purple line), Driver and Militzer [106] (light blue line), Zhao *et al.* [111] (green line). Experimental prediction for the first-order phase transition: Ross and Rogers [110] (grey dotted line).

1.3.2. Phase separation in binary mixtures

Phase separation lowers the overall free enthalpy by splitting the homogenous system into a weighted mix of two separate phases, each with lower free enthalpy than the starting homogeneous phase. A well-known example is a mixture of ethanol and water [78]. Under certain conditions, the mixture separates into two distinct phases: one rich in ethanol and the other rich in water.

For a mixture of two components, the condition of thermodynamic equilibrium means that the temperature T , the pressure p , the chemical potential μ_1 of component 1, and the μ_2 of component 2 must have the same value everywhere in the system. For subsystems A and B in coexistence, the condition of equilibrium is given by

$$T_A = T_B, \quad p_A = p_B, \quad \mu_{1A} = \mu_{1B}, \quad \text{and} \quad \mu_{2A} = \mu_{2B}. \quad (1.10)$$

Using Eqn. 1.9, the molecular mixture's free enthalpy is given by

$$\frac{G}{N_1 + N_2} = g = u + pv - Ts, \quad (1.11)$$

where $N = N_1 + N_2$ is the total number of molecules in the mixture. The free enthalpy of mixing per molecule is defined as

$$\Delta g(p, T, x_2) = g(p, T, x_2) - x_2 g(p, T, 1) - (1 - x_2) g(p, T, 0), \quad (1.12)$$

where $g(p, T, 1)$ is the free enthalpy of component 2, and $g(p, T, 0)$ is the free enthalpy of component 1. Note, that x_2 defines the molecular concentrations:

$$x_2 = \frac{N_2}{N_1 + N_2}. \quad (1.13)$$

To ascertain the thermodynamic stability of the homogeneous system, it is imperative to evaluate the second derivative of the free enthalpy. If the free enthalpy of mixing exhibits partial or complete concavity, characterized by

$$\frac{\partial^2 \Delta g}{\partial x_2^2} \leq 0, \quad (1.14)$$

the homogeneous system loses stability and undergoes partial or complete phase separation. As a result, equilibrium concentrations can be derived from Δg by constructing a common tangent [48]. The free enthalpy is illustrated for three different temperatures in Fig. 1.4. The black curve depicts a perfectly mixed system for arbitrary molecular concentration whereas the blue curve indicates partial immiscibility. The red curve depicts a system which is wholly immiscible. The dashed lines are the common tangent construction, while the crosses are the equilibrium concentrations. Note that the entropy increases with temperature, leading to a termination of demixing at higher temperatures. Accordingly, the black curve can be considered the highest temperature while the red curve is the lowest temperature [78], for a more detailed description of phase separation in binary mixtures see, e.g. [48, 78].

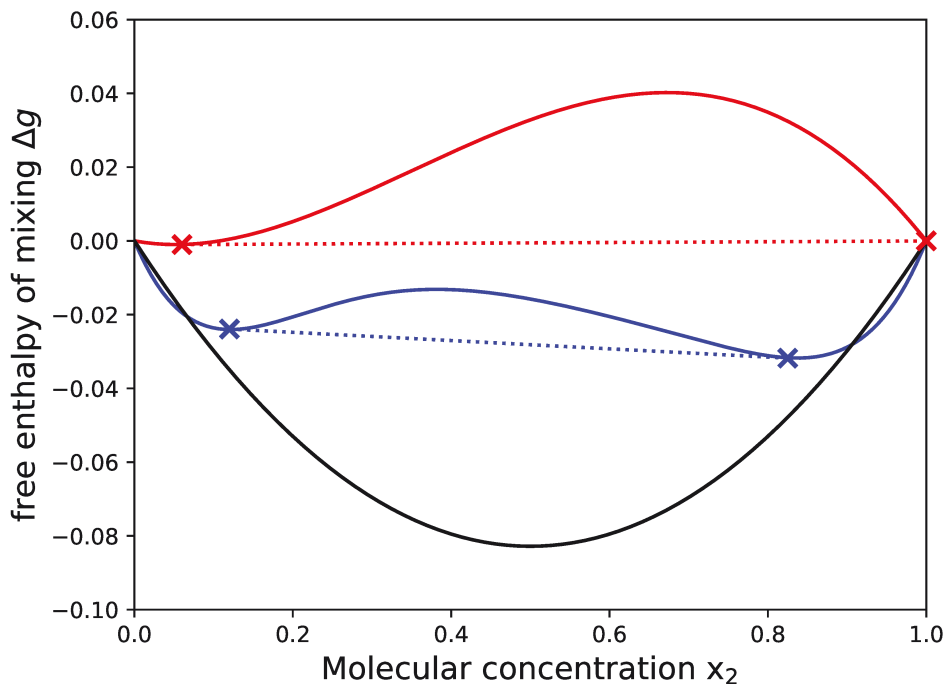


Fig. 1.4.: Free enthalpy of mixing for a binary mixture. The double tangent construction is shown by dotted lines, while the crosses indicate the equilibrium concentrations.

1.4. Outline of this thesis

The primary aim of this work is to investigate phase transitions in the WDM regime. The primary focus will be on binary mixtures of hydrogen with heavier elements such as helium and water, their miscibility gaps and impact on giant planets. To investigate these topics, we use theoretical methods such as *ab initio* methods or classical Monte Carlo simulations. Additionally, the first-order liquid-liquid phase transition of warm dense nitrogen is investigated, including the structural changes and its electrical conductivity.

In Chapter 2, the Monte-Carlo simulation method is outlined. First, the metropolis algorithm is explained in Sec. 2.1. Secondly, the Gibbs-ensemble Monte-Carlo method 2.2 is outlined, which is later used to calculate the miscibility gap of hydrogen mixed with either helium or water using analytical two-body interaction potentials. In Chapter 3 the theoretical concept of density functional theory molecular dynamics (DFT-MD) simulations is introduced. First, the many-body Schrödinger equation is discussed (Sec. 3.1) in light of the Born-Oppenheimer approximation (Sec. 3.2). Subsequently, the details of DFT simulations are discussed in Sec. 3.3. We explain the Kohn-Sham formalism for finite temperatures (Sec. 3.3.1), the approximations for the exchange-correlation functional (Sec. 3.3.3), the basics of molecular dynamic simulations (Sec. 3.4) and the used simulation code VASP (Sec. 3.5) including technical details of the code such as plane-waves and pseudopotentials (Sec. 3.3.2).

In Chapter 4 further numerical methods are explained, such as nuclear quantum corrections (Sec. 4.1), the coupling constant integration method (Sec. 4.2), and the Kubo-Greenwood formalism to calculate the electrical conductivity (Sec. 4.3).

Subsequently, Chapter 5 discusses the obtained results of this work: A prediction of the miscibility diagram of hydrogen and helium (Sec. 5.1), two predictions of the miscibility diagram of hydrogen and water (Sec. 5.2.1 and Sec. 5.2.2), its relevance for giant planets (Sec. 5.2.4), and a comparison to earlier results (Sec. 5.2.3). The first-order liquid-liquid phase transition in nitrogen (Sec. 5.3) is discussed. The publications are given in chapter 6. In addition, supporting information, such as convergence tests, is given in App. A.

Chapter 2.

Monte-Carlo (MC) simulations

Monte Carlo (MC) simulations, named after the Monte Carlo Casino in Monaco due to their reliance on random numbers [117], are invaluable tools across various fields for exploring complex systems, reducing uncertainty, and aiding in decision-making. For example, MC simulations provide a versatile and robust methodology for tackling the uncertainties inherent in financial markets [118]. One fundamental application of MC simulations is the estimation of mathematical constants such as π . This simulation involves generating random points within a known region and determining the fraction of points falling within a desired area. For instance, to approximate π , random points are generated within a square, and the ratio of points within a quarter-circle inscribed within that square to the total points generated provides an estimate of $\pi/4$. The accuracy of this method improves with the number of random points generated.

This work employs simulations in the canonical ensemble and Gibbs-ensemble Monte-Carlo (GEMC) simulations. The MC simulation method has been extensively documented in the literature. Consequently, this chapter aims to provide a concise overview of the techniques employed in this work. Comprehensive resources are available in review papers [118, 119] and various books [120, 121] for readers seeking a deeper understanding of this method.

2.1. MC simulations using the Metropolis algorithm

In 1953, Metropolis *et al.* [122] introduced the Metropolis MC algorithm, a foundational technique for generating trajectories in phase space to sample from a specified statistical ensemble. Understanding this algorithm is crucial for grasping the workings of MC simulations.

At its core, the Metropolis algorithm generates a Markov chain, enabling the sampling of system states according to a distribution proportional to the Boltzmann distribution. This Markov chain evolves sequentially, and each new state (denoted as x_{i+1}) is conditionally generated based on the previous state (x_i) and an acceptance-rejection criterion. Initially designed for two-dimensional systems and later extended to three dimensions, the algorithm considers a system with a finite number of N particles. The energy can be calculated using analytical two-body interaction potentials, such as the Lennard-Jones potential, many-body force fields, or *ab initio* methods.

The simulation begins by placing N particles on a simple cubic lattice. Subsequently, each particle is displaced incrementally, one by one, according to a set of rules. These rules dictate the new positions of the particles along the x , y , and z axes as follows:

- $X \rightarrow X + \alpha\zeta_1$,
- $Y \rightarrow Y + \alpha\zeta_2$,
- $Z \rightarrow Z + \alpha\zeta_3$.

Here, X , Y , and Z denote the particle positions, α represents the maximum allowed displacement, and ζ_i are random numbers sampled from the interval $[-1, 1]$. It is important to note that the particles are displaced with an equal probability within a cube with a side length of 2α around their original positions.

The critical step in the Metropolis algorithm is deciding whether to accept or reject the proposed displacement. The move is always accepted if the displacement results in a lower energy state ($\Delta E < 0$). However, if the energy increases ($\Delta E > 0$), the move is accepted with a probability \mathbb{P}_{PD} defined by

$$\mathbb{P}_{\text{PD}} = \min[1, \exp(-\beta\Delta E)], \quad (2.1)$$

where ΔE represents the change in energy and $\beta = 1/(k_{\text{B}}T)$. A random number ζ_4 is generated from the interval $[0, 1]$. If ζ_4 is less than $\exp(-\beta\Delta E)$, the particle's new position is accepted; otherwise, it remains unchanged. The Metropolis algorithm can be extended for rotational moves to deal with nonspherical molecules by employing spherical coordinates Θ and ϕ .

The number of particles in MC simulations is limited. Therefore, this work uses periodic boundary conditions and the minimum image convention [120, 121]. The pressure of such a system can be calculated using the virial theorem [123].

This simulation procedure is employed primarily in the canonical ensemble to calculate the EOS. In this work, the MC method plays a crucial role in determining the nonideal entropy using the coupling constant integration (CCI) method discussed in Sec. 4.2.

2.2. Gibbs-ensemble Monte-Carlo (GEMC) simulations

The GEMC simulation method is a simple extension of the Monte Carlo simulation technique described in Sec. 2.1. Developed in 1987 by Panagiotopoulos *et al.* [124, 125, 126], and comprehensively reviewed by Zhang *et al.* [127], this method involves two simulation boxes, denoted as Box *I* and Box *II*, sharing the same external pressure p and temperature T but differing in volumes V_I and V_{II} . Box *I* contains N_I^A and N_I^B particles of types *A* and *B*, while Box *II* contains N_{II}^A and N_{II}^B particles. The total number of particles is conserved, resulting in $N^A = N_I^A + N_{II}^A$ and $N^B = N_I^B + N_{II}^B$.

A schematic overview of a simulation cycle is provided in Fig. 2.1. First, particle displacements are attempted independently in both boxes. For polar fluids, particle displacements or rotations are chosen with equal probabilities of 50%. The order of displacement and rotation steps is randomly selected. The acceptance probability for such a step is given in Eq. 2.1.

Secondly, both boxes experience volume changes to maintain the average pressure constant. The acceptance probability is given by

$$\mathbb{P}_{\text{VC}} = \min\left[1, \exp\left(-\left(\beta\Delta E - N \ln \frac{V + \Delta V}{V} + \beta p \Delta V\right)\right)\right], \quad (2.2)$$

where ΔV represents the change in volume.

Thirdly, particle transfers and swaps are attempted. In the case of particle transfers, a particle is randomly selected and moved from Box *I* to Box *II* or vice versa by randomly choosing a new position and orientation. A particle swap involves the transfer of two particles

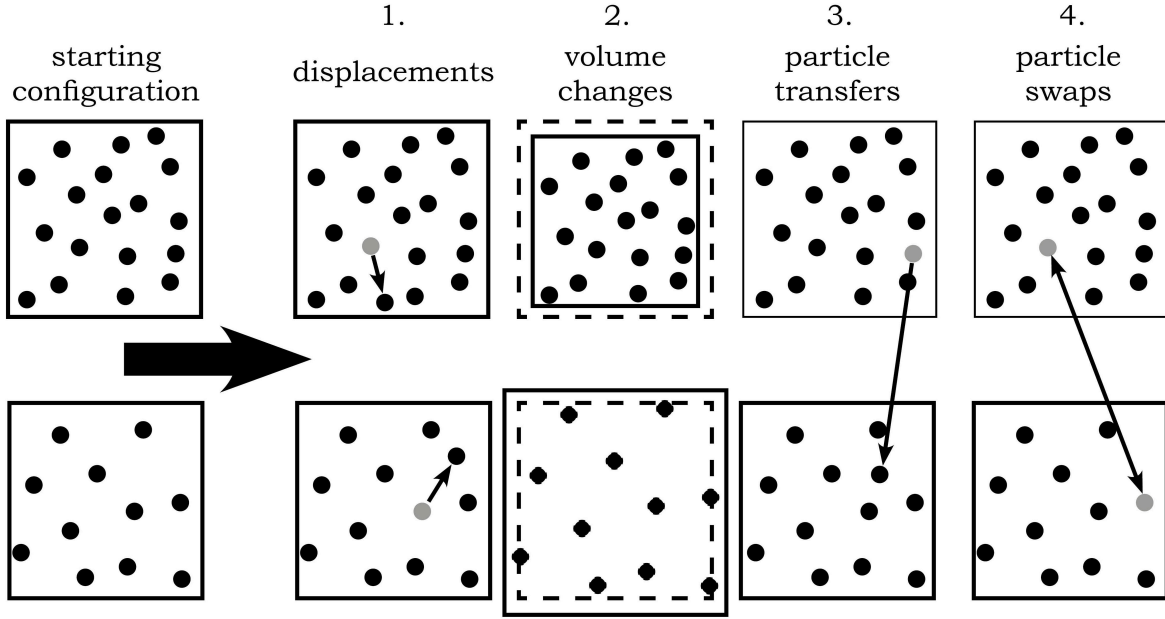


Fig. 2.1.: Schematic workflow of a Gibbs-ensemble Monte Carlo simulation [128].

of different species between the two boxes, with no change in particle positions. The species and the boxes are chosen with equal probabilities of 50%, while the specific particles to be swapped are selected randomly. The acceptance probability for a particle transfer is given by

$$\mathbb{P}_{\text{PT}} = \min \left[1, \exp \left(-\beta \left(\Delta E_I + \Delta E_{II} + \frac{1}{\beta} \ln \frac{V_{II}(N_I^A + 1)}{V_I N_{II}^A} \right) \right) \right], \quad (2.3)$$

where $\Delta E_I = E_{I,\text{new}} - E_{I,\text{old}}$, and $\Delta E_{II} = E_{II,\text{new}} - E_{II,\text{old}}$. The acceptance probability for a swap is given by

$$\mathbb{P}_{\text{PS}} = \min \left[1, \exp \left(-\beta \left(\Delta E_I + \Delta E_{II} + \frac{1}{\beta} \ln \frac{V_{II}(N_I^A + 1)}{V_I N_{II}^A} + \frac{1}{\beta} \ln \frac{V_I(N_{II}^B + 1)}{V_{II} N_I^B} \right) \right) \right]. \quad (2.4)$$

This simulation technique ensures that the difference in the chemical potentials is $\Delta\mu = \mu_I - \mu_{II} = 0$. Note that the absolute value of the chemical potential remains undetermined [121]; thus, the GEMC method circumvents its calculation.

The GEMC method is versatile and applicable not only to investigate phase transitions in single-component systems, like the liquid-vapor transition in sodium [129] but also to explore miscibility gaps in binary mixtures. For instance, in 1991, Schouten *et al.* [130] utilized this approach to study the miscibility gap between hydrogen and helium.

Throughout this study, we conducted a comprehensive series of convergence tests to ensure particle number convergence. Additional details are available in App. A.1.

Chapter 3.

Density functional theory molecular dynamics (DFT-MD)

In case of degeneracy in the plasma, a full quantum mechanical description becomes imperative and predictions of perturbation theory becomes increasingly questionable. This work employs density functional theory molecular dynamics (DFT-MD) simulations using the Kohn-Sham formulation of DFT.

3.1. The many body Schrödinger equation

The time-dependent Schrödinger equation is a fundamental equation in quantum mechanics that describes the time evolution and properties of a nonrelativistic many-particle system [131]. The corresponding Hamiltonian \hat{H} reads as

$$\hat{H} = \hat{T}_e + \hat{V}_{ee} + \hat{V}_{ne} + \hat{T}_i + \hat{V}_{ii}, \quad (3.1)$$

where \hat{T}_e is the kinetic energy operator of the electrons, \hat{V}_{ee} is the electron-electron repulsion energy operator, \hat{V}_{ne} is the electron-nucleus attraction energy operator, \hat{T}_i is the kinetic energy operator of the nuclei, and \hat{V}_{ii} is the nucleus-nucleus repulsion operator. However, analytically solving this equation for systems with a large number of particles is infeasible, limiting its practical application to only a few particles [132]. The Hartree-Fock method [133], a foundational approach in quantum chemistry, has historically been instrumental in studying electronic structure for many-body systems, preceding more advanced methods such as path integral Monte Carlo (PIMD) simulations. PIMD simulations are powerful computational methods that can solve the many-body Schrödinger equation, providing accurate results [28, 29, 134]. However, their applicability is constrained due to the computational challenges when dealing with larger systems [31]. DFT has emerged as a very successful alternative computational approach in many fields such as physics, chemistry, and material science [135]. DFT methods focus on the electron density rather than the wave function, enabling the study of complex many-body systems with improved computational efficiency and practicality. Other post Hartree-Fock methods, such as the Coupled Cluster theory or the configuration interaction method [26], offer high accuracy in capturing electron correlation effects; however, their computational cost makes them infeasible for studying the dynamics of larger systems. In this work, computational efficiency is a crucial factor. Therefore, DFT is the preferred choice, allowing us to explore larger and more complex systems of hundreds of atoms in the WDM regime while still achieving meaningful results.

3.2. Born-Oppenheimer approximation

In this work, the Born-Oppenheimer approximation [136] is employed. This approximation, grounded on the assumption that electrons are significantly lighter than nuclei, effectively

decouples the electronic system from the nuclei, treating the nuclear motion as stationary. As a consequence, the electronic wave function depends only on the fixed nuclear positions, enabling the determination of the electronic energy and wave function for a given nuclear configuration. The reduced stationary Schrödinger equation for a system consisting of N -nuclei with coordinates $\{\mathbf{R}_I\}$ and N_e electrons with coordinates $\{\mathbf{r}_i\}$ can be written as

$$\hat{H}_e \phi_m(\{\mathbf{r}_i\}, \{\mathbf{R}_I\}) = E_m(\{\mathbf{R}_I\}) \phi_m(\{\mathbf{r}_i\}, \{\mathbf{R}_I\}), \quad (3.2)$$

where E_m is the eigenvalue of state m depending only parametrically on $\{\mathbf{R}_I\}$ and $\phi_k(\{\mathbf{r}_i\}, \{\mathbf{R}_I\})$ is the electronic wave function. The electronic Hamiltonian \hat{H}_e is given by

$$\hat{H}_e = \hat{T}_e + \hat{V}_{ne} + \hat{V}_{ee}. \quad (3.3)$$

It is worth noting that \hat{H}_e differs from that in the Schrödinger equation (equation. 3.1) as it does not include the kinetic energy operator of the nuclei or the nuclei-nuclei repulsion operator. This separation allows for the independent treatment of the nuclei and electronic contributions within the system. By disregarding all quantum effects in the motion of the nuclei, classical equations of motion for the nucleus are derived [120] follows to

$$m_I \frac{d^2}{dt^2} \mathbf{R}_I = \mathbf{F}_{I,nn} + \mathbf{F}_{I,ne}, \quad (3.4)$$

where $\mathbf{F}_{I,nn}$ is the Coulomb force between the nuclei and $\mathbf{F}_{I,ne}$ are the forces between the electrons and the nuclei calculated using the Hellmann-Feynman theorem [137, 138]. This decoupling allows to treat the electronic and ionic subsystem separately.

Coupling density functional theory with molecular dynamics (DFT-MD), proposed by Car-Parrinello [139], provides a powerful computational framework for studying complex many-body systems. This work uses the DFT-MD method to treat many-particle systems effectively in the WDM regime. First, density functional theory is used to calculate the electronic energies by solving Eqn. (3.2). Secondly, a molecular dynamics (MD) simulation for the nucleus is used, but with forces that are directly obtained from the quantum mechanical calculation of the electron system at each time step. Concluding, it combines the efficiency of DFT in capturing electronic structure with classical molecular dynamics to simulate the dynamics of the nuclei. The DFT-MD method approach enables the investigation of a wide range of systems, from light atoms such as hydrogen to complex molecules. In the subsequent sections, the main ideas of DFT and MD are outlined briefly. Readers interested in delving deeper into the DFT method might be referred to a plethora of books [135, 140, 141, 142, 143] and review articles [132, 144, 145, 146, 147, 148, 149]. Likewise, various books give details on the numerical concepts of MD [120, 121, 150, 151], being a long-established standard method for the numerical description of many-body systems.

3.3. Density functional theory (DFT)

In the following, we explore the unique theory of density functional theory (DFT), which simplifies the description of quantum systems by replacing the cumbersome N -electron wave function $\Psi(\{\mathbf{q}_k, \sigma_k\}; t)$, where σ_k represents spin and \mathbf{q}_k are the three-dimensional spatial coordinates of each particle k at all points in time t . The electron density $\rho(\mathbf{r})$, observed in X-ray diffraction experiments and readily visualised, serves as a three-dimensional single-particle

distribution function and can describe the quantum behaviour of ground states. The electron density is given by

$$\rho(\mathbf{r}) = N_e \int \dots \int d^3r_2 \dots d^3r_{N_e} |\phi_m(\{\mathbf{r}_i\})|^2, \quad (3.5)$$

where $\phi_m(\mathbf{r}_i)$ represents the electronic wave function and is normalized to the number of electrons N_e

$$\int d^3r \rho(\mathbf{r}) = N_e. \quad (3.6)$$

The concept of electron density has received considerable attention over the years [152]. In 1927, Thomas and Fermi proposed an approximate model by assuming an average electron density distribution around the nuclei.

uniform electron distribution within an atom. However, this primitive method fails to describe molecular binding accurately and lacks precision for atoms. The situation changed significantly with the milestone publication by Hohenberg and Kohn [153]. They provided two fundamental theorems:

1. The external potential \hat{V}_{ne} (except for a constant) is a unique functional of the electron density $\rho(\mathbf{r})$. Consequently, since \hat{V}_{ne} determines the electronic Hamiltonian, $\hat{H}_e = \hat{T}_e + \hat{V}_{ne} + \hat{V}_{ee}$, the many-particle ground state is a unique functional of $\rho(\mathbf{r})$.
2. The Hohenberg-Kohn functional, $J_{HK}[\tilde{\rho}(\mathbf{r})] = T_e[\tilde{\rho}(\mathbf{r})] + E_{ee}[\tilde{\rho}(\mathbf{r})]$, yields the ground state energy, if and only if the electron density $\tilde{\rho}(\mathbf{r})$ is the true electron density $\rho(\mathbf{r})$.

The first theorem legitimizes the use of electron density as the fundamental variable, while the second Hohenberg-Kohn theorem provides the variational principle. The simplicity of proving these theorems is well-documented in related textbooks. In conclusion, $\rho(\mathbf{r})$ determines the number of electrons N and the external potential V_{ne} , thereby capturing all properties of the ground state. The energy as a functional of the density can be expressed as

$$E[\rho] = T_e[\rho] + V_{ne}[\rho] + V_{ee}[\rho] = V_{ne}[\rho] + J_{HK}[\rho], \quad (3.7)$$

where $J_{HK}[\rho]$ is the so-called Hohenberg-Kohn functional. Unfortunately, the explicit form of the energy functional is unknown, which makes direct minimization infeasible. However, Kohn and Sham [154] ingeniously reformulated the electronic problem in 1965, presenting an efficient scheme suitable for computer simulations.

3.3.1. Kohn-Sham formalism for finite temperatures

DFT provides a practical computational scheme known as the Kohn-Sham equations [154], akin to the Hartree-Fock equations, but with the inclusion of both exchange and correlation effects. Conceived initially as a ground-state theory, DFT was extended to finite temperatures by Mermin [155] shortly after Hohenberg and Kohn [153] introduced their foundational ideas. This extension introduces the free energy as the quantity to be minimized, represented by

$$F[\rho] = E[\rho] - TS[\rho]. \quad (3.8)$$

Hohenberg and Sham introduced a corresponding noninteracting reference system with the Hamiltonian [144]

$$\hat{H}_s = \hat{T}_s + \hat{V}_s, \quad (3.9)$$

where the subscript s denotes the reference system. In this reference system, \hat{T}_s represents the kinetic energy operator, and \hat{V}_s represents the potential energy operator, with no electron-electron repulsion terms in the Hamiltonian. The associated electron density for this noninteracting reference system is defined as

$$\rho(\mathbf{r}) = \sum_{i=1}^{\infty} f(\epsilon_i) |\phi_i(\mathbf{r})|^2, \quad (3.10)$$

where electrons occupy single-particle eigenstates based on Fermi-Dirac statistics [144]. Here, $\phi_i(\mathbf{r})$ represents the Kohn-Sham orbitals, elements of the Slater determinant, each associated with an eigenenergy ϵ_i . In this context, Kohn-Sham orbitals describe a wave function that precisely represents N noninteracting electrons. The Fermi-function, $f(\epsilon_i)$, is given by

$$f(\epsilon_i) = \frac{1}{e^{(\epsilon_i - \mu_e)/k_B T} + 1}, \quad (3.11)$$

where μ_e is the chemical potential. The kinetic energy of this noninteracting reference system, defined using Kohn-Sham orbitals, is

$$T_s = -\frac{\hbar^2}{2m_e} \sum_{i=1}^{\infty} f(\epsilon_i) \int d^3r \phi_i(\mathbf{r}) \nabla_i^2 \phi_i(\mathbf{r}), \quad (3.12)$$

while the entropy is given by

$$S_s = -k_B \sum_{i=1}^{\infty} [f(\epsilon_i) \ln(f(\epsilon_i)) + (1 - f(\epsilon_i)) \ln(1 - f(\epsilon_i))]. \quad (3.13)$$

Although T_s and S_s are uniquely defined for any density, they do not represent the exact kinetic-energy functional $T_e[\rho]$ and entropy functional $S[\rho]$. The free energy functional can then be expressed as

$$F[\rho] = T_s[\rho] + J[\rho] + E_{en}[\rho] - TS_s[\rho] + E_{xc}[\rho], \quad (3.14)$$

where $J[\rho]$ represents the well-known Hartree energy term, and the so-called exchange-correlation energy $E_{xc}[\rho]$ encompasses the differences between $T_e[\rho]$ and T_s , $S[\rho]$ and S_s , and the nonclassical part of $V_{ee}[\rho]$. Thus, the exchange-correlation free energy is defined as

$$F_{xc}[\rho] = (T_e[\rho] - T_s[\rho]) - (TS_e[\rho] + TS_s[\rho]) + E_{ee}[\rho] - J[\rho]. \quad (3.15)$$

The Hartree energy term, $J[\rho]$, is given by

$$J[\rho] = J[\rho(\mathbf{r})] = \frac{1}{2} \frac{e^2}{4\pi\epsilon_0} \int \int d^3r d^3r' \frac{\rho(\mathbf{r})\rho(\mathbf{r}')}{|\mathbf{r} - \mathbf{r}'|}, \quad (3.16)$$

while the external energy is defined as

$$E_{en}[\rho] = E_{en}[\rho(\mathbf{r})] = - \sum_{I=1}^{N_n} \frac{Z_a e^2}{4\pi\epsilon_0} \int d^3r \frac{\rho(\mathbf{r})}{|\mathbf{r} - \mathbf{R}_I|}, \quad (3.17)$$

where e is the elementary charge, m is the electron mass, ϵ_0 is the vacuum permittivity, and Z_a the charge number of the nuclei. The Kohn-Sham equations are derived from the variational principle, which seeks to find the electronic wave functions that minimize the total energy functional by considering the normalisation. Hence, a system of noninteracting electrons moving in a local potential $v_{eff}(\mathbf{r})$ is given by

$$v_{eff}(\mathbf{r}) = \frac{e^2}{4\pi\epsilon_0} \int d^3r' \frac{\rho(\mathbf{r}')}{|\mathbf{r} - \mathbf{r}'|} - \sum_{I=1}^{N_n} \frac{Z_a e^2}{4\pi\epsilon_0} \frac{1}{|\mathbf{r} - \mathbf{R}_I|} + \frac{\delta F_{xc}[\rho(\mathbf{r})]}{\delta \rho(\mathbf{r}')}. \quad (3.18)$$

Accordingly, the interacting and the noninteracting system agree in an effective potential. The eigenfunctions and eigenvalues are obtained from the finite-temperature Kohn-Sham equations, given by

$$\left[- \frac{\hbar^2}{2m_e} \nabla^2 + v_{eff}(\mathbf{r}) \right] \phi_i(\mathbf{r}) = \epsilon_i \phi_i(\mathbf{r}), \quad (3.19)$$

which result in the electron density as given by Eq. 3.10. The choice of orbitals to solve the Kohn-Sham equations is determined self-consistently based on the minimization of the free energy. Note, that the eigenenergies ϵ_i represent the Lagrange parameters.

It's important to note that Kohn-Sham theory, while exact in principle, distinguishes itself from the approximate Hartree-Fock theory by its ability to fully incorporate the exchange-correlation effects of electrons.

3.3.2. Plane waves and pseudo potentials

Two different major methodologies exist to expand of the basis set in modern DFT codes. One can use local orbital basis sets like those implemented in SIESTA [156] and FHI-aims [157] or employ a plane-wave basis set. The latter is used by VASP [158], and other codes such as Quantum Espresso [159], Abinit [160], or CASTEP [161]. The Bloch theorem [162] connects the properties of the electrons in a system with periodic boundary conditions to those of the electrons in the unit cell [143]. Expressing the Kohn-sham orbitals by Bloch functions it follows

$$\Phi_i(\mathbf{r}, \mathbf{k}) = u_i(\mathbf{r}, \mathbf{k}) e^{i\mathbf{k} \cdot \mathbf{r}}, \quad (3.20)$$

where \mathbf{k} is a vector in the first Brillouin zone and the index i runs over all states. By expanding the periodic wave functions $u_i(\mathbf{r}, \mathbf{k})$ in the plane wave basis the Kohn-Sham orbitals can be expressed as

$$\Phi_i(\mathbf{r}) = \frac{1}{\sqrt{V}} u_i(\mathbf{r}, \mathbf{k}) e^{i\mathbf{k}\mathbf{r}} = \frac{1}{\sqrt{V}} \sum_{\mathbf{G}=0}^{\infty} C_i(\mathbf{G}, \mathbf{k}) e^{i(\mathbf{k}+\mathbf{G})\mathbf{r}} \quad (3.21)$$

where \mathbf{G} is the reciprocal lattice vector, and $C_i(\mathbf{G}, \mathbf{k})$ are the complex Fourier expansion coefficients [143, 150, 163]. In practice, the infinite sum over \mathbf{G} is truncated once the

pre-defined energy cutoff is exceeded

$$E_{cut} > \frac{\hbar^2}{2m_e} |\mathbf{k} + \mathbf{G}|^2. \quad (3.22)$$

To calculate properties such as electron density and energy, integration over the wave vectors \mathbf{k} in the first Brillouin zone is required [150]. It is, however, possible to choose special integration points such that the integration over \mathbf{k} space reduces to a weighted sum over a few discrete \mathbf{k} points [150, 163]. This work employs the Balderschi mean value point [164] and the scheme of Monkhorst-Pack [165].

Describing the wave function only with plane waves is a hopeless task due to the heavily oscillating nature of the wave function near the core, which necessitates an infinite number of plane waves [143, 150]. Pseudopotentials are used to overcome this problem. The basic idea is that the core electrons of an atom are tightly bound and not directly involved in chemical bonding or many electronic properties of interest. Therefore, they can be replaced by an effective potential that replaces the wave function in a radius r_c around the nucleus with a smooth wave function. Therefore, the pre-defined energy cutoff E_{cut} can be reduced significantly. This work utilises PAW (Projected Augmented-Wave) pseudopotentials, which combine elements of all-electron methods and traditional pseudopotentials. The PAW approach connects the wave function to the pseudo wave function through projection operators [166, 167].

3.3.3. Approximations for the exchange-correlation functional

As explained in the previous sections, DFT offers a practical computational scheme known as the Kohn-Sham equations. While these equations precisely incorporate the kinetic energy term $T_s[\rho]$, they leave the exchange-correlation functional F_{xc} undetermined. Over the past four decades, many of approximations have been developed and categorized into different classes of functionals [135, 143, 168]. The functional choice depends on the specific physical problem, with simpler or more complex functionals selected accordingly. However, it is essential to note that increased complexity often translates to longer computational times.

In thermal DFT, a common practice is to approximate the free energy exchange and correlation functional as $F_{xc} \approx E_{xc}$ from ground state DFT, effectively neglecting part of the temperature effects [55, 62, 169]. This approach persisted because explicitly temperature-dependent functionals were not available for an extended period and had only recently received more attention [170, 171, 172, 173, 174]. Nevertheless, popular ground state functionals like PBE, SCAN, or HSE have proven to describe the thermodynamic properties of warm dense matter accurately in many comparisons with experiments [175, 176, 177, 178].

The simplest approximation is the local-density approximation (LDA) for exchange and correlation energy

$$E_{xc}^{LDA}[\rho] = \int \rho(\mathbf{r}) \epsilon_{xc} d\mathbf{r}, \quad (3.23)$$

where ϵ_{xc} represents the exchange and correlation energy per particle of a uniform electron gas of density $\rho(\mathbf{r})$ [144]. We expand the density in terms of gradients and higher-order derivatives to address inhomogeneities in electron density. The generalized gradient approximation (GGA), including the density ρ and its gradient $\nabla\rho$, accounts for the non-homogeneity of

the true electron density. In this work, the Perdew, Burke, and Ernzerhof (PBE) functional is employed [179]. Although the meta-GGA functionals like the SCAN-functional [180] incorporate additional semi-local information via the Laplacian of the density $\nabla^2\rho$, they are significantly more computationally expensive and are not used in this work.

LDA, PBE, and SCAN functionals are locally defined, meaning information about the density $\rho(\mathbf{r})$ and its derivatives $\nabla\rho(\mathbf{r})$ is independent of properties of $\rho(\mathbf{r}')$ at points $\mathbf{r} \neq \mathbf{r}'$ [135]. These functionals tend to underestimate band gaps significantly [181]. Hybrid functionals were developed to overcome this limitation, combining a portion of exact exchange from Hartree-Fock theory for short distances with the density functional exchange-correlation [135]. In this work, the Heyd, Scuseria, and Ernzerhof (HSE) functional is used [178, 181, 182, 183], which incorporates a fraction of the exact exchange with the PBE-functional as follows

$$E_{\text{XC}}^{\omega\text{PBEh}} = aE_{\text{x}}^{\text{HF,SR}}(\omega) + (1-a)E_{\text{x}}^{\text{PBE,SR}}(\omega) + E_{\text{x}}^{\text{PBE,LR}}(\omega) + E_{\text{c}}^{\text{PBE}}, \quad (3.24)$$

where the half-empirical parameters $a = 0.25$ is a mixing parameter and $\omega = 0.2$ controls the short-rangeness of the interaction. Note that the short-range exchange energy is determined by 25% by the short-range Hartree-Fock exact exchange functional ($E_{\text{x}}^{\text{HF,SR}}(\omega)$) and to 75% by the PBE-exchange energy $E_{\text{x}}^{\text{PBE,SR}}(\omega)$ part. This work uses the hybrid functional to calculate the conductivity in liquid nitrogen. For the study on the conductivity in liquid nitrogen, HSE proves to be the optimal choice [177].

3.4. Molecular dynamics (MD)

Molecular dynamics (MD) simulation [184, 185] is a widely used computational technique that provides valuable insights into the dynamic behaviour of atoms and molecules over time. In this section, we focus on MD simulations where movements of nuclei are governed by the Hellmann-Feynman forces, calculated using density functional theory (DFT). Accordingly, as explained in 3.2, the electronic system is treated within the DFT framework while MD simulations propagate the nuclei in time, considering them as classical particles.

The fundamental equation of motion, Newton's equation of motion, is central to molecular dynamics simulations:

$$m_I \frac{d^2}{dt^2} \mathbf{R}_I = -\nabla_I E_{nn}(\{\mathbf{R}_I\}) - \nabla_I E_m(\{\mathbf{R}_I\}) - M_a \dot{\mathbf{R}}_I \frac{\dot{s}}{s}, \quad (3.25)$$

where $-\nabla_I E_{nn}(\{\mathbf{R}_I\}) = \mathbf{F}_{I,nn}$ is the Coulomb force between the nuclei and $-\nabla_I E_m(\{\mathbf{R}_I\}) = \mathbf{F}_{I,ne}$ are the forces between the electrons and the nuclei calculated using the Hellmann-Feynman theorem [137, 138], which states that the derivative of the total energy with respect to the nuclei coordinates provides the forces acting on the nuclei. The Coulomb forces between the nuclei are directly obtained from their positions. The additional force $M_a \dot{\mathbf{R}}_I \dot{s}/s$ arises from an external heat bath to conduct MD simulations at constant temperature conditions. This thermostat called the Nose-Hoover thermostat [186, 187], effectively adds or extracts energy from the system, thereby maintaining the time-averaged kinetic energy of the nuclei.

3.5. DFT-MD simulations with VASP

The methodology outlined in the preceding sections is implemented within the Vienna Ab-initio Simulation Package (VASP) software suite [158, 189, 190, 191]. A schematic representation of the workflow for these DFT-MD simulations is illustrated in Fig. 3.1.

Initiating with an initial configuration of N atomic nuclei in a simulation box of volume V , VASP employs an iterative process. It starts by estimating the electron energy density and computing the electronic free energy utilising the Kohn-Sham formalism based on the effective one-particle Schrödinger equation proposed by Kohn and Sham. Notably, the Kohn-Sham orbitals are expressed through Bloch functions, which are evaluated in reciprocal space, as elucidated in Section 3.3.2. The Hartree energy J and the Coulomb energy E_{ee} are calculated using Ewald summation [192].

This iterative cycle continues until the electronic free energy reaches its minimum, facilitating the derivation of the Hellmann-Feynman forces. These forces are subsequently incorporated into the set of N_n Newtonian equations of motion [193], which govern the dynamics of the atomic nuclei. The Verlet algorithm [120, 121] is employed to integrate the Newtonian equations of motion, leading to the updating of the positions of the atomic nuclei. Consequently, a new electron density is obtained, initiating the repetition of the DFT-MD cycle for a designated number of MD steps, thereby allowing the system to evolve dynamically over time. The Nose-Hoover thermostat [186, 187] maintains simulations under constant temperature conditions. Periodic boundary conditions are used to minimise surface effects [120]. The electronic pressure is computed using the quantum mechanical virial theorem [143, 150].

Throughout this study, a comprehensive series of convergence tests encompassing factors such as the number of particles, k -points, energy cutoff (E_{cut}), and time step have been meticulously executed to ensure the convergence of the simulations. This rigorous validation process underscores the reliability conducted simulations' reliability and accuracy, reinforcing the result's robustness. For details, see App. A.2.

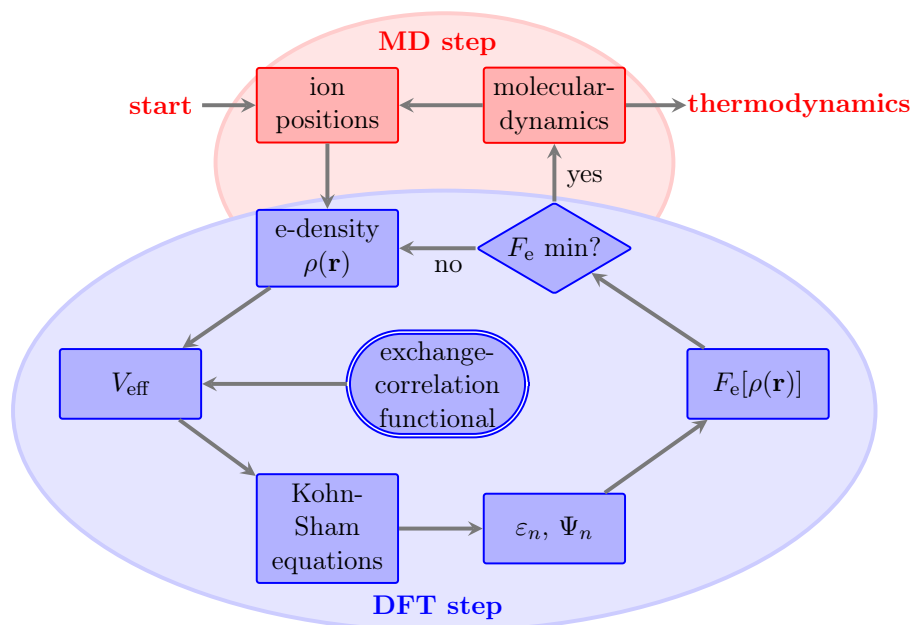


Fig. 3.1.: Schematic workflow of DFT-MD simulations using the Vienna Ab initio Simulation Package (VASP). The figure is adopted from W. Lorenzen [188].

Chapter 4.

Additional theoretical methods

After outlining the main methods, such as MC and DFT-MD simulations, the following chapter outlines additional methods used in this work.

4.1. Nuclear quantum corrections (NQC)

In DFT-MD simulations, the ions are typically treated as classical particles, neglecting the quantum effects of nuclear motion. However, in the molecular regime, nuclear quantum effects (NQE) become crucial and must be considered to obtain accurate results [55, 62]. Path Integral Molecular Dynamics (PIMD) simulations [150, 194, 195] need to be performed to calculate the NQEs directly during the MD simulations. PIMD simulations, however, are 10 – 100 times more computationally expensive than DFT-MD simulations [150] and, therefore, are often impractical for a large number of simulations.

In this work, the NQEs of the ionic motion are reintroduced using a post-processing method designed by Berens *et al.* [196]. The correction to the internal energy U^{QC} , the free energy F^{QC} , and the entropy S^{QC} is calculated by evaluating the difference between the quantum harmonic and the classical oscillator for each frequency interval in the power spectrum of nuclear motion. Since this work only deals with the NQE for the free energy, only F^{QC} is explicitly stated; U^{QC} and S^{QC} can be found in the literature [196]. The correction formula for F^{QC} is given by:

$$F^{QC} = \frac{3Nk_B T}{2\pi} \int_0^\infty d\omega S(\omega, V, T, x) \left[W_F^Q(\omega) - W_F^C(\omega) \right], \quad (4.1)$$

where k_B is the Boltzmann constant, V is the volume, N is the total number of nuclei, ω is the frequency, and $S(\omega, V, T, x)$ is the power spectrum of nuclear motion [49, 50, 55]. The functions $W_F^{Q,C}(\omega)$ are weighting functions for the classical and quantum harmonic oscillator, respectively. They can be derived using the partition function for a quantum mechanical harmonic oscillator and the partition function for a classical harmonic oscillator, and are given by:

$$W_F^Q = \ln(1 - \exp(-\beta\hbar\omega)) + \frac{\beta\hbar\omega}{2}, \quad (4.2)$$

and

$$W_F^C = \ln(\beta\hbar\omega), \quad (4.3)$$

where \hbar is the Planck constant, and $\beta = 1/k_B T$. The power spectrum of nuclear motion is calculated using the velocity-autocorrelation function $\langle \mathbf{v}_a(t) \cdot \mathbf{v}_a(0) \rangle_{V,T}$ evaluated at a given volume V and temperature T [55, 196]:

$$S(\omega, V, T, x) = \sum_a \frac{4N_a m_a}{3Nk_B T} \int_0^\infty dt \cos(\omega t) \langle \mathbf{v}_a(t) \cdot \mathbf{v}_a(0) \rangle. \quad (4.4)$$

The correction term F^{QC} is added to the free energy F^{DFT} calculated from the DFT-MD simulations, yielding $F = F^{DFT} + F^{QC}$.

Note that the volume-dependent spectrum $S(\omega, V, T, x)$ introduces a volume dependence in F^{QC} . To overcome this issue, the pressure needs to be corrected as well using the following relation:

$$p^{QC}(V, T, x) = - \left(\frac{\partial F^{QC}}{\partial V} \right)_{T, x}. \quad (4.5)$$

Therefore, the free energy needs to be fitted to a suitable, differentiable model function. Finally, the corrected pressure is given by $p = p^{QC} + p^{DFT}$.

4.2. Calculating the nonideal entropy

Thermodynamic quantities such as energy, pressure, or structural properties are direct outcomes of DFT-MD simulations. However, when dealing with phase equilibria, knowledge of entropy becomes crucial 1.3. Within the DFT framework, the electronic entropy can be calculated, although the XC influence is often neglected due to the lack of sophisticated finite-temperature XC-functionals. The primary contribution to entropy is the ionic entropy, but unfortunately, it cannot be directly evaluated within the DFT-MD framework. Various methods exist for calculating or approximating the ionic entropy, and in this work, we employ the coupling constant integration (CCI) method developed by J.G. Kirkwood in 1935 [197]. It's important to note that this method is, in principle, exact if the integration with respect to λ is performed using sufficient integration points.

However, other methods for calculating the ionic entropy exist, such as the thermodynamic integration (TI) technique [198] or methods based on the power spectrum of ionic motion [199, 200]. Unfortunately, these methods either require a wide range of EOSs or yield inaccurate and thermodynamically inconsistent results [50]. Another option is to calculate entropy via TI using a reference point [49, 50].

4.2.1. Coupling constant integration (CCI)

$$H(\lambda) = (1 - \lambda)H_0 + \lambda H_1 = \sum_{i=1}^N \frac{\mathbf{p}_i^2}{2m_i} + V_0 + \lambda(V_1 - V_0), \quad (4.6)$$

where H_0 denotes the Hamiltonian of system 0, and H_1 denotes the Hamiltonian of system 1. The change in free energy ΔF between system 0 and system 1 can be calculated using the canonical partition function. It follows

$$\Delta F = F_1 - F_0 = \int_0^1 \langle V_1 - V_0 \rangle_\lambda d\lambda, \quad (4.7)$$

where F_1 and F_0 are the free energies of systems 1 and 0, respectively. Many simulations with different λ values must be conducted to evaluate the integral. A reference system must be chosen so that F_0 is analytically known to calculate the total value of the free energy.

Fortunately, the free energy of an ideal gas is analytically known and given by:

$$F_{\text{id}} = - \sum_{\alpha} N_{\alpha} k_B T \left[\ln \left(\frac{V}{N_{\alpha} \lambda_{\alpha}^3} \right) + 1 \right], \quad (4.8)$$

where $\lambda_{\alpha} = h/\sqrt{2\pi m_{\alpha} k_B T}$ is the thermal wavelength, and N_{α} is the number of particles of species α . Therefore, the CCI is conducted between the noninteracting ideal gas system and the fully interacting DFT-MD system to calculate the nonideal entropy.

4.2.2. Numerical details

As the interaction energy and, consequently, the forces on the ions approach zero under conditions close to the ideal gas, the ions may come very close to each other. Such configurations could disrupt the DFT cycle. Therefore, the CCI was executed in two steps as proposed by Sugino and Car [201]. First, a CCI between the ideal gas and a system interacting with a reflected Yukawa potential [202] was carried out using classical Monte Carlo (MC) simulations. Secondly, the free energy was calculated between the reflected Yukawa potential and the fully interacting DFT-MD system. Hence, the complete free energy can be expressed as follows

$$F(V, T, x) = F_{\text{id}} + \Delta F_{\text{id} \rightarrow \text{RY}} + \Delta F_{\text{RY} \rightarrow \text{DFT-MD}}, \quad (4.9)$$

where $\Delta F_{\text{id} \rightarrow \text{RY}}$ represents the change in free energy between the ideal gas system and the reflected Yukawa potential, and $\Delta F_{\text{RY} \rightarrow \text{DFT-MD}}$ is the change in free energy between the reflected Yukawa potential and the fully interacting DFT-MD system. Unfortunately, calculating an infinite number of λ points is infeasible. While the MC simulation scheme is computationally efficient, DFT-MD computations are highly demanding. Throughout this study, extensive convergence tests with respect to the number of λ points were conducted (see Sec. 6.3).

The reflected Yukawa potential is entirely repulsive, leading to the dissociation of hydrogen and water molecules. These molecules fully dissociate once the DFT-MD forces reach zero at $\lambda = 0$. This potential is described by

$$V_{\text{RY}}^{ij}(r_{ij}) = \begin{cases} a \left(\frac{e^{-br}}{r_{ij}} + \frac{e^{-b(L-r_{ij})}}{L-r_{ij}} - 4 \frac{e^{-bL/2}}{L} \right) & r_{ij} < L/2, \\ 0 & r_{ij} \geq L/2, \end{cases} \quad (4.10)$$

where a , b , and L are coefficients. These parameters must be chosen with caution to ensure a continuous dissociation process. If the reflected Yukawa potential is too repulsive, molecules will dissociate rapidly at $\lambda \gg 0.9$, making it impossible to conduct the integration. Conversely, if the reflected Yukawa potential is not repulsive enough, atoms may approach each other too closely, causing the DFT-MD cycle to fail to converge.

4.3. Electric conductivity from Kubo-Greenwood formalism

To calculate transport properties such as electrical conductivity, linear response theory [203] is used. It states that a small external perturbation of the system in thermodynamic equilibrium causes an effect directly proportional to the perturbation. The Kubo-Greenwood formalism is used to calculate the real part of the dynamic conductivity (dc) [204, 205, 206, 207]. The

real part of the frequency-dependent dynamic conductivity is given by

$$\begin{aligned} \sigma(\omega) = & \frac{2\pi e^2}{3\omega V} \sum_{\mathbf{k}} W(\mathbf{k}) \sum_{j=1} \sum_{i=1} \sum_{\alpha=1}^3 [\mathbf{F}(\epsilon_{i,\mathbf{k}}) - \mathbf{F}(\epsilon_{j,\mathbf{k}})] \\ & \times |\langle \Psi_{j,\mathbf{k}} | \mathbf{v} | \Psi_{i,\mathbf{k}} \rangle|^2 \delta(\epsilon_{j,\mathbf{k}} - \epsilon_{i,\mathbf{k}} - \hbar\omega), \end{aligned} \quad (4.11)$$

where e is the elementary charge, ω is the frequency, and V is the volume of the simulation box, $\epsilon_{i,\mathbf{k}}$ and $\mathbf{F}(\epsilon_{i,\mathbf{k}})$ are the eigenvalue and Fermi occupation number, respectively, of the Bloch state $|\Psi_{i,\mathbf{k}}\rangle$ calculated from DFT. The matrix elements with the velocity operator $\langle \Psi_{j,\mathbf{k}} | \mathbf{v} | \Psi_{i,\mathbf{k}} \rangle$ are calculated with the optical routines internally by VASP [158, 189, 190, 191, 208, 209, 210]. The integration of the Brillouin zone is performed by a weighted summation $\sum_{\mathbf{k}} W(\mathbf{k})$ over a discrete \mathbf{k} -point mesh [207, 211, 212, 213]. The limit $\sigma_e(\omega \rightarrow 0) = \omega_{dc}$ provides the dc. Since all bands have discrete eigenvalues, the δ -function must be artificially broadened to a finite width. The broadening parameter, however, has to be chosen small enough so that the dc limit $\omega \rightarrow 0$ is independent of it. A number of convergence tests are provided in the App. A.2.2.

Chapter 5.

Results

The results section begins by exploring the miscibility gap in binary mixtures of hydrogen and helium, as well as hydrogen and water. It also delves into the non-metal-to-metal transition observed in dense liquid nitrogen. We use the computational tools detailed in the preceding chapters to accomplish this. Note that the results presented in this chapter have already been published in peer review journals [177, 214, 215, 216].

Paper I (2021) [214] presents comprehensive findings on the miscibility gap in hydrogen and helium mixtures, employing the GEMC method. In Paper II (2021) [215], we extend this exploration to the miscibility gap in hydrogen and water mixtures, using the GEMC method. Paper III (2023) [216] introduces a fresh perspective by employing *ab initio* simulations and the CCI method. Additionally, the intricate analysis of the non-metal-to-metal transition in dense liquid nitrogen is detailed in Paper IV (2023) [177]. Collectively, these four papers contribute to a profound understanding of the intriguing behaviours exhibited by these molecular mixtures under extreme conditions.

5.1. Hydrogen and helium

Previous studies [49, 50, 51] based on *ab initio* methods have predicted a considerable miscibility gap in hydrogen and helium mixtures under the pressure and temperature conditions relevant to gas giant planets like Saturn and Jupiter [44]. Recent experiments [69] found demixing at even higher temperatures as proposed by *ab initio* studies [49, 50, 51]. However, performing *ab initio* calculations is computationally expensive, particularly in the lower pressure and temperature regime, making it infeasible to calculate the demixing gap for pressures below 500 kbar. To address these limitations, we employed the GEMC simulation method to determine the region where hydrogen and helium are immiscible. We utilised the exponential-six potential to describe the molecular interactions with the parameters provided in [130]. We conducted GEMC simulations with 32768 particles over 40000 steps, a significant improvement compared to the 512 particles and 2000 – 4000 simulation steps used by Schouten *et al.* [130]. This increase in particle number and simulation steps resulted in significantly better converged results, as shown in the App. A.1. It is important to note that analytical interaction potentials cannot capture effects such as dissociation, ionization, or intramolecular vibrations. Therefore, our results, similar to those of Schouten *et al.* [130], are limited to the molecular regime of hydrogen. We calculated five demixing curves at pressures between 100 and 500 kbar, as depicted in Fig. 5.1.

The helium melting temperatures calculated by Preising and Redmer [94] are shown by coloured diamonds at $x_{\text{He}} = 1$, whereas the hydrogen melting temperatures are depicted by coloured triangles at $x_{\text{He}} = 0$, calculated in Ref. [202]. The black solid line represents the solar helium abundance of $Y = 0.28$ [217]. Notably, the system is predicted to be fully demixed below the melting temperatures of hydrogen and helium. Previous predictions by Schöttler *et al.* [49, 50] suggested an asymmetric demixing curve, while the results of this work indicate symmetric demixing curves. The asymmetric behaviour observed in *ab initio* results

may be attributed to perturbations of intramolecular vibrations, the molecular structure of hydrogen compared to the atomic structure of helium, and differences in interaction strength. Our radial interaction potentials neglect such effects, yet we find reasonable agreement despite these simplifications. In Fig. 5.2, the demixing diagram is depicted for the solar helium concentration of $Y = 0.28$, with our results shown as red circles. We observe excellent agreement with earlier *ab initio* results [49, 51]. Experimental results by Brygoo *et al.* [69], based on reflectivity measurements of laser-driven shock-compressed hydrogen and helium mixtures, are depicted by cyan triangles. While they did not perform experiments below 1 Mbar, they used results obtained by static compression experiments of Loubeyre *et al.* [70] to conduct a fit towards lower pressures. Despite the significant deviations between the results based on *ab initio* methods [49, 50, 51] and experimental results [69] above 1 Mbar, our GEMC results are in excellent agreement below 1 Mbar. Conducting GEMC simulations at pressure and temperature conditions relevant to the interior of Saturn and Jupiter was not possible due to the limitation of the two-body interaction potentials. Nevertheless, our results contribute to a deeper understanding of physical processes leading to the demixing of hydrogen and helium.

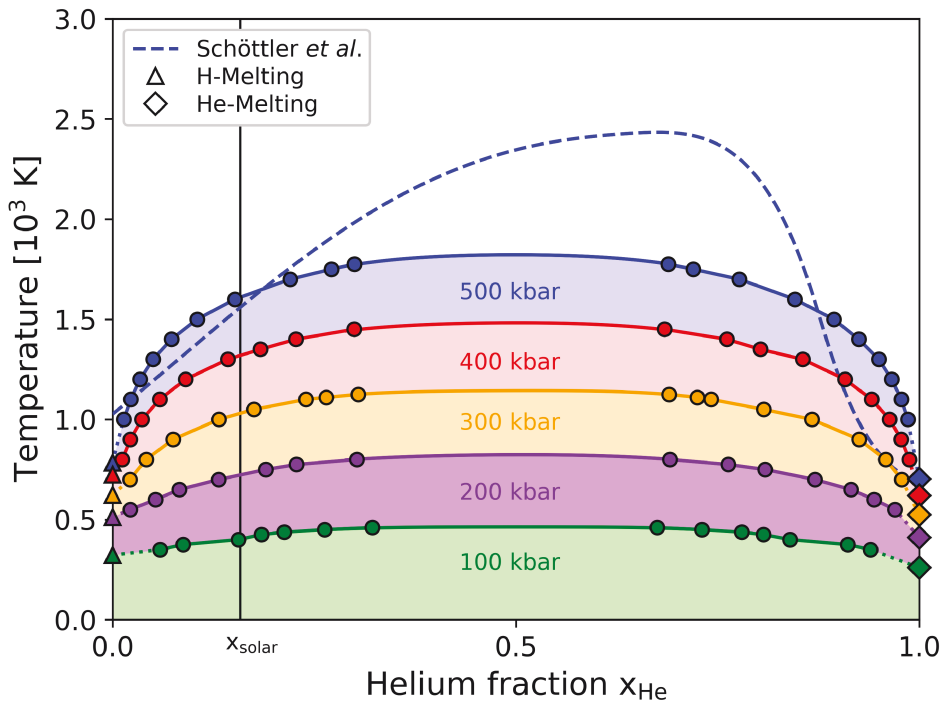


Fig. 5.1.: Miscibility diagram illustrating hydrogen and helium mixtures at five distinct pressures (depicted by colored circles). Shaded areas delineate $p - T$ conditions where demixing occurs, guided visually by smoothing splines. The blue dashed line represents the findings of Schöttler and Redmer [49] from DFT-MD simulations. The solar helium concentration is indicated by the vertical black line. Colored triangles and diamonds represent the melting temperatures of pure hydrogen [202] and helium [218], respectively.

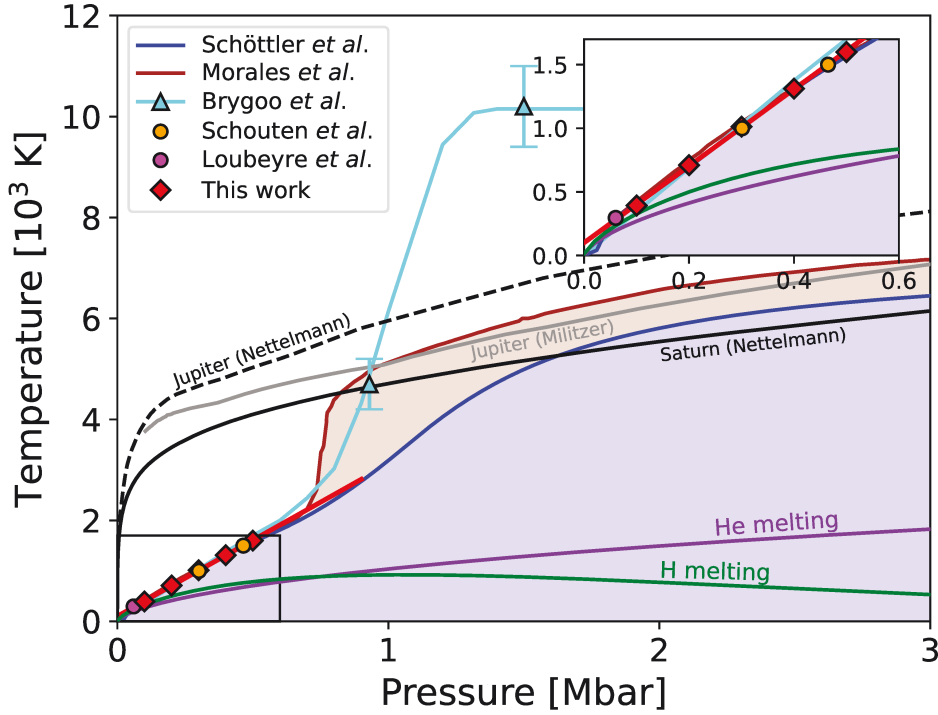


Fig. 5.2.: Miscibility diagram for solar helium abundance of $Y = 0.28$. Our GEMC simulation results are represented by red diamonds, and the red line denotes a linear fit. Earlier results obtained by DFT-MD simulations are depicted by solid lines: Schöttler and Redmer [49, 50] by blue and Morales *et al.* [51] by brown. Demixing is predicted within $p - T$ conditions in the shaded areas. Earlier theoretical results based on GEMC simulations by Schouten *et al.* [130] are depicted by orange circles. Experimental results are shown as colored symbols: Loubeyre *et al.* [70] as purple circles and Brygoo *et al.* [69] as cyan triangles. Present day planetary isentropes for Jupiter are shown as a black dashed line [219] and solid grey line [220] while the isentrope for Saturn is depicted by a solid black line [58].

5.2. Hydrogen and water

A miscibility gap in hydrogen and water mixtures under high pressure and temperature conditions could significantly impact the thermal evolution and structure of ice giant planets such as Neptune and Uranus [1, 10, 59, 221]. Experimental studies [76, 77] based on hydrogen and water trapped in silicates indicate a miscibility gap at pressures between 10 and 40 kbar and temperatures below 1500 K, while earlier theoretical findings predict hydrogen and water to be completely miscible [221]. This work reinvestigates the miscibility diagram and aims to resolve the contradictions. First, we calculated the miscibility gap by conducting GEMC simulations using analytical two-body interaction potentials. Secondly, we used *ab initio* simulations to analyse this miscibility gap further and extend it to higher pressure and temperature conditions.

5.2.1. Miscibility gap calculated with the GEMC method

We conducted GEMC simulations utilising analytical two-body interaction potentials to characterize the interactions between the molecular species hydrogen and water. The exponential-six potential represents the hydrogen-water interactions, while the hydrogen-water interaction

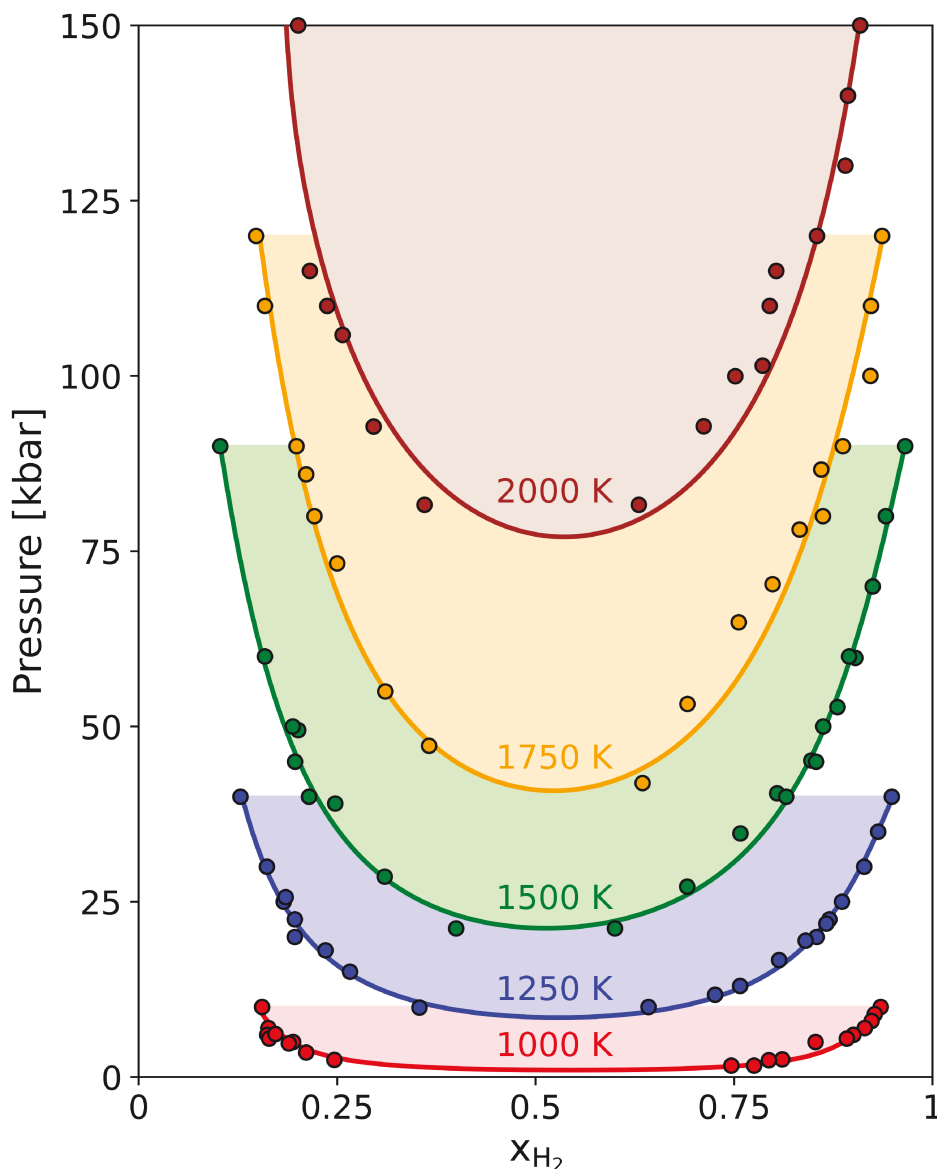


Fig. 5.3.: GEMC simulations for hydrogen and water for five different temperatures (color-coded) [215]. Demixing occurs under $p - T$ conditions within the shaded areas. The smoothing splines serve as visual guides.

is described using the Hulburt-Hirschfelder potential [222]. The interaction between water molecules is modelled using the Stockmayer potential [223], treating water as point dipoles. The corresponding potential parameters are provided in Paper II. Extensive testing confirmed the adequacy of these interaction potentials for describing interactions between hydrogen and water below 2000 K and 150 kbar.

The dipolar interaction between water molecules, scaling with $1/r^3$, introduces finite size effects leading to unconverged simulations even with 30 000 particles. Implementing the reacting field or Ewald summation methods [120] to correct the truncated dipole interaction term is challenging. To address these issues, we performed five GEMC simulations with different particle numbers for each $p - T$ condition and conducted a linear regression to extrapolate to $N \rightarrow \infty$, with a detailed description in Paper II.

We computed five binodal curves at varying temperatures (1000, 1250, 1500, 1750, and 2000 K) and pressures ranging from 5 to 150 kbar, as illustrated in Fig. 5.3. These demixing

curves exhibit near-symmetry but are subtly skewed towards higher hydrogen fractions. This phenomenon underscores the tendency of hydrogen to readily dissolve in water compared to the reverse process. Such behaviour aligns with expectations due to the stronger and anisotropic dipolar intermolecular interactions between water molecules, favouring molecular configurations that minimize electrostatic energy. These intricate structures find it challenging to form in an environment of nonpolar and less strongly interacting hydrogen molecules, resulting in demixing at low water fractions.

In contrast to simulations based on *ab initio* methods, the GEMC simulation procedure neglects certain effects, such as dissociation, ionization, perturbations in intramolecular vibrations, changes in the electronic structure of the molecules, and changes in intramolecular polarization charges. Consequently, it was not feasible to calculate the miscibility gap of hydrogen and water at temperatures above 2000 K or pressures exceeding 150 kbar, where dissociation becomes increasingly important [224, 225]. Combining *ab initio* methods with the GEMC method (*aiGEMC*) represents the best option for overcoming these limitations. Unfortunately, the particle number required to converge *aiGEMC* simulations is too large to facilitate such a combined simulation approach.

5.2.2. Miscibility gap calculated with *ab initio* methods

We conducted DFT-MD simulations to investigate the miscibility gap of hydrogen and water further. We used the CCI technique to calculate the non-ideal entropy and the non-ideal entropy and evaluate differences in the free enthalpy of mixing to evaluate the miscibility gap of hydrogen and water. The CCI was performed as discussed in Sec. 4.2.

We calculated 12 different concentrations of hydrogen and water for 3 different temperatures of 1000, 1500, and 2000 K and five different pressures of 40, 80, 120, 200, and 300 kbar, leading to nine distinct $p - T$ conditions. We conducted extensive convergence tests and used the following ratios of $N_{\text{H}_2}:N_{\text{H}_2\text{O}}$ molecules in our simulation boxes: 128:0, 128:3, 128:10, 128:18, 128:30, 108:36, 48:80, 64:64, 40:64, 21:64, 10:64, 0:64. Detailed convergence tests are given in App. A.2.1. The results of the CCI integration are shown in Fig. 5.4. To conduct the integration between the ideal non-interacting reference and the Yukawa system, 40 λ points were chosen. Additionally, we used 6-11 λ points to calculate the difference in free energy between the system interacting with RY potentials and the fully interaction DFT-MD system. The DFT-MD simulation framework neglects the quantum effects of the nuclear motion. We use a post-processing method developed by Berens *et al.* [196] to reintroduce part of the NQEs, see Sec. 4.1. The potential parameters of the RY potential and further numerical details are provided in Paper III.

The findings for Δg are presented in Fig. 5.5. We used a fifth-order Redlich-Kister ansatz [226] to fit Δg and applied a double tangent construction in cases where the curves exhibited concavity. Notably, the pronounced concave behaviour observed in Δg at temperatures of 1000 K and pressures of 80 kbar and 120 kbar, as well as at 1500 K with pressures of 120 kbar and 200 kbar, strongly indicates demixing.

However, the concave regions are less definitive for the other pressure and temperature conditions. Regrettably, due to the extensive number of simulation steps required for precise results, we could not calculate the miscibility gap for temperatures below 1000 K or pressures below 40 kbar. Furthermore, we refrained from calculating Δg at even higher pressures, as

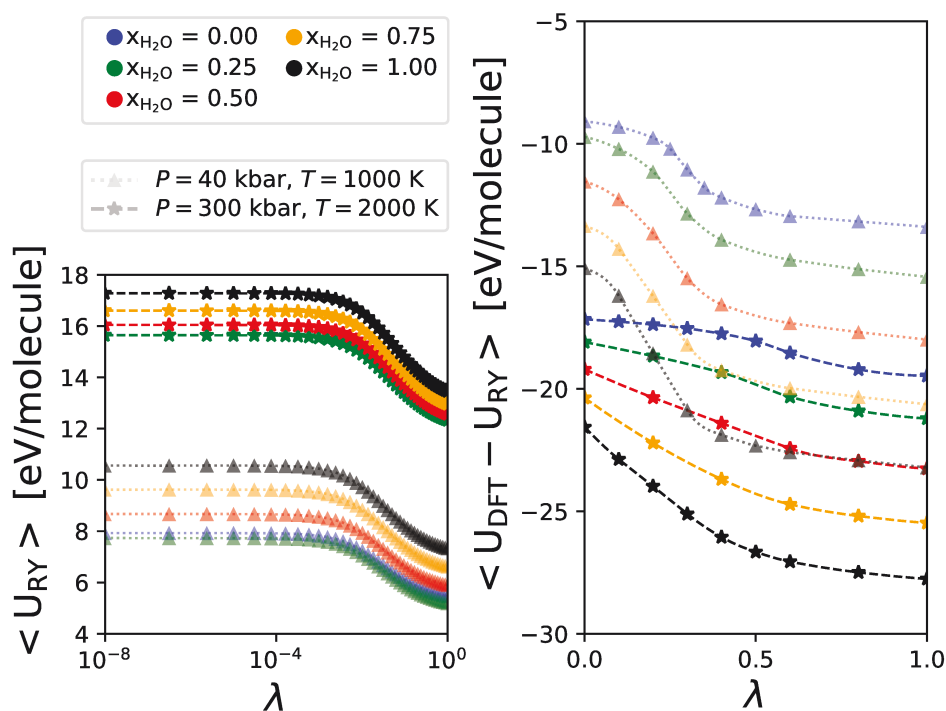


Fig. 5.4.: CCI for five different hydrogen and water concentrations (colour-coded). Results for 40 kbar and 1000 K are shown as triangles, while results for 300 kbar and 2000 K are shown as stars. The dashed lines are Akima splines. The left panel shows the CCI between the ideal non-interacting reference system and the RY potentials, while the right panel shows the results for the CCI between the RY potentials and the fully interacting DFT-MD system.

these conditions intersect with the melting line of water [227, 228, 229, 230, 231, 232, 233, 234, 235].

Upon examining the overall trends, it becomes evident that Δg increases with rising pressure, as lower pressure enhances the ideality of the mixture. Conversely, an increase in temperature results in a decrease in Δg , which can be attributed to the temperature-induced enhancement of water and hydrogen solubility in each other. As demonstrated in previous studies, these trends align with the behaviour commonly observed in partial immiscible binary mixtures, as demonstrated in previous studies [49, 50, 78].

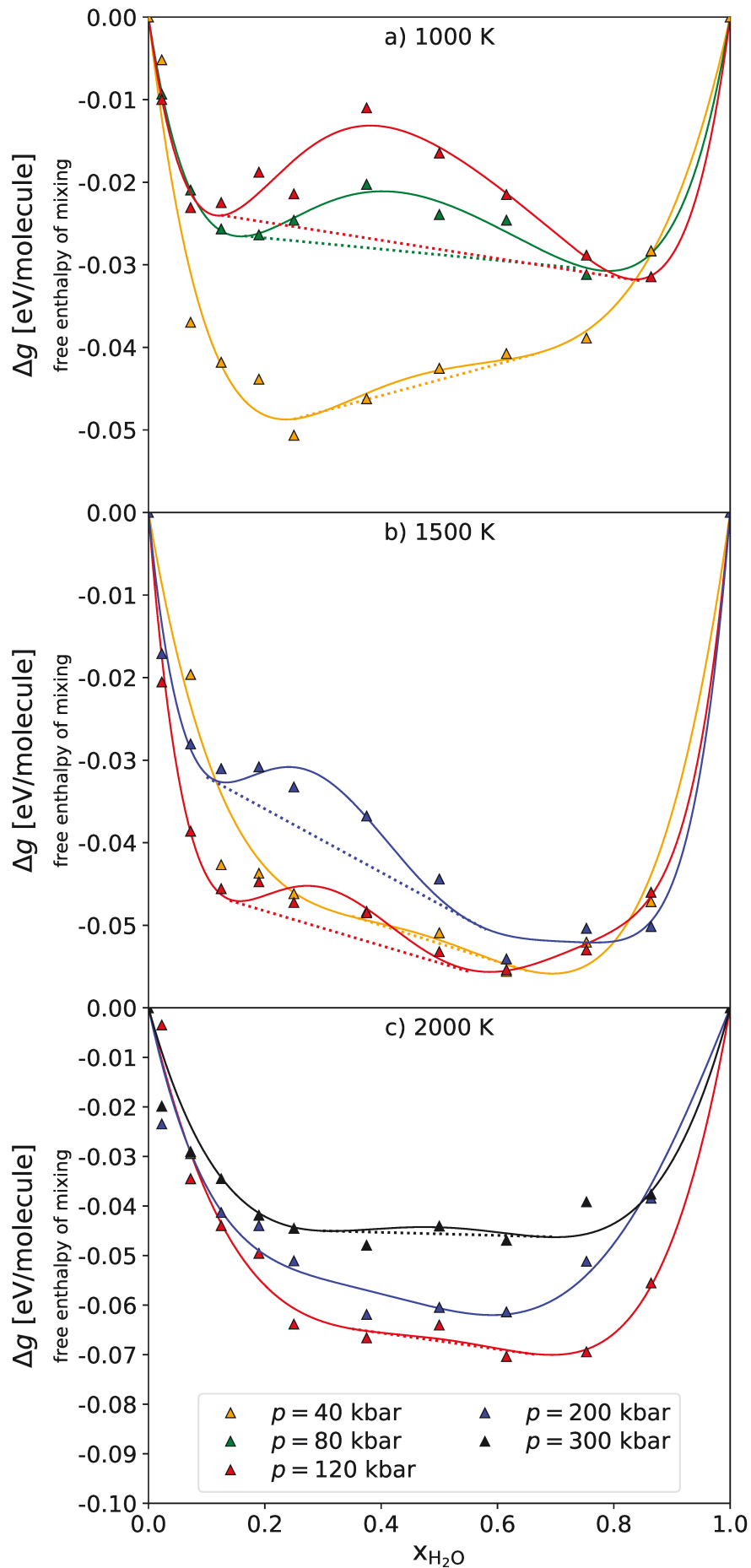


Fig. 5.5.: Gibbs free energy of mixing Δg for different $p - T$ conditions depicted by triangles. We computed five different pressures (colour-coded). The solid lines are Redlich-Kister fits [226] and the dashed lines are the double tangent construction [78].

5.2.3. Comparison of the results

In Fig. 5.6, we present the highest temperature at which demixing occurs. The results obtained through the GEMC method are depicted in red, as derived from Fig. 5.3. To determine the highest temperature of demixing from the DFT-MD simulations, we employed a two-dimensional fitting approach, explained in detail in Paper III, represented as a green solid line. Notably, the results from the DFT-MD simulations exhibit a deviation of 6% from the experimental findings of Bali *et al.* [77] and Vlasov *et al.* [76], and demonstrate a similar steep slope. Furthermore, our GEMC simulation results align closely with those obtained from DFT-MD. However, the DFT-MD results significantly extend the demixing diagram by an order of magnitude in pressure compared to both experimental and GEMC results. Above 100 kbar, our predictions indicate a nearly constant highest temperature for demixing for both methods, suggesting a termination of the demixing region around 2000 K. This termination aligns with fundamental thermodynamic principles, as entropy inherently rises with temperature [78].

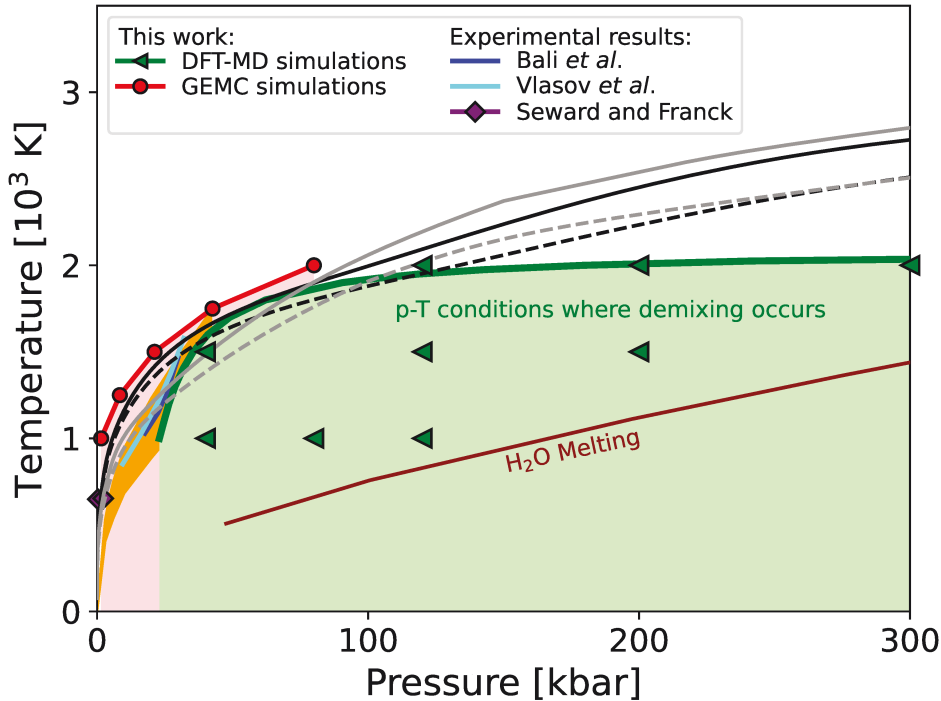


Fig. 5.6.: $p - T$ diagram presenting results for the miscibility gap of hydrogen and water. Green triangles represent all conditions for which we calculated Δg . The solid green line represents the upper temperature limit for demixing from our DFT-MD simulations, while the red line denotes the upper temperature limit from our GEMC simulations. Demixing occurs under conditions within shaded areas. Experimental data from Bali *et al.* [77] (blue line), Vlasov *et al.* [76] (cyan line), and Seward and Franck [236] (purple diamonds) is included. For orientation, the melting line of water is depicted by a solid dark-red line [234]. Predicted $p - T$ profiles along Uranus' and Neptune's radius are shown with solid and dashed lines, respectively, from Scheibe *et al.* [10] (black) and Nettelmann *et al.* [58] (grey). Additionally, Earth's archean geotherms, as provided by Mareschal and Jaupart [237], are represented by the orange shaded area.

5.2.4. Impact on ice giant planets

Examining Fig. 5.6, it is evident that the planetary isentropes of Neptune and Uranus [10, 58] align within the demixing region predicted by both GEMC and DFT-MD simulations. This alignment suggests that the miscibility gap of hydrogen and water may significantly influence the internal structure and evolution of Uranus and Neptune, as discussed below.

The GEMC method predicts the immiscibility of hydrogen and water in the outermost envelope of Uranus and Neptune, reaching radii of approximately $r_U \approx 1.0R_U$ and $r_N \approx 1.0R_N$, where $R_N = 24622$ km represent Neptune’s radius, and $R_U = 25362$ km represents Uranus’ radius. However, as discussed in Sec. 5.2.1, calculating the miscibility gap for pressures above 80 kbar remains impractical due to methodical limitations. Consequently, determining the exact termination radii for the immiscibility of hydrogen and water remains a challenging task. An inspection of Fig. 5.3 suggests that demixing starts at a water fraction of approximately 8% for temperatures between 1000 K and 2000 K.

DFT-MD simulations extend the miscibility diagram by one order of magnitude in pressure. These results predict immiscibility between hydrogen and water within radii ranging from $0.86R_N$ to $0.93R_N$ for Neptune. Nettelmann *et al.* [58] suggest a density jump at $r_{N\rho} = 0.86R_N$ —well within our demixing region. Concerning on Uranus’ planetary model [58], immiscibility of hydrogen and water is expected between radii $0.83R_U$ and $0.87R_U$. The predicted density jump occurs at $r_{U\rho} = 0.77R_U$, near our predicted demixing region. Notably, the DFT-MD results suggest a higher minimum concentration of water to induce demixing, approximately 15%. Additionally, between 40 kbar and 80 kbar, the highest temperature where demixing occurs is slightly lower than in our GEMC results.

In conclusion, the miscibility gap in mixtures of hydrogen and water supports the hypothesis of density discontinuities within ice giant planets. This immiscibility underscores the need for more sophisticated planetary models beyond the adiabatic interior assumption. Such models might include stratified layers with a density jump, which inhibits heat transport by convection and cause trapping of primordial heat within the planet while the relatively thin outer layer cools rapidly [1, 10, 58, 73].

5.3. Nitrogen

Nitrogen, has long intrigued scientists due to its remarkable behaviour under extreme conditions of high pressure and temperature [20, 238]. In this study, we explore the liquid-liquid first-order transition (LL-PT), which is characterized by the abrupt transition from a molecular to a polymeric liquid. Additionally, a nonmetal-to-metal transition occurs [106, 107, 108, 110, 111, 238, 239, 240, 241].

DFT-MD simulations were conducted to calculate the EOS across temperatures ranging from 2000 to 10000 K and densities from 1.1 to 4.2 g/cm³. Extensive convergence tests demonstrated that 256 nitrogen atoms are necessary for simulation convergence, as shown in App. A.2.2. We employed a plane-wave cutoff of 1000 eV and used the BMVP to sample the Brillouin zone, known for better convergence compared to the Γ -point [225, 242]. These simulation parameters resulted in systematic deviations from earlier works, which used fewer particles, the Γ point, and lower plane-wave cutoffs [106, 107, 108, 111, 240, 243]. The p – T conditions

calculated in this work are relevant for the interior of ice giant planets, such as Uranus and Neptune.

Fig. 5.7 displays the calculated EOS. For EOSs below 3500 K, the van der Waals loops indicate the first-order phase transition. The critical temperature is estimated near $T_c = 3500$ K, $\rho_c = 3.4$ g/cm³, and $P_c = 90$ GPa. Comparing our results to Boates and Bonev [107] reveals a systematic shift towards higher pressures. The coexistence line by Driver and Militzer [106] is located at lower pressures, with both earlier works predicting the critical point at significantly higher temperatures. These discrepancies trace back to the significantly higher particle number used in our work. Zhao *et al.* [111] predicted the LL-PT transition at even higher pressures using DFT-MD simulations with the SCAN functional and 64 particles. However, their results lack sufficient convergence and may be inaccurate. Results from Yakub & Yakub [109] are based on an advanced polymerization model using the results of Boates and Bonev [107], while the results of Ross and Rogers [110] rely on the Grüneisen parameter.

Using the Kubo-Greenwood formalism, we calculated the electrical conductivity. Enhanced computational power allowed the use of the hybrid functional HSE, known for more precise results for the band gap than PBE [181, 218, 244, 245]. We selected 100 snapshots of the MD simulation at constant time intervals and used the BMVP to evaluate the Brillouin zone. For temperatures above 4000 K, we evaluated 20 snapshots, utilised MP $3 \times 3 \times 3$ to sample the Brillouin zone, and employed the PBE functional, as metallic-like conductivities prevail at these conditions. Detailed convergence tests are provided in App. A.2.2.

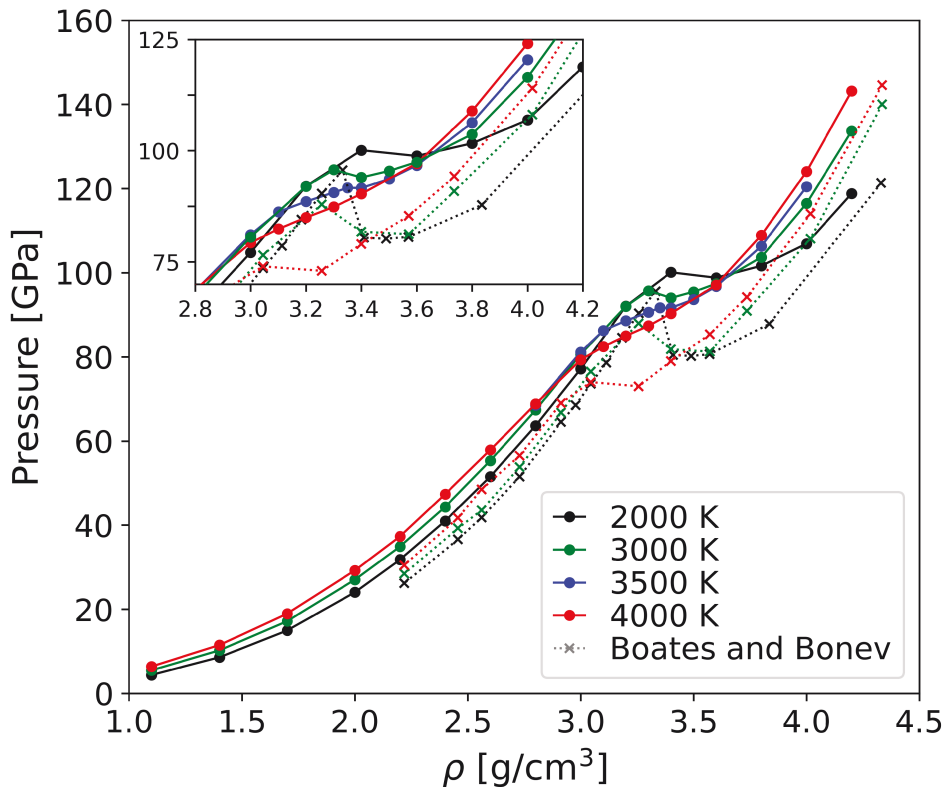


Fig. 5.7.: Thermal EOS for dense fluid nitrogen (pressure as a function of the density) for temperatures between 2000 K and 4000 K (color-coded). The results of this work are shown by solid lines with circles, while those of Boates and Bonev [107] are shown by dotted lines with crosses. The inset depicts the pressure and density region where the van der Waal loop occurs in higher resolution.

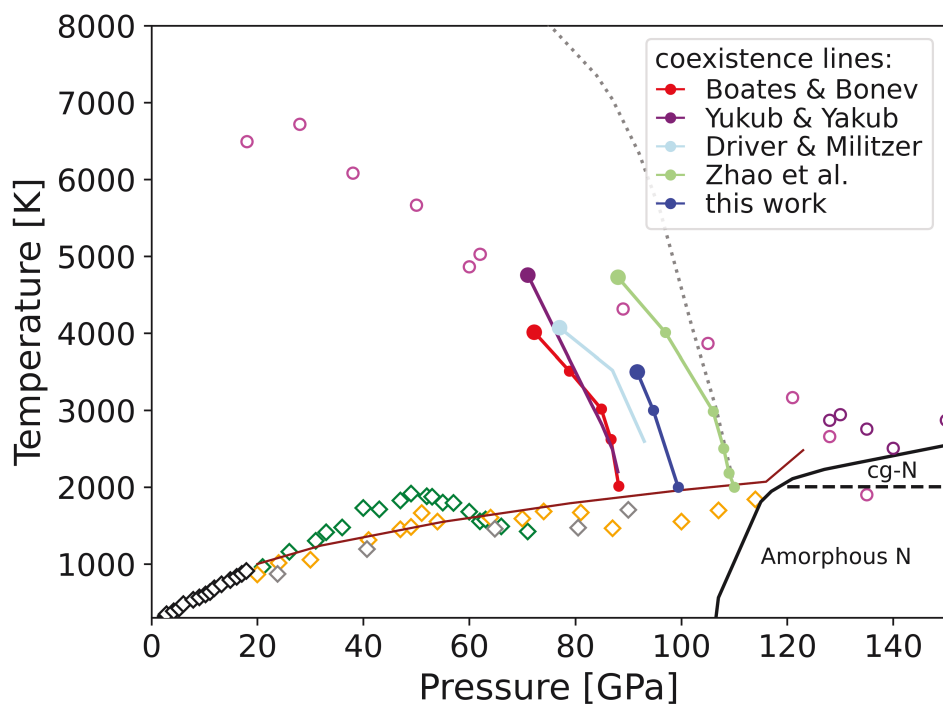


Fig. 5.8.: Phase diagram of dense fluid nitrogen. The LL-PT predictions are color-coded: the results of this work are represented by the blue line, Boates and Bonev [107] by the red line, Yakub and Yakub [109] by the purple line, Driver and Militzer [106] by the light blue line, and Zhao *et al.* [111] by the light green line. The dotted lines depict the chemical model proposed by Ross and Rogers [110]. Magenta and violet circles denote the onset of absorption and reflection, respectively, as observed in laser-heated DAC experiments [239]. Theoretical predictions for the melting line are represented by diamonds: Young *et al.* [113] in black, Mukherjee *et al.* [114] in green, Goncharov *et al.* [115] in orange, and Donadio *et al.* [116] in grey. An experimental prediction for the melting line by Weck *et al.* [93] is indicated with a red line.

Our results for the electric conductivity, alongside those of Boates and Bonev [108], Fu *et al.* [240], Mazevet *et al.* [243], and the experimental results of Chau *et al.* [246], are presented in Fig. 5.9. The HSE functional results in conductivities two orders of magnitude lower compared to the PBE functional. Good agreement is found with Boates and Bonev [108], while deviations from Mazevet *et al.* [243] and Fu *et al.* [240] are attributed to a lower particle number and a different XC functional. The deviations between results of this work and the experimental results of Chau *et al.* [246] might come from inaccurate temperature measurements in the experiment [247].

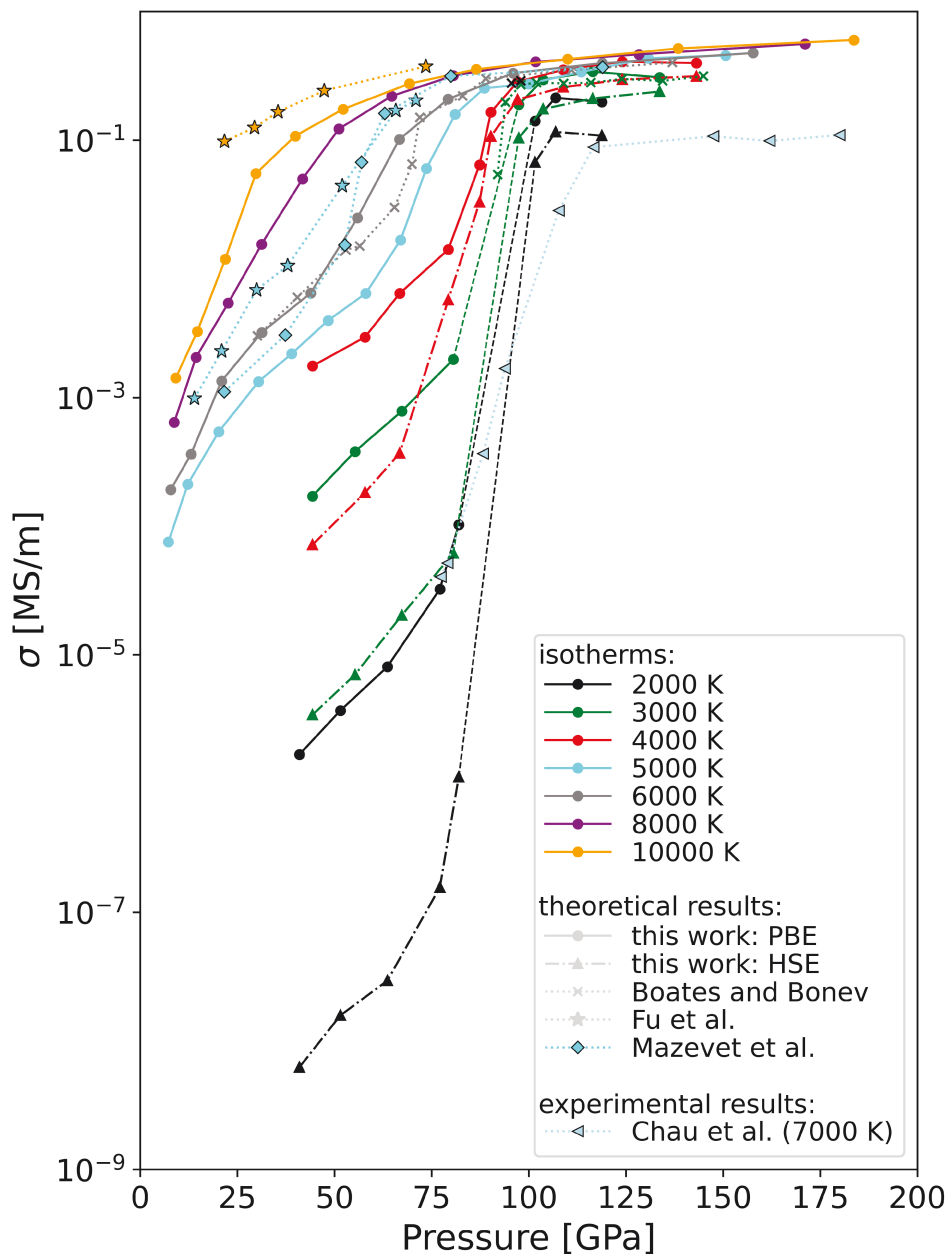


Fig. 5.9.: Static electrical conductivities for nitrogen as a function of pressure at various temperatures (colour-coded). Results obtained using the PBE functional in this work are represented by coloured circles, while Mazevet *et al.*'s [243] results are shown as cyan diamonds, Fu *et al.* [240] as coloured stars, and Boates and Bonev *et al.* [108] as coloured crosses. The results obtained using the HSE functional in this work are represented by coloured triangles pointing upward. Experimental values from Chau *et al.* [246] are indicated with light-blue triangles pointing left.

5.4. Summary and outlook

This work focuses on investigating phase transitions, specifically demixing phenomena, in mixtures of hydrogen and water under extreme pressure and temperature conditions relevant to ice giant planets such as Neptune and Uranus. Additionally, it explores demixing in hydrogen and helium mixtures under extreme pressure and temperature conditions relevant to gas giant planets, along with the first-order liquid-liquid phase transition in dense fluid

nitrogen. Both classical simulation methods (GEMC) and *ab initio* methods (DFT-MD) are employed, and the results are compared with experimental data and planetary models.

Previous studies using *ab initio* methods predicted a miscibility gap in hydrogen and helium mixtures in gas giant planets. In this work, GEMC simulations are used to study the immiscibility of hydrogen and helium between 100 kbar and 500 kbar, extending the *ab initio* calculations of Schöttler and Redmer [49] to lower pressures. Our results reveal symmetric demixing curves, contrasting with the asymmetric predictions from *ab initio* methods. The demixing diagram for solar helium concentration ($Y=0.28$) aligns well with experimental results from Loubeyre *et al.* [70] and Brygoo *et al.* [69]. Furthermore, we find good agreement with earlier *ab initio* results [49, 50, 51]. However, for higher temperatures, where the GEMC method fails, experimental and theoretical results present contradictions. Our results highlight the need for further experimental campaigns to enhance our understanding of hydrogen and helium mixtures.

GEMC simulations are extended to mixtures of hydrogen and water, revealing demixing curves at pressures below 80 kbar and temperatures below 2000 K. Acknowledging limitations in predicting demixing at higher temperatures and pressures due to the constraints of two-body interaction potentials, we conduct extensive *ab initio* calculations with the DFT-MD method to extend the miscibility diagram by one order of magnitude. Using DFT-MD simulations, we calculate the miscibility of hydrogen and water for temperatures between 1000 and 2000 K and pressures between 40 and 300 kbar. Comparing the highest temperature where demixing occurs of GEMC and DFT-MD simulations reveals reasonable agreement. Additionally, the predictions obtained by DFT-MD calculations agree with earlier experimental studies within 6%. The results have implications for understanding the interior structure of ice giant planets such as Neptune and Uranus, supporting the formation of stable stratified layers inside these planets that inhibit heat transport by convection. Our findings will facilitate new experimental campaigns and influence upcoming ice giant missions where the water concentration in the outer atmosphere plays a crucial role.

Moreover, DFT-MD simulations are employed to study the phase transition in dense fluid nitrogen. The results exhibit a first-order transition, consistent with earlier predictions [20, 106, 107, 108, 109, 110, 111]. However, the transition pressure and the critical point deviate from those earlier studies, emphasizing the importance of sufficient particles to converge the simulations. The Kubo-Greenwood formalism is used to calculate electrical conductivity in nitrogen. The conductivity is calculated using the HSE functional, yielding more realistic band gaps than PBE and leading to a difference in conductivity of two orders of magnitude. Our results will spur new experimental campaigns using facilities such as the Linear Coherent Light Source at SLAC Stanford or the European XFEL.

In conclusion, this study enhances our understanding of phase transitions under extreme pressure and temperature conditions, contributing to planetary science and thermodynamics. Given these successes, some questions remain unanswered. The methods used in this work are suitable for studying the behaviour of hydrogen mixed with other heavier species, such as neon or methane, as required to develop an even deeper understanding of planetary objects. More complex hydrogen, carbon, nitrogen, and oxygen mixtures and their mixing properties must be investigated theoretically and experimentally.

Chapter 6.


Publications

The following chapter shows four first-author publications [177, 214, 215, 216]. The titles, the authors, and their contributions are given prior to every publications.

6.1. Gibbs-ensemble Monte Carlo simulation of H₂-He mixtures

Author contributions:

- **A. Bergemann:** Preparation of the manuscript, code development, conducting all the GEMC simulations, interpretation of the results
- **M. French:** Preparation of the manuscript, interpretation of the results
- **M. Schöttler:** Code development
- **R. Redmer:** Supervision of the project, preparation of the manuscript, interpretation of the results

Gibbs-ensemble Monte Carlo simulation of H₂-He mixturesArmin Bergermann, Martin French , Manuel Schöttler, and Ronald Redmer 
Institut für Physik, Universität Rostock, 18051 Rostock, Germany (Received 29 September 2020; accepted 24 November 2020; published 12 January 2021)

We explore the performance of the Gibbs-ensemble Monte Carlo simulation technique by calculating the miscibility gap of H₂-He mixtures with analytical exponential-six potentials. We calculate several demixing curves for pressures up to 500 kbar and for temperatures up to 1800 K and predict a H₂-He miscibility diagram for the solar He abundance for temperatures up to 1500 K and determine the demixing region. Our results are in good agreement with *ab initio* simulations in the nondissociated region of the phase diagram. However, the particle number necessary to converge the Gibbs-ensemble Monte Carlo method is yet too large to offer a feasible combination with *ab initio* electronic structure calculation techniques, which would be necessary at conditions where dissociation or ionization occurs.

DOI: [10.1103/PhysRevE.103.013307](https://doi.org/10.1103/PhysRevE.103.013307)**I. INTRODUCTION**

Hydrogen and helium are not only the first and simplest elements in the Periodic Table, but also the most abundant materials in gas giant planets like Jupiter and Saturn [1,2]. Recent *ab initio* calculations predict that H₂-He mixtures phase separate at 1–2 Mbar, i.e., at conditions in the upper envelope of Jupiter and Saturn [3–6]. This demixing process leads to the formation of He-rich droplets sinking toward the planetary core. The *ab initio* predictions explain not only the reduced He fraction x_{He} in the atmosphere of Jupiter and Saturn compared to the protosolar value of $Y = 0.28$ [1], but also Saturn's excess luminosity [7–9]. The sinking droplets convert gravitational energy into heat, which contributes to the luminosity and delays the cooling of the planet. If this demixing process is neglected, most evolution models of Saturn yield a planetary age substantially lower than that of the solar system [3]. The consideration of demixing processes under extreme pressure and temperature conditions is therefore crucial for the development of improved models of gas giant planets [10,11].

Loubeyre *et al.* [12] measured demixing in the H₂-He system at pressures of $p < 60$ kbar at room temperature by using diamond anvil cells. So far, no experiments indicating demixing at conditions relevant for jovian planets have been published. Schouten *et al.* [13] performed Gibbs-ensemble Monte Carlo simulations to calculate the miscibility gap of H₂-He mixtures. They predicted two demixing curves at $T = 1000$ and 1500 K and found separation at pressures of $p = 230$ and 385 kbar at the lower and higher temperatures, respectively. Additionally, they predicted a demixing line for H₂-He at temperatures of $T \leq 2500$ K and at pressures of $p \lesssim 750$ kbar.

Recently, research has been carried out by using *ab initio* methods to calculate demixing by evaluating differences in the Gibbs free energy ΔG [3–6,14,15]. Lorenzen *et al.* [4] calculated the H₂-He phase diagram for arbitrary He fractions considering the ideal entropy of mixing. This simple

approximation has already led to good results at $p \gtrsim 1$ Mbar but is questionable at pressures of $p \lesssim 1$ Mbar. Morales *et al.* [5,6] conducted similar simulations, but also considered the nonideal entropy to determine the demixing phase diagram for solar He abundance, and obtained a demixing line lower than that of Lorenzen *et al.* [4]. Both of these studies employed *ab initio* simulation methods based on density-functional theory (DFT). The central approximation in DFT is the choice of the exchange-correlation (XC) functional, which determines how accurately the quantum mechanical electronic interactions are captured. While both Lorenzen *et al.* [4] and Morales *et al.* [5,6] used the semilocal Perdew-Burke-Ernzerhof [16] functional, a more recent paper by Schöttler and Redmer [3] used a nonlocal van der Waals XC functional [17] and also considering the nonideal entropy found an even lower demixing line in the pressure-temperature plane than Morales *et al.* [5,6]. These most recent calculations predict H₂-He phase separation to occur in Saturn but not in Jupiter. The intricate correlation between the H₂-He phase diagram, in particular the location of the demixing region, and the evolution of Jupiter and Saturn has been studied in detail recently (see [11]).

Nevertheless, performing *ab initio* calculations is computationally expensive, in particular at the lower pressure and temperature regime. Therefore, we use the Gibbs-ensemble Monte Carlo simulation method of Panagiotopoulos *et al.* [18–20] in this study in order to determine the region where H₂-He mixtures phase separate. Unlike studies based on DFT, our results are limited to mixtures of H₂ molecules and He atoms. First, we calculate two demixing curves at temperatures of $T = 1000$ and 1500 K in order to compare our results with those of Schouten *et al.* [13]. Second, we extend the demixing diagram of Schöttler and Redmer [3] to the lower-temperature and -pressure regime. We calculate demixing curves at pressures of $100 \text{ kbar} \leq p \leq 500 \text{ kbar}$ and at temperatures of $T \lesssim 1800 \text{ K}$. Third, we predict a demixing phase diagram for solar He abundance. In Secs. II and III we briefly explain the simulation technique used in this work.

TABLE I. Parameters for the exponential-six potential (5) regarding the H₂-H₂, H₂-He, and He-He interactions.

Interaction	ϵ (kJ/mol)	r^M (Å)	α	Ref.
H ₂ -H ₂	0.302646	3.43	11.1	[25]
H ₂ -He	0.143840	3.28	12.49	[26]
He-He	0.089763	2.9673	13.1	[27]

In Sec. IV we present our results and compare with previous calculations and experiments. Section V gives a summary.

II. SIMULATION METHOD

In this section we briefly explain the Gibbs-ensemble Monte Carlo (GEMC) method. A more detailed description is given in Refs. [13, 18–20]. This technique is based on two separate simulation boxes which contain $N_{I,II}^A$ particles of species A and $N_{I,II}^B$ particles of species B. The indices I and II denote boxes I and II, respectively. The total number of particles $N^A = N_1^A + N_2^A$ and $N^B = N_1^B + N_2^B$ is conserved. The boxes have different volumes V_I and V_{II} but the same temperature T and the same external pressure p .

The GEMC process evolves the spatial configurations of particles in both simulation boxes in different ways and attempts to simulate a thermal equilibrium state at constant pressure and constant temperature. First, an attempt is made to displace particles within each of both boxes. Second, an attempt is made to resize the volume in order to keep the average pressure constant. Third, particle transfers and particle swaps between the boxes are attempted.

Particle displacement. Every particle is randomly displaced within a maximum allowed distance. The well-known acceptance probability [18] is given by

$$\mathbb{P}_{PD} = \min[1, \exp(-\beta\Delta E)], \quad (1)$$

where $\Delta E = E_{\text{new}} - E_{\text{old}}$ defines the change in energy and $\beta = 1/k_B T$.

Volume change. In order to keep the average pressure constant, we attempt to resize the volumes of both boxes independently within $0 < \Delta V < \Delta V_{\text{max}}$. The acceptance probability was derived in [21, 22] and is given by

$$\mathbb{P}_{VC} = \min\left\{1, \exp\left[-\left(\beta\Delta E - N \ln \frac{V + \Delta V}{V} + \beta p \Delta V\right)\right]\right\}, \quad (2)$$

where ΔV denotes the change in volume.

Particle transfer. A random particle of species A or B contained in either of the boxes I or II is transferred to a random position in the other box. The respective acceptance probability is similar to that for particle insertions in the grand canonical ensemble and given by [18–20]

$$\mathbb{P}_{PT} = \min\left\{1, \exp\left[-\beta\left(\Delta E_I + \Delta E_{II} + \frac{1}{\beta} \ln \frac{V_{II}(N_I^A + 1)}{V_I N_I^A}\right)\right]\right\}, \quad (3)$$

where $\Delta E_I = E_{I,\text{new}} - E_{I,\text{old}}$ and $\Delta E_{II} = E_{II,\text{new}} - E_{II,\text{old}}$. The acceptance probability of transfer steps is quite low at high densities; thus, many transfers will be rejected. The

excluded-volume map sampling method [23] was used to avoid the computational expensive calculation of the change in energy ΔE .

Particle swap. Essentially, the so-called particle swap is a transfer of two particles of different species between the two boxes [13, 24]. First, a random particle of species A or B contained in either of the boxes I or II is chosen. Second, one randomly selects a particle of the other species in the other box. The selected particles may swap their species, whereas their positions remain the same. The acceptance probability of such a swap is given by

$$\mathbb{P}_{PS} = \min\left\{1, \exp\left[-\beta\left(\Delta E_I + \Delta E_{II} + \frac{1}{\beta} \ln \frac{V_{II}(N_I^A + 1)}{V_I N_I^A} + \frac{1}{\beta} \ln \frac{V_I(N_{II}^B + 1)}{V_{II} N_{II}^B}\right)\right]\right\}. \quad (4)$$

III. SIMULATION DETAILS

We used exponential-six potentials

$$\Phi_{ij}(r) = \frac{\epsilon_{ij}}{\alpha_{ij} - 6} \left\{ 6 \exp\left[\alpha_{ij} \left(1 - \frac{r}{r_{ij}^M}\right)\right] - \alpha_{ij} \left(\frac{r_{ij}^M}{r}\right)^6 \right\} \quad (5)$$

to model the interactions in the H₂-He system. The parameters α_{ij} , r_{ij}^M , and ϵ_{ij} are given in Table I. The H₂-H₂ potential is calibrated to shock compression data for pressures up to 750 kbar and temperatures up to 7000 K [25]. The He-He potential is likewise calibrated to shock compression data for pressures up to 120 kbar and temperatures up to 300 K. To extend its applicability to even higher pressures, Young *et al.* [26] performed linear muffin-tin orbital electron-band-theory calculations. Due to the absence of internal degrees of freedom in the He atom, we regard the potential to be valid also at temperatures of several 1000 K. The H₂-He potential is calibrated to diamond anvil cell data for pressures up to 75 kbar and pressures up to 360 K by van den Bergh and Schouten [27].

Initially, we placed 8192 He atoms and 8192 H₂ molecules on simple cubic lattices in each of the boxes. The simulations consisted of 10 000 steps for internal equilibration inside each box, during which we attempted to displace all particles and tried to resize the volumes of both boxes to reach the desired pressure. This internal equilibration process was followed by 40 000 global steps. During a global step, we attempted to displace all particles and resize the volumes. Additionally, 20 000 particle transfers and 2000 particle swaps were tried. After the global equilibrium was reached (usually after 10 000 steps for equilibration), the molar fractions of the species in each box were calculated by averaging until the simulation end. The

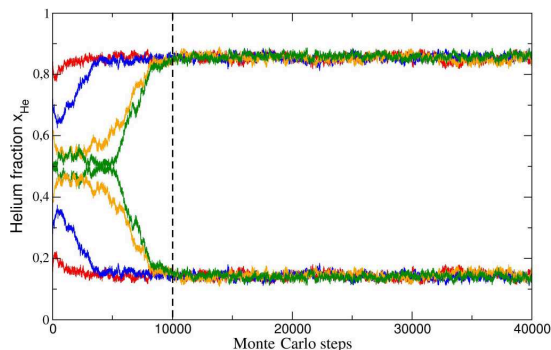


FIG. 1. The GEMC simulation for a H_2 -He mixture at $T = 1400$ K and $p = 400$ kbar. The different colors depict four different initial conditions regarding the concentrations of x_{He} and x_{H_2} . The concentration averaging starts after 10 000 Monte Carlo steps (black dashed line).

large number of 40 000 steps was chosen to diminish errors due to large fluctuations or an insufficiently demixed system. We started the first simulation at high-pressure conditions far away from the lowest pressure at which demixing occurs. After each run, we started a new simulation run at lower pressure conditions until we found H_2 -He to be completely miscible.

In extensive convergence tests, we found that particle numbers $\gtrsim 16384$ are necessary in order to obtain converged results with deviations of less than 1.5%. Because the computational power in 1991 was much more limited than ours today, Schouten *et al.* [13] had to perform their simulations with only 256 He atoms and 256 H_2 molecules and were unable to perform extensive convergence tests with more particles. With such small particle numbers, we observed that the boxes swap “identities” during the simulations several times, i.e., from box I rich in x_{He} and poor in x_{H_2} to box I rich in x_{H_2} and poor in x_{He} , and vice versa for box II. This takes place especially close to the lowest pressure at which demixing occurs.

For each pressure-temperature condition, we ran four simulations with different initial concentrations in box I and box II of x_{He} and x_{H_2} . The situation is depicted in Fig. 1 with four different colors. This method made it easy to detect metastable states or huge fluctuations.

In Fig. 1 a simulation run at a temperature of $T = 1400$ K and a pressure of $p = 400$ kbar is shown. The system is demixed after 10 000 Monte Carlo steps (black dashed line). The average molar fractions are $x_{\text{He}} \approx 0.78$ (box I) and $x_{\text{He}} \approx 0.14$ (box II).

IV. RESULTS AND DISCUSSION

First, we simulated two demixing curves at $T = 1000$ and 1500 K, depicted in Figs. 2 and 3, respectively. The demixing pressures are given as a function of the He fraction x_{He} . Compared to Schouten *et al.* [13], we used a much larger number of particles, which resulted in a much smaller statistical uncertainty. A comparison of the lowest pressure at which demixing

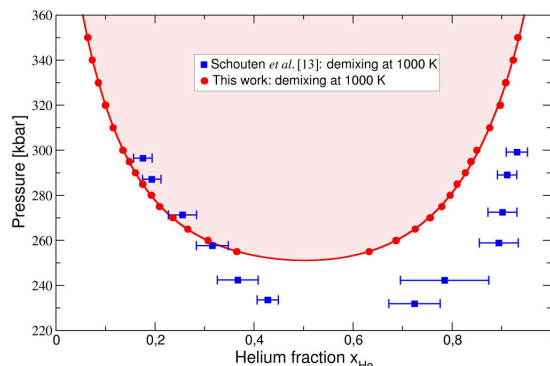


FIG. 2. Demixing curve for H_2 -He at $T = 1000$ K as derived from GEMC simulations. The red circles are the results of this work, while the blue squares are those of Schouten *et al.* [13]. The red line is a smoothing spline acting as a guide to the eye. Demixing occurs under conditions within the red shaded area.

occurs is shown in Table II. Our calculations indicate highly symmetric demixing curves, likely due to the purely radial form of all interaction potentials used. The asymmetry in the curves predicted by Schouten *et al.* is probably an artifact generated by insufficiently converged simulation data. Moreover, our calculations predict a higher lowest pressure at which demixing occurs than Schouten *et al.* [13]. By performing test calculations with 150 000 Monte Carlo steps and the same low particle number ($N = 512$) as Schouten *et al.* [13], we found huge fluctuations regarding the concentrations of x_{He} and x_{H_2} . Within these fluctuations we could reproduce the results of Schouten *et al.* [13].

Second, we simulated five demixing curves at pressures of $100 \text{ kbar} \leq p \leq 500 \text{ kbar}$. The results are depicted in Fig. 4. Because it was not feasible, Schöttler and Redmer [3] did not perform any *ab initio* simulations at pressures below 500 kbar. The colored diamonds at $x_{\text{He}} = 1$ are the He melting

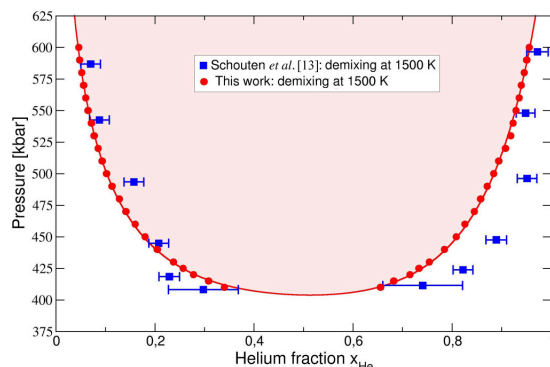


FIG. 3. Demixing curve for H_2 -He at $T = 1500$ K as derived from GEMC simulations. The red circles are the results of this work, while the blue squares are those of Schouten *et al.* [13]. The red line is a smoothing spline acting as a guide to the eye. Demixing occurs under conditions within the red shaded area.

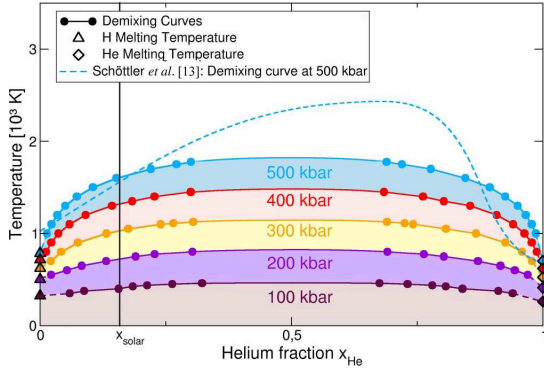


FIG. 4. Miscibility diagram of H_2 -He mixtures as derived from GEMC simulations (colored circles). The lines are smoothing splines acting as guides to the eye. Demixing occurs under conditions within the shaded areas. The dashed line is the result of Schöttler and Redmer [3] using DFT-MD simulations. The vertical black line indicates the solar He concentration as relevant for Fig. 6. Colored triangles and diamonds show the melting temperature of pure H_2 [29] and He [28], respectively.

temperatures as calculated by Preising and Redmer [28]. The colored triangles at $x_{\text{He}} = 0$ are the H_2 melting temperatures [29]. Our demixing curves are highly symmetric, while the result at $p = 500$ kbar of Schöttler and Redmer [3] shows an asymmetric behavior with a kink towards higher He fractions. The *ab initio* data show an abrupt increase of the demixing temperature at low hydrogen fractions at $n_{\text{H}}^{1/3} a_B \approx 0.25$, which represents the concentration required to transform hydrogen to a metal according to the Mott criterion [4]. In *ab initio* simulations, metallization of hydrogen is the driving force of the demixing process at high pressures, which leads to asymmetric demixing curves. At moderate pressures, where hydrogen is yet mostly molecular, the asymmetry in the *ab initio* demixing data can be explained with (i) the molecular structure of hydrogen vs the atomic structure of helium and (ii) the difference in interaction strength between these species, i.e., helium is mostly repulsive while interactions with H_2 are a little more attractive (see Table II). Inserting a low concentration of hydrogen into helium thus has little effect on ΔG , but the presence of low He concentration in H_2 disturbs the interactions between H_2 molecules more strongly, depending on the pressure [30]. Part of the reason is perturbations of the intramolecular vibrations, which are detectable in the contribution of nuclear quantum effects to ΔG , as explained in Chap. 3.2. of Ref. [30]. The purely radial interaction potentials used in this work cannot capture such effects, so the *ab*

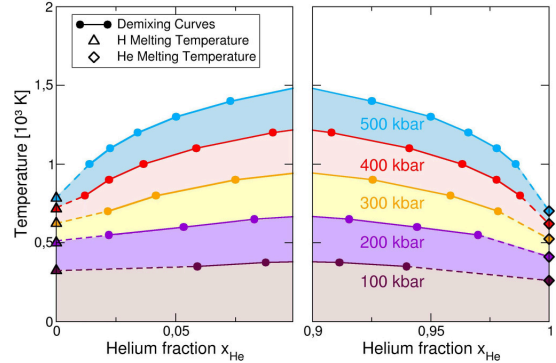


FIG. 5. Miscibility diagram of H_2 -He mixtures for very high and very low He concentrations. The colored circles connected by solid lines are the results of the GEMC simulations. The dashed lines connect the GEMC results with the H_2 and He melting temperatures [28] shown by colored triangles and colored diamonds, respectively.

initio demixing curve at 500 kbar is likely the more reliable one.

Figure 5 compares the H_2 melting temperatures by Morales *et al.* [29] and the He melting temperatures by Preising and Redmer [28] to our demixing curves. The demixing temperature is given as a function of the He fraction. It is not meaningful to use the GEMC method at temperatures below the melting point. Particle insertions and removals of single particles fail for crystalline phases because they involve the creation of interstitial or vacancy defects [31]. Thus, we were not able to simulate a fully demixed system of pure solid He and pure H_2 . The compression behavior at dense H_2 -He mixtures in the solid phase was studied recently by x-ray diffraction [32]. Nevertheless, the dashed lines that connect our results to the H_2 [29] and He [28] melting points can likewise be regarded as reasonable extrapolation of our results to $x_{\text{He}} = 0$ and 1. Hence our GEMC simulations are in alignment with a fully demixed system for temperatures below the melting temperature of H_2 and He, which Schöttler and Redmer [3] also predicted in their *ab initio* simulations.

Because the exponential-six potential shows an unphysical behavior at small intermolecular distances it was not possible to simulate even higher pressures and temperatures. This limitation was already discussed in more detail by Schouten *et al.* [13]. Nevertheless, our work agrees with earlier *ab initio* results [3–6,14,15] reasonably well at conditions where no dissociation or ionization occurs. Finally, we calculated the demixing diagram for the solar He abundance of $Y = 0.28$ at temperatures of $T \lesssim 1500$ K. The results are shown in Fig. 6.

TABLE II. Lowest pressure at which demixing occurs at temperatures of $T = 1000$ and 1500 K. The results of this work are compared with the results of Schouten *et al.* [13].

Temperature T (K)	Schouten <i>et al.</i>	This work
1000	$p = 230$ kbar at $x_{\text{H}_2} = 0.4$	$p = 250$ kbar at $x_{\text{H}_2} = 0.5$
1500	$p = 385$ kbar at $x_{\text{H}_2} = 0.45$	$p = 400$ kbar at $x_{\text{H}_2} = 0.5$

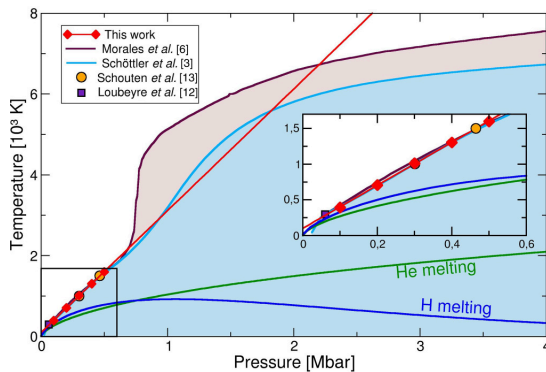


FIG. 6. Miscibility diagram at the solar He abundance of $Y = 0.28$. Red diamonds depict results of this work obtained with the GEMC method and the red line is a linear fit towards higher temperatures. Colored areas show results of *ab initio* simulations performed by Schöttler and Redmer (lower blue area) [3] and Morales *et al.* (upper violet area) [6]. The magenta square depicts the experimental result of Loubeyre *et al.* [12] and the orange circle the result of Schouten *et al.* [13]. At low temperatures the melting lines for H_2 [29] and He [28] are shown for the sake of orientation. The inset shows the results at the p - T domain considered here.

The red diamonds are the results of this work, which are in very good agreement with the experimental data of Loubeyre *et al.* [12] and *ab initio* results of Refs. [3,6]. Interestingly, the deviation between the results of Schouten *et al.* [13] and

ours is relatively small in the pressure-temperature diagram, despite the poor convergence of their simulations.

V. CONCLUSION

In summary, we have used GEMC simulations to examine the H_2 -He phase diagram at pressures of $100 \text{ kbar} \leq p \leq 500 \text{ kbar}$ and temperatures of $T \lesssim 1800 \text{ K}$. In doing so, we extended the hydrogen-helium miscibility diagram of Schöttler *et al.* [3] to lower pressures. Our GEMC simulations indicate a fully demixed system below the He melting temperature and reproduce earlier results obtained from *ab initio* methods [3–6] with a significantly different approach. Although the pressures and temperatures considered in this work do not overlap with Jupiter’s or Saturn’s interior conditions, our findings facilitate efforts to understand physical processes that lead to demixing of hydrogen and helium in astrophysical objects. Our results are in agreement with experiments of Loubeyre *et al.* [12] and should stimulate further demixing experiments toward higher pressures and temperatures. Technically, we found the GEMC method not yet suitable to be combined with *ab initio* electronic structure calculations in order to determine miscibility diagrams because of the very high particle number needed to achieve convergence.

ACKNOWLEDGMENTS

We thank Mandy Bethkenhagen and Hanns-Peter Liermann for helpful discussions. This work was supported by the Deutsche Forschungsgemeinschaft via the Research Unit FOR 2440 and by Deutsches Elektron-Synchrotron (DESY) Hamburg via the Centre for Molecular Water Science.

- [1] U. von Zahn, D. M. Hunten, and G. Lehmacher, *J. Geophys. Res.* **103**, 22815 (1998).
- [2] B. J. Conrath, D. Gautier, R. A. Hanel, and J. S. Hornstein, *Astrophys. J.* **282**, 807 (1984).
- [3] M. Schöttler and R. Redmer, *Phys. Rev. Lett.* **120**, 115703 (2018).
- [4] W. Lorenzen, B. Holst, and R. Redmer, *Phys. Rev. Lett.* **102**, 115701 (2009).
- [5] M. Morales, E. Schwegler, D. Ceperley, C. Pierleoni, S. Hamel, and K. Caspersen, *Proc. Natl. Acad. Sci. USA* **106**, 1324 (2009).
- [6] M. A. Morales, S. Hamel, K. Caspersen, and E. Schwegler, *Phys. Rev. B* **87**, 174105 (2013).
- [7] D. J. Stevenson and E. E. Salpeter, *Astrophys. J. Suppl.* **35**, 221 (1977).
- [8] J. J. Fortney, *Science* **305**, 1414 (2004).
- [9] R. Püstow, N. Nettelmann, W. Lorenzen, and R. Redmer, *Icarus* **267**, 323 (2016).
- [10] D. J. Stevenson, *Phys. Rev. B* **12**, 3999 (1975).
- [11] C. R. Mankovich and J. J. Fortney, *Astrophys. J.* **889**, 51 (2020).
- [12] P. Loubeyre, R. Letouillec, and J. Pinceaux, *J. Phys.: Condens. Matter* **3**, 3183 (1991).
- [13] J. A. Schouten, A. de Kuijper, and J. P. J. Michels, *Phys. Rev. B* **44**, 6630 (1991).
- [14] O. Pfaffenzeller, D. Hohl, and P. Ballone, *Phys. Rev. Lett.* **74**, 2599 (1995).
- [15] W. Lorenzen, B. Holst, and R. Redmer, *Phys. Rev. B* **84**, 235109 (2011).
- [16] J. P. Perdew, K. Burke, and M. Ernzerhof, *Phys. Rev. Lett.* **77**, 3865 (1996).
- [17] M. Dion, H. Rydberg, E. Schröder, D. C. Langreth, and B. I. Lundqvist, *Phys. Rev. Lett.* **92**, 246401 (2004).
- [18] A. Z. Panagiotopoulos, *Mol. Phys.* **61**, 813 (1987).
- [19] A. Panagiotopoulos, N. Quirke, M. Stapleton, and D. Tildesley, *Mol. Phys.* **63**, 527 (1988).
- [20] A. Z. Panagiotopoulos, *Mol. Simul.* **9**, 1 (1992).
- [21] D. Frenkel and B. Smit, *Understanding Molecular Simulation: From Algorithms to Applications*, 2nd ed. (Academic, San Diego, 2002).
- [22] M. Allen and D. Tildesley, *Computer Simulation of Liquids* (Oxford University Press, Oxford, 1987).
- [23] G. L. Deitrick, L. E. Scriven, and H. T. Davis, *J. Chem. Phys.* **90**, 2370 (1989).
- [24] J. de Pablo and J. Prausnitz, *Fluid Phase Equilib.* **53**, 177 (1989).
- [25] M. Ross, F. H. Ree, and D. A. Young, *J. Chem. Phys.* **79**, 1487 (1983).

ARMIN BERGERMANN *et al.*PHYSICAL REVIEW E **103**, 013307 (2021)

- [26] D. A. Young, A. K. McMahan, and M. Ross, *Phys. Rev. B* **24**, 5119 (1981).
- [27] L. C. van den Bergh and J. A. Schouten, *J. Chem. Phys.* **89**, 2336 (1988).
- [28] M. Preising and R. Redmer, *Phys. Rev. B* **100**, 184107 (2019).
- [29] M. A. Morales, C. Pierleoni, E. Schwegler, and D. M. Ceperley, *Proc. Natl. Acad. Sci. USA* **107**, 12799 (2010).
- [30] M. Schöttler and R. Redmer, *J. Plasma Phys.* **85**, 945850201 (2019).
- [31] B. Chen, J. I. Siepmann, and M. L. Klein, *J. Phys. Chem. B* **105**, 9840 (2001).
- [32] J. Lim, M. Kim, S. Duwal, S. Kawaguchi, Y. Ohishi, H.-P. Liermann, R. Hrubyak, J. S. Tse, and C.-S. Yoo, *Phys. Rev. B* **101**, 224103 (2020).

6.2. Gibbs-ensemble Monte-Carlo simulation of H₂-H₂O mixtures

Author contributions:

- **A. Bergemann:** Preparation of the manuscript, code development, conducting GEMC simulations, interpretation of the results
- **M. French:** Preparation of the manuscript, interpretation of the results
- **R. Redmer:** Supervision of the project, preparation of the manuscript, interpretation of the results


 Cite this: *Phys. Chem. Chem. Phys.*,
2021, **23**, 12637

 Received 3rd February 2021,
Accepted 19th May 2021

DOI: 10.1039/d1cp00515d

rsc.li/pccp

Gibbs-ensemble Monte Carlo simulation of H₂–H₂O mixtures

 Armin Bergermann, , Martin French  and Ronald Redmer 

The miscibility gap in hydrogen–water mixtures is investigated by conducting Gibbs-ensemble Monte Carlo simulations with analytical two-body interaction potentials between the molecular species. We calculate several demixing curves at pressures below 150 kbar and temperatures of $1000\text{ K} \leq T \leq 2000\text{ K}$. Despite the approximations introduced by the two-body interaction potentials, our results predict a large miscibility gap in hydrogen–water mixtures at similar conditions as found in experiments. Our findings are in contrast to those from *ab initio* simulations and provide a renewed indication that hydrogen–water immiscibility regions may have a significant impact on the structure and evolution of ice giant planets like Uranus and Neptune.

1 Introduction

Planetary models for the ice giant planets suggest that compounds of H, C, N, and O are the major contributors to the total mass of these planets. Thus, it is a key challenge to develop a deep understanding of the physical and chemical behaviour of such planetary mixtures under high-pressure and -temperature conditions.^{1–3} Since ice giant planets like Neptune and Uranus also contain a significant amount of hydrogen, mixtures of heavy elements with hydrogen might play an important role in our understanding of their structure and evolution.^{4–7}

Many current interior models for Uranus and Neptune assume three different layers – a rocky core, an inner layer rich in H₂O, and an outer layer rich in H₂, which leads to density discontinuities at the layer boundaries.^{4,8–12} A sample planetary profile of such a planet is depicted in Fig. 1. Alternative models without jumps in the density-radius relation exist as well.^{13,14} The interior of the ice giant planets is mostly assumed to be adiabatic.^{4,5,15–17} Most adiabatic models are unable to explain the thermal evolution and brightness of Uranus and Neptune,^{4,5,8} though, albeit a few are.^{16,18} The consideration of primordial heat trapped inside the planet in more refined models might offer a solution to these issues. Accordingly, the deep interior should be significantly hotter than assumed in the adiabatic case and still cooling.^{11,12,16,19} Nettelmann *et al.*⁷ investigated the influence of thermal boundary layers that partially inhibit convection and might offer an explanation for the low luminosity of Uranus. In 2019, Vazan and Helled²⁰ also predicted non-adiabatic interior profiles to match the present luminosity.

The partial immiscibility of H₂–H₂O could cause layer formation in ice giants and inhibit heat transport by convection. In 1981, Seward and Franck²¹ examined the miscibility gap of H₂–H₂O mixtures using an autoclave with sapphire windows. The autoclave was heated to 723 K and then cooled down slowly. By measuring temperature and pressure along isochores, the transition between a miscible and an immiscible H₂–H₂O mixture was identified through kinks observed in the temperature–pressure curves. Demixing was observed at temperatures below $T < 713\text{ K}$ and pressures of $p < 2.5\text{ kbar}$. In 2013, Bali *et al.*²² carried out high-pressure experiments using a piston-cylinder apparatus with samples of H₂ and H₂O trapped as synthetic fluid inclusions in quartz or olivine. They found demixing at temperatures of $1000\text{ K} < T < 1300\text{ K}$ and pressures between $17\text{ kbar} < p < 26\text{ kbar}$ by examining the samples with optical microscopy and Raman spectroscopy. Their results suggest that H₂–H₂O mixtures may phase separate

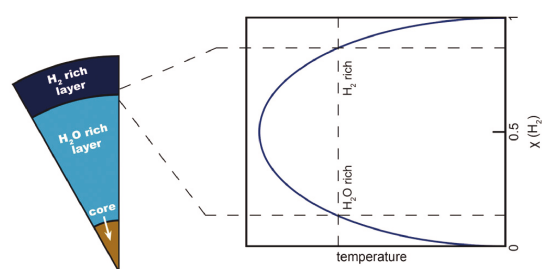


Fig. 1 Left: A typical three-layer model with an outer shell rich in H₂, an inner shell rich in H₂O, and a rocky core. Right: H₂–H₂O molar fraction at the boundary between the layers. Immiscibility of H₂ and H₂O may be a reason for layer formation in ice giant planets.

Institut für Physik, Universität Rostock, D-18051 Rostock, Germany.
E-mail: armin.bergermann@uni-rostock.de

during the evolution process of ice giant planets. Recently, Soubiran and Militzer^{6,23} conducted *ab initio* simulations to calculate demixing by evaluating differences in the Gibbs free energy. They found H₂-H₂O to be completely miscible at pressures of 20 kbar < p < 700 kbar and temperatures of 1000 K < T < 6000 K. Accordingly, demixing should not occur during any stage of the evolution of ice giant planets, contrary to the experimental finding of Bali *et al.*²² The *ab initio* simulations are based on density functional theory (DFT) and thermodynamic integration techniques to determine the entropy. The central approximation in DFT is the choice of the exchange–correlation (XC) functional, which determines how accurately the quantum mechanical electronic interactions are captured and might influence the results, albeit Soubiran and Militzer^{6,23} found consistent results using the semi-local PBE²⁴ functional and a van der Waals functional.²⁵

Performing *ab initio* calculations is computationally expensive and describing the influence of the long-range dipolar interactions between water molecules might require many more particles than can be handled efficiently in such miscibility calculations. In the present work, we employ the Gibbs-Ensemble Monte-Carlo (GEMC) method of Panagiotopoulos *et al.*^{26–28} and use two-body interaction potentials to determine whether or not H₂-H₂O mixtures separate in the interior of ice giant planets. We find that demixing occurs for temperatures of 1000 K ≤ T ≤ 2000 K and pressures of 1.5 kbar < p < 85 kbar.

The outline of our paper is as follows. In Section 2, we describe the molecular interaction potentials used in this work. In Section 3, we explain the GEMC method and give a detailed overview of the particle numbers necessary to obtain converged results which are presented in Section 4. Conclusions are given in Section 5.

2 Molecular interaction models

We used three different analytical two-body interaction potentials to calculate the interactions in the molecular H₂-H₂O mixture. All molecules are treated as point particles, *i.e.*, they act as centers for radial and, in case of H₂O-H₂O interaction, also dipolar interactions.

An exponential-six potential,

$$\Phi_{e6}(r) = \frac{\varepsilon}{\alpha - 6} \left\{ 6 \exp \left[\alpha \left(1 - \frac{r}{r_M} \right) \right] - \alpha \left(\frac{r_M}{r} \right)^6 \right\}, \quad (1)$$

was used to describe the H₂-H₂ interactions. The H₂-H₂ potential was calibrated to shock compression data for pressures up to 750 kbar and temperatures up to 7000 K.²⁹ We used this spherically symmetric potential in a preceding study on hydrogen–helium demixing and found it to perform well in

predicting the respective demixing conditions below a pressure of 500 kbar.³⁰ Further comparison to *ab initio* simulation results³¹ indicated that, although effects from non-sphericity become noticeable at few 100 kbar, they do not introduce substantial errors to the calculated hydrogen–helium demixing line.³⁰ The parameter values α , r_M , and ε are given in Table 1.

The Stockmayer potential³² was introduced in 1941 to describe interactions between polar fluids. In this work, it is used to describe the H₂O-H₂O interactions. The Stockmayer potential consists of two parts. The first part represents a Lennard-Jones potential, while the second part describes the interaction between two point dipoles. This dipole–dipole interaction term scales with $1/r^3$, which we here refer to as a long range interaction. The potential reads:

$$\Phi_{St}(r) = 4\varepsilon \left[\left(\frac{\sigma}{r} \right)^{12} - \left(\frac{\sigma}{r} \right)^6 - \delta \left(\frac{\sigma}{r} \right)^3 \right], \quad (2)$$

where $\delta = \zeta \mu^2 / 4\sigma^2 \varepsilon$, and $\zeta(\Theta_1, \Theta_2, \phi)$ is a function describing the angular dependence of the dipole–dipole interaction. The dipole strength is defined by μ , while Θ_1 and Θ_2 are the angles between the two dipoles and the line connecting the centres of the molecules. Additionally, ϕ defines the azimuthal angle between the molecules.

Note that the Stockmayer potential cannot properly describe hydrogen bonding or the typical 4.5-fold coordinated geometrical configurations of water molecules in liquid water. However, experiments and *ab initio* simulations show that such structures or bonding mechanisms do not play a significant role at high temperature–pressure conditions relevant for our calculations.^{33,34}

Prior to our demixing calculations, we performed ordinary Monte-Carlo (MC) simulations for pure water using the Stockmayer potential with parameter values for σ , ε and μ from ref. 35 and 36 and found large deviations from the equation of state (EOS) data given by Wagner and Pr \ddot{u} \mathring{f},³⁷ which is a high-quality reference standard for water up to several kbar. Therefore, we recalibrated ε and σ to ensure that our simulations reproduce the thermal EOS of Wagner and Pr \ddot{u} \mathring{f}³⁷ within 5% in the range of temperatures between 1000 K < T < 2000 K and pressures below p < 150 kbar. The recalibrated parameter values are given in Table 1. Additionally, Fig. 2 illustrates that MC simulations with the recalibrated Stockmayer potential reproduce the thermal EOS of Wagner and Pr \ddot{u} \mathring{f}³⁷ well for pressures below p < 150 kbar.

To describe the H₂-H₂O interactions, we used the Hulburt-Hirschfelder potential,³⁸

$$\Phi_{HH}(r) = \varepsilon [\exp(-2\alpha x) - 2 \exp(-\alpha x) + \beta x^3 (1 + \gamma x) \exp(-2\alpha x)], \quad (3)$$

Table 1 Parameters for the analytical two-body potentials used to describe the interaction between the molecular species H₂ and H₂O

	ε (kJ mol ⁻¹)	r_M (Å)	r_e (Å)	σ (Å)	μ (Debye)	α	β	γ	Ref.
H ₂ -H ₂	0.302646	3.43	—	—	—	11.1	—	—	29
H ₂ O-H ₂ O	2.6	—	—	2.825	1.85	—	—	—	This work
H ₂ -H ₂ O	1.15782	—	3.269	—	—	6.1750	10.18	1.144	35

PCCP

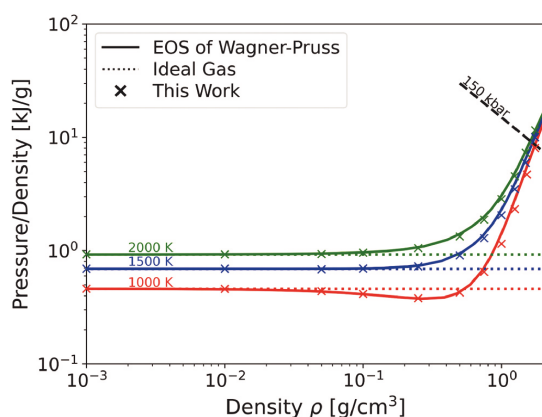


Fig. 2 Thermal EOS for H₂O at temperatures of $T = 1000, 1500,$ and 2000 K. Solid lines present the EOS data by Wagner and Pr \ddot{u} ß,³⁷ dotted lines represent the molecular ideal gas. The black dashed line represents a pressure of 150 kbar. The crosses depict the results of our Monte Carlo simulations obtained with $\sigma = 2.825$ Å, $\epsilon = 2.6$ kJ mol⁻¹, and $\mu = 1.85$ Debye, see Table 1.

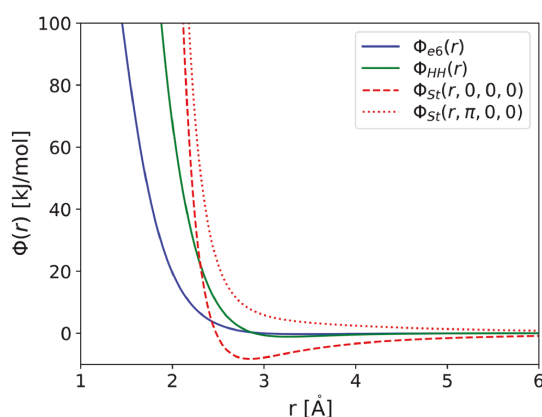


Fig. 3 Comparison of the exponential six potential, the Hulbert–Hirschfelder potential, and the Stockmayer potential. The red dashed and dotted lines represent the strongest and weakest interaction of H₂O, respectively, depending on the orientation of the molecules.

where $x = (r - r_c)/r_c$. In ref. 39, a rigid-body potential energy surface for the H₂–H₂O complex was constructed using scaled perturbation theory, which was then employed to calculate the second cross virial coefficient. Aubreton *et al.*³⁵ used this data to calibrate the H₂–H₂O potential and recommend its use between $200 \text{ K} < T < 2000 \text{ K}$. The parameter values are shown in Table 1 and the potentials are displayed in Fig. 3.

3 Simulation method

In this section, we briefly outline the GEMC method. A detailed description is given in ref. 26–28 and 40. In a preceding paper,

we employed the GEMC method to calculate demixing in hydrogen–helium mixtures at high pressures up to 500 kbar and temperatures up to 1800 K.³⁰

The Gibbs-ensemble method employs two different simulation boxes subject to the same external pressure p and the same temperature T , but with different volumes V_I and V_{II} . They contain $N_{I,II}^{\text{H}_2}$ hydrogen and $N_{I,II}^{\text{H}_2\text{O}}$ water molecules. Boxes I and II are denoted by the indices I and II, respectively. The total number of molecules $N^{\text{H}_2} = N_I^{\text{H}_2} + N_{II}^{\text{H}_2}$ and $N^{\text{H}_2\text{O}} = N_I^{\text{H}_2\text{O}} + N_{II}^{\text{H}_2\text{O}}$ is conserved.

The GEMC method can simulate a mixed or demixed multi-component system at constant pressure and temperature. We followed the same simulation procedure as performed in ref. 30 and 40. First, it is attempted to displace all hydrogen molecules. Likewise, all water molecules are attempted to be either displaced or rotated with an equal probability of 50%. The order of displacement and rotation steps is chosen randomly. To keep the average pressure constant, it is attempted to resize the volume in both boxes sequentially. Third, particle transfers between the boxes are attempted to simulate the equilibration of the chemical potentials, *i.e.*, random H₂O or H₂ molecules were transferred from box I to box II or *vice versa*. The new positions and orientations of the transferred molecules were chosen randomly. Considering the low acceptance probability of transfer steps at high pressure conditions, particle swap steps are introduced to speed up the simulation. These steps are essentially exchanges of one H₂ with one H₂O molecule, whereas the positions of the swapped molecules do not change. For transfers and swaps the species, the boxes, and the individual molecules were chosen randomly with equal probabilities. The GEMC method thus circumvents the calculation of chemical potentials. Acceptance probabilities for the individual MC steps are given in ref. 30.

A fundamental requirement for a Monte-Carlo simulation is microreversibility; otherwise, deviations from the Boltzmann distribution may arise. A random choice of individual steps (displacement, rotation, volume change, particle transfer) ensures microreversibility. As written above, we grouped several individual steps of the same type together into blocks (displacement/rotation, volume change, particle transfer, and particle swaps), which allowed for more efficient parallelisation of the GEMC code. However, such non-microreversible protocol may introduce a bias into the simulations. To ascertain that this does not lead to detectable systematic errors in the calculated thermodynamic quantities, we performed several simulations at various temperature and pressure conditions in which all individual MC move types we drawn randomly with predefined constant probabilities. No systematic deviations to results from our standard procedure were found.

We simulated five demixing curves at temperatures of $T = 1000, 1250, 1500, 1750,$ and 2000 K. Each simulation was conducted with a stoichiometric ratio of 1:1. For every temperature we conducted a simulation procedure as follows. The first simulation for each isotherm was started at the highest pressure of interest. This pressure was always located

View Article Online

Paper

PCCP

deep in the demixing region. Initially, all H₂ and H₂O molecules were placed randomly on simple cubic lattices in each of the boxes. We ran each simulation four times, *i.e.*, with four different initial molar fractions $x_{1,\text{II}}^{\text{H}_2}$ and $x_{1,\text{II}}^{\text{H}_2\text{O}}$. This procedure ensured independence of our results from the initial configurations. The first part of a simulation consisted of 1000 steps for internal equilibration inside each box, during which all particles were attempted to be displaced and the volumes of both boxes were tried to be resized to reach the desired pressure. This internal equilibration process was followed by at least 10 000 global steps. During a global step, attempts to displace or rotate every particle and resize the volumes were made. Additionally, 30 000 particle transfers and 3000 particle swaps were attempted. After the global equilibrium was reached, the molar fractions of the species in each box were calculated by averaging until the simulation end (usually over 5000 of such steps). The number of 5000 steps was chosen so large to diminish errors due to large fluctuations or an insufficiently demixed system. We consistently used final configurations of equilibrated runs to start new runs at the next lower pressure of interest for each isotherm, so that a new equilibrium state was established quickly (usually after 1000 steps). Considering the large number of molecules used in our GEMC simulations, this saved a considerable amount of computation time. The procedure was followed until H₂–H₂O was discovered to be completely miscible. As an example, Fig. 4 shows a simulation with $N = 14\,000$ molecules for a temperature of $T = 1500$ K and pressures of 90 and 80 kbar.

The maximum displacement for particle moves was adjusted to yield an average acceptance rate of 50%. In rotation steps of water molecules, their new orientations were drawn randomly.

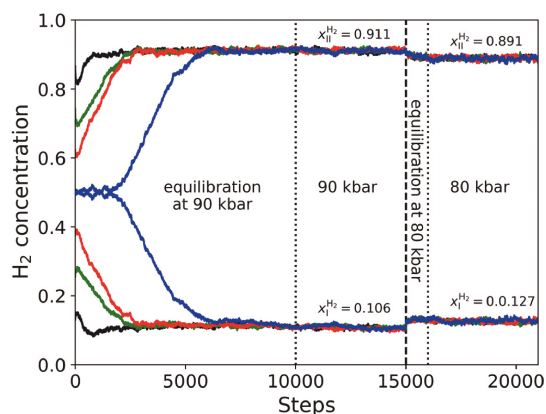


Fig. 4 GEMC simulation at a temperature of $T = 1500$ K for a mixture of H₂–H₂O. The different colors show different initial molar fractions $x_{1,\text{II}}^{\text{H}_2}$ and $x_{1,\text{II}}^{\text{H}_2\text{O}}$. The simulation was started with the highest pressure of interest ($p = 90$ kbar). After 10 000 steps the equilibrium was reached (first black dotted line) and the molar fractions were averaged over 5000 steps (left side of the black dashed line). Then we switched the pressure to $p = 80$ kbar (right side of the black dashed line) and the new equilibrium state was established quickly (second black dotted line), after which the averaging of the molar fractions was made.

The volumes were attempted to be resized independently between $0 < \Delta V < \Delta V_{\text{max}}$ with a predefined value of $\Delta V_{\text{max}} = 1.1 \text{ \AA}$. This choice was found appropriate because it kept the average pressure constant throughout the simulation. The acceptance probability of transfers and swaps became smaller for high pressures; accordingly, the number of global steps was extended.

In extensive convergence tests with more than 30 000 particles, we still found our GEMC simulations to be not yet sufficiently converged due to finite-size effects. We attribute these to the long range of the Stockmayer potential that describes the dipolar interaction between the water molecules. To obtain converged results for the demixing (binodal) curves nonetheless, we performed five sets of simulations with 12 000, 14 000, 16 384, 20 000, and 30 000 molecules for each pressure–temperature condition. We found a very systematic relation between the demixing pressure and the particle number, which allowed us to refine our results by conducting a linear regression over the inverse particle number and subsequent extrapolation to zero. This procedure was followed in two ways inside the pressure/molar-fraction plane to approach the demixing line largely perpendicularly: either the molar demixing fractions were fitted along isobars or the demixing pressures were fitted at lines of a constant molar fraction. In Fig. 5, the procedure is illustrated and explained in more detail for a temperature of $T = 1500$ K. Notably, at low H₂ fractions our results were already converged with 12 000 molecules, whereas finite-size corrections became necessary for hydrogen fractions of $x_{\text{H}_2} > 0.2$. This indicates that increasing the fraction of hydrogen molecules beyond a certain level disturbs the screening of the dipolar interactions between water molecules, which

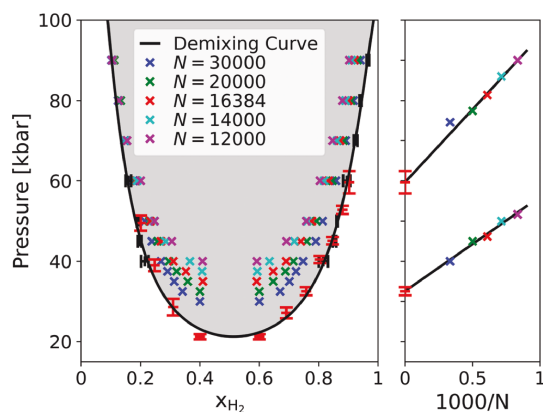


Fig. 5 Demixing of H₂–H₂O at $T = 1500$ K. The left figure shows results of GEMC simulations with different numbers of molecules (colored crosses). The red symbols and error bars are pressures fitted at constant molar fraction concentration while the black symbols and error bars show the demixing fractions fitted at constant pressure. The black line serves as guide to the eye. Demixing occurs within the shaded area. As an example, the right figure shows two linear regressions at constant molar fraction $x_{\text{H}_2} = 0.75$ and $x_{\text{H}_2} = 0.9$.

PCCP

View Article Online

Paper

is very efficient in pure water but not in mixtures with non-polar particles.

By nature of the GEMC method, it is not possible to directly simulate demixing data at the global 1:1 stoichiometric ratio because equilibrium states with molar fractions of $x_{\text{H}_2} = 0.5$ in both boxes correspond to a mixed system. Consequently, an infinite number of particles would be necessary to converge the Gibbs ensemble method in close vicinity of $x_{\text{H}_2} = 0.5$, which is also where the pressure minima occur in our system, see Fig. 5. Accordingly, the demixing ratios close to the lowest pressure at which demixing occurs are always obtained by conducting linear regressions as described above.

We also studied the influence of the cutoff radius r_c for calculating the energies and pressures in the simulation box which has to be half the box length or less, depending on the range of the interaction potentials. Cutoff radii less than half the box length (which would save computing time) led to demixing at systematically higher pressures or the system becoming even completely miscible. This finding also explains the computational origin of the finite size effects explained above. Accordingly, the long-range dipolar $\text{H}_2\text{O}-\text{H}_2\text{O}$ interactions are indeed the cause for these finite-size effects and explain why the GEMC simulations can only fully converge at hydrogen fractions $x_{\text{H}_2} < 0.2$ with less than 30 000 molecules in total. For H_2 fractions $x_{\text{H}_2} > 0.2$, the screening of the long-range dipolar interaction between the H_2O molecules is not sufficient anymore.

4 Results and discussion

We simulated five demixing curves at $T = 1000, 1250, 1500, 1750,$ and 2000 K, which are shown in Fig. 6. Our demixing curves are nearly symmetric but slightly shifted toward higher H_2 fractions. This illustrates that hydrogen dissolves more easily in water than *vice versa*. Such behaviour is plausible because the dipolar intermolecular interactions between water molecules are stronger and anisotropic, which favour molecular configurations that can minimize the electrostatic energy. Such structures cannot form well in an environment of non-polar and more weakly interacting hydrogen molecules so that demixing occurs already at low water fractions.

As mentioned in Section 3, choosing cutoff radii r_c smaller than half the box length led to systematically higher demixing pressures or even to completely miscible systems. Obviously, the long-range dipolar $\text{H}_2\text{O}-\text{H}_2\text{O}$ interactions act as a trigger for $\text{H}_2-\text{H}_2\text{O}$ separation.

Demixing might as well occur at higher pressures than marked by the shaded areas in Fig. 4. We did not attempt to calculate demixing curves at temperatures higher than 2000 K or pressures higher than 150 kbar because our potential models do not allow for the description of molecular dissociation processes that increasingly appear there.^{41,42}

Fig. 7 compares the GEMC simulation results and experimental findings in a p - T plot. The red circles represent the lowest pressure at which demixing occurs for the given

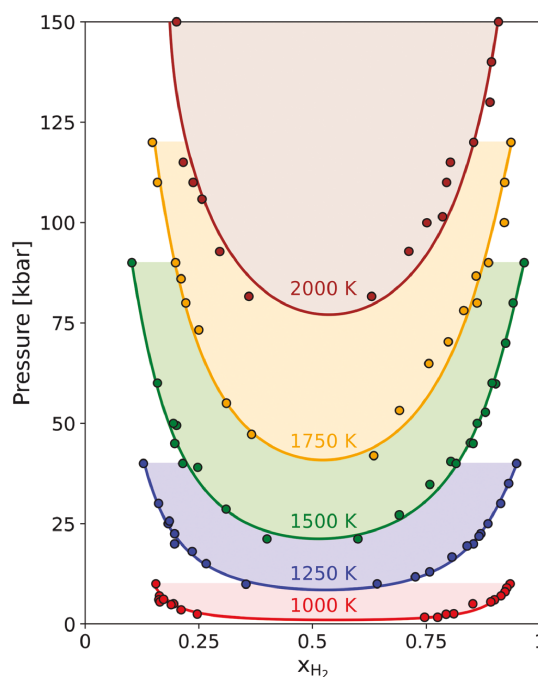


Fig. 6 Demixing curves at different temperatures (color coded). The colored lines serve as guides to the eye. Demixing occurs within the shaded areas; see text.

temperature. Comparing to Fig. 6 this holds for a hydrogen concentration of $x_{\text{H}_2} = 0.5$. Our demixing curve is located above the results of Bali *et al.*,²² *i.e.* at somewhat higher temperatures,

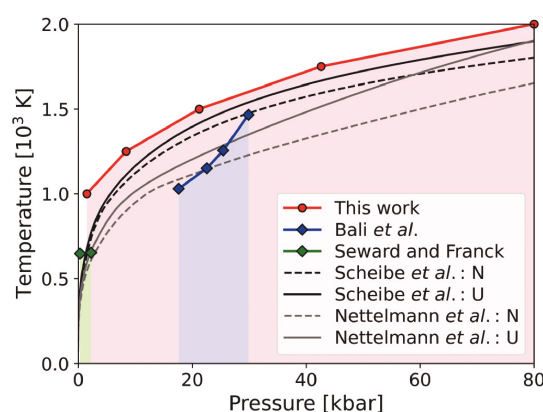


Fig. 7 Pressure-temperature diagram for $\text{H}_2-\text{H}_2\text{O}$ demixing. Red circles represent our results obtained by GEMC simulations at $x_{\text{H}_2} = 0.5$. Blue squares are the experimental results of Bali *et al.*,²² and green squares those of Seward and Franck,²¹ respectively. Demixing may occur under conditions within the shaded areas. Black lines indicate the interior states of Uranus (U) and Neptune (N) as predicted by Scheibe *et al.*,⁵ while grey lines indicate the interior states of Uranus (U) and Neptune (N) as predicted by Nettelmann *et al.*¹¹ in their model no. 2.

View Article Online

Paper

PCCP

and displays a downward curvature. The deviations to the low-pressure results of Seward and Franck²¹ show the same trend, *i.e.*, our results are higher. The lowest pressure at which demixing was reported by Seward and Franck²¹ is located at hydrogen concentrations of $x_{\text{H}_2} \approx 0.8$. Our demixing curve has been simulated for significantly higher temperatures. Accordingly, the comparison between our demixing curve and the results of Seward and Franck²¹ has to be done with caution.

The main reason for the quantitative disagreement between the GEMC results and the experimental data is certainly the use of analytical two-body interaction potentials. This excludes changes in the electronic structure of the molecules that occur in wider ranges of pressure, temperature, and molar fraction. Especially at lower temperatures, the electronic structure of liquid (subcritical) water is increasingly determined by hydrogen bonding and an enhancement of the dipole moment.⁴³ Furthermore, molecular dissociation processes are not taken into account either, which become increasingly important at more extreme pressures and temperatures. A combination of the GEMC method with *ab initio* electronic structure calculation techniques (aiGEMC) was used to calculate the fluid-phase equilibria of water.^{44,45} Nevertheless, the particle number necessary to converge our H₂-H₂O demixing calculations is presently too large for allowing a combination with the aiGEMC method, which would be necessary to obtain results where ionization or dissociation occurs.

Despite the quantitative deviations from experimental data discussed above, our GEMC simulations provide clear evidence that H₂ and H₂O are immiscible under high-pressure and temperature conditions, in contrast to the DFT-MD simulations by Soubiran and Militzer,⁶ who did not observe demixing at all. Their calculations were performed with 48–92 molecules, and in light of our results on the strong influence of long-range dipolar forces on the convergence of molecular simulations in Section 3, this seems to be too small. We, therefore, suggest to revisit and reassess these calculations,⁶ especially because the DFT-MD simulations technique allows, in principle, for a more accurate description than classical interaction potentials do and consistently takes into account dissociation processes. Demixing in the simpler hydrogen–helium system has already been successfully investigated with DFT-MD simulations.^{31,46–49}

The interior states of Neptune and Uranus as calculated by Scheibe *et al.*⁵ and Nettelmann *et al.*¹¹ are located completely within our predicted demixing region; see Fig. 7. Note that our demixing curve has to be checked by performing *ab initio* simulations with a sufficiently large number of particles which is computationally very demanding. Inspecting Fig. 6, H₂-H₂O is predicted to be partially demixed within Uranus and Neptune but not completely. Nevertheless, our results suggest that H₂-H₂O might be immiscible across large regions inside ice giant planets like Neptune and Uranus. Such a miscibility gap has a significant impact on the cooling behaviour of these planets because it provides physical reasoning for density discontinuities or steep compositional gradients. A steep compositional gradient is more stable against convection; accordingly, the

immiscibility of H₂-H₂O might inhibit heat transport by convection between the hydrogen-rich outer layer and the water-rich inner layer. The temperature of the water-rich inner layer might be significantly higher than predicted by fully adiabatic planetary models.^{50,51} In contrast, the outer envelope could be in thermal equilibrium with solar radiation. Our demixing curves indicate that a compositional gradient might develop during the planetary evolution. Accordingly, in earlier and hotter states of planetary evolution above the demixing region, convective heat transport throughout the planet would still be possible.

5 Conclusions

In summary, we have used Gibbs-ensemble Monte Carlo simulations to examine the H₂-H₂O demixing diagram at pressures below $p \leq 150$ kbar and temperatures of $1000 \text{ K} \leq T \leq 2000 \text{ K}$. In doing so, we obtained a clear indication that hydrogen and water demix under high-pressure and -temperature conditions relevant to the interior of ice giant planets. The driving force for H₂-H₂O demixing is characterized by differences between the long-range dipole interactions among H₂O molecules, compared to the short-range van der Waals-like interactions between hydrogen molecules. The calculated H₂-H₂O miscibility gap indicates that demixing of major molecular species in ice giant planets might occur, which would support non-adiabatic models developed to explain the present luminosity of Uranus and Neptune. Our results should not only stimulate further demixing experiments using high-pressure experimental techniques like diamond anvil cells but also spur renewed calculations using *ab initio* methods.

Conflicts of interest

There are no conflicts to declare.

Acknowledgements

We thank Ludwig Scheibe and Manuel Schöttler for helpful discussions. This work was supported by the North German Supercomputing Alliance (HLRN), the ITMZ of the University of Rostock, the Deutsche Forschungsgemeinschaft (DFG) *via* the Research Unit FOR 2440, the Evangelische Studienwerk Villigst as well as by DESY Hamburg *via* the Center for Molecular Water Science (CMWS).

References

- 1 R. Chau, S. Hamel and W. J. Nellis, *Nat. Commun.*, 2011, **2**, 203.
- 2 A. Hermann, N. W. Ashcroft and R. Hoffmann, *Proc. Natl. Acad. Sci. U. S. A.*, 2012, **109**, 745.
- 3 M. Bethkenhagen, E. R. Meyer, S. Hamel, N. Nettelmann, M. French, L. Scheibe, C. Ticknor, L. A. Collins, J. D. Kress, J. J. Fortney and R. Redmer, *Astrophys. J.*, 2017, **848**, 67.

View Article Online

PCCP

Paper

- 4 R. Helled, N. Nettelmann and T. Guillot, *Space Sci. Rev.*, 2020, **216**, 38.
- 5 L. Scheibe, N. Nettelmann and R. Redmer, *Astron. Astrophys.*, 2019, **632**, A70.
- 6 F. Soubiran and B. Militzer, *Astrophys. J.*, 2015, **806**, 1–12.
- 7 N. Nettelmann, K. Wang, J. Fortney, S. Hamel, S. Yellamilli, M. Bethkenhagen and R. Redmer, *Icarus*, 2016, **275**, 107–116.
- 8 W. B. Hubbard and J. J. MacFarlane, *J. Geophys. Res.*, 1980, **85**, 225–234.
- 9 W. B. Hubbard, W. J. Nellis, A. C. Mitchell, N. C. Holmes, S. S. Limaye and P. C. McCandless, *Science*, 1991, **253**, 648.
- 10 M. S. Marley, P. Gómez and M. Podolak, *J. Geophys. Res.*, 1995, **100**, 23349–23353.
- 11 N. Nettelmann, R. Helled, J. Fortney and R. Redmer, *Planet. Space Sci.*, 2013, **77**, 143–151.
- 12 M. Podolak, A. Weizman and M. Marley, *Planet. Space Sci.*, 1995, **43**, 1517–1522.
- 13 M. Podolak, J. Podolak and M. Marley, *Planet. Space Sci.*, 2000, **48**, 143–151.
- 14 R. Helled, J. D. Anderson, M. Podolak and G. Schubert, *Astrophys. J.*, 2010, **726**, 15.
- 15 R. Redmer, T. R. Mattsson, N. Nettelmann and M. French, *Icarus*, 2011, **211**, 798–803.
- 16 N. Nettelmann, J. J. Fortney, U. Kramm and R. Redmer, *Astrophys. J.*, 2011, **733**, 2.
- 17 W. B. Hubbard, *Science*, 1981, **214**, 145.
- 18 J. J. Fortney and N. Nettelmann, *Space Sci. Rev.*, 2010, **152**, 423–447.
- 19 M. Podolak, R. Helled and G. Schubert, *Mon. Not. R. Astron. Soc.*, 2019, **487**, 2653–2664.
- 20 A. Vazan and R. Helled, *Astron. Astrophys.*, 2020, **633**, A50.
- 21 T. M. Seward and E. U. Franck, *Berichte der Bunsengesellschaft fuer physikalische Chemie*, 1981, **85**, 2–7.
- 22 E. Bali, A. Audétat and H. Keppler, *Nature*, 2013, **495**, 220–222.
- 23 F. Soubiran and B. Militzer, *High Energy Density Phys.*, 2015, **17**, 157–161.
- 24 J. P. Perdew, K. Burke and M. Ernzerhof, *Phys. Rev. Lett.*, 1996, **77**, 3865–3868.
- 25 M. Dion, H. Rydberg, E. Schröder, D. C. Langreth and B. I. Lundqvist, *Phys. Rev. Lett.*, 2004, **92**, 246401.
- 26 A. Z. Panagiotopoulos, N. Quirke, M. Stapleton and D. Tildesley, *Mol. Phys.*, 1988, **63**, 527–545.
- 27 A. Z. Panagiotopoulos, *Mol. Phys.*, 1987, **61**, 813–826.
- 28 A. Z. Panagiotopoulos, *Mol. Simul.*, 1992, **9**, 1–23.
- 29 M. Ross, F. H. Ree and D. A. Young, *J. Chem. Phys.*, 1983, **79**, 1487–1494.
- 30 A. Bergermann, M. French, M. Schöttler and R. Redmer, *Phys. Rev. E*, 2021, **103**, 013307.
- 31 M. Schöttler and R. Redmer, *J. Plasma Phys.*, 2019, **85**, 945850201.
- 32 W. H. Stockmayer, *J. Chem. Phys.*, 1941, **9**, 398–402.
- 33 G. Weck, J. Eggert, P. Loubeyre, N. Desbiens, E. Bourasseau, J.-B. Maillat, M. Mezouar and M. Hanfland, *Phys. Rev. B: Condens. Matter Mater. Phys.*, 2009, **80**, 180202.
- 34 E. Schwegler, G. Galli and F. M. C. Gygi, *Phys. Rev. Lett.*, 2000, **84**, 2429–2432.
- 35 J. Aubreton, M. F. Elchinger and J. M. Vinson, *Plasma Chem. Plasma Process.*, 2009, **29**, 149–171.
- 36 D. Adams and E. Adams, *Mol. Phys.*, 1981, **42**, 907–926.
- 37 W. Wagner and A. Pruß, *J. Phys. Chem. Ref. Data*, 2002, **31**, 387–535.
- 38 H. M. Hulburt and J. O. Hirschfelder, *J. Chem. Phys.*, 1941, **9**, 61–69.
- 39 M. P. Hodges, R. J. Wheatley, G. K. Schenter and A. H. Harvey, *J. Chem. Phys.*, 2003, **120**, 710–720.
- 40 J. A. Schouten, A. de Kuijper and J. P. J. Michels, *Phys. Rev. B: Condens. Matter Mater. Phys.*, 1991, **44**, 6630–6634.
- 41 E. Schwegler, G. Galli, F. Gygi and R. Q. Hood, *Phys. Rev. Lett.*, 2001, **87**, 265501.
- 42 M. French and R. Redmer, *J. Phys.: Condens. Matter*, 2009, **21**, 375101.
- 43 F. Franks, *The Physics and Physical Chemistry of Water*, Plenum Press, 1972.
- 44 M. J. McGrath, J. I. Siepmann, I.-F. W. Kuo, C. J. Mundy, J. VandeVondele, J. Hutter, F. Mohamed and M. Krack, *J. Phys. Chem. A*, 2006, **110**, 640–646.
- 45 K. Leonhard and U. K. Deiters, *J. Phys. Chem. B*, 2018, **122**, 3318–3329.
- 46 W. Lorenzen, B. Holst and R. Redmer, *Phys. Rev. Lett.*, 2009, **102**, 115701.
- 47 M. A. Morales, S. Hamel, K. Caspersen and E. Schwegler, *Phys. Rev. B: Condens. Matter Mater. Phys.*, 2013, **87**, 174105.
- 48 M. Schöttler and R. Redmer, *Phys. Rev. Lett.*, 2018, **120**, 115703.
- 49 J. Vorberger, I. Tamblyn, B. Militzer and S. A. Bonev, *Phys. Rev. B: Condens. Matter Mater. Phys.*, 2007, **75**, 024206.
- 50 L. Scheibe, N. Nettelmann and R. Redmer, *Astron. Astrophys.*, accepted.
- 51 E. Bailey and D. Stevenson, *Planet. Sci. J.*, 2021, **2**, 64.

6.3. *Ab Initio* calculation of the miscibility diagram for hydrogen and water

Author contributions:

- **A. Bergermann:** Preparation of the manuscript, conducting DFT-MD simulations, conduction the coupling constant integration, interpretation of the results
- **M. French:** Preparation of the manuscript, discussion of the numerical methods and their impact, interpretation of the results
- **R. Redmer:** Supervision of the project, preparation of the manuscript, interpretation of the results and their impact on ice giant planets

Ab Initio Calculation of the Miscibility Diagram for Mixtures of Hydrogen and Water

Armin Bergermann, Martin French, and Ronald Redmer
Institut für Physik, Universität Rostock, D-18051 Rostock, Germany
 (Dated: January 5, 2024)

We calculate the miscibility gap in mixtures of hydrogen and water under high-temperature and high-pressure conditions as relevant for planetary interiors with density functional theory combined with classical molecular dynamics. In contrast to earlier calculations, we find a miscibility gap at temperatures below 1500-2000 K at pressures of up to 300 kbar, which extends the experimentally known immiscibility region by one order of magnitude in pressure. In contrast to extrapolated experimental demixing lines reaching to high temperatures, our results indicate a termination of the demixing region close to 2000 K. This finding profoundly impacts the understanding the interiors of ice-giant planets like Neptune and Uranus by supporting a partially demixed interior, including a density discontinuity near 2000 K, which corresponds to planetary radii of 0.85 - 0.95 in Uranus and Neptune. Additionally, our findings are relevant for thermal evolution models of Earth that aim to explain the formation of super-reducing mineral associations.

Introduction: Neptune and Uranus are usually assumed to be ice-giant planets, consisting mostly of mixtures of the ice-forming compounds water, ammonia, and methane [1–3]. Since space probe missions to these ice-giants are utterly challenging and expensive [4, 5], knowledge gain on the interior structures of Uranus and Neptune mainly relies on the development and improvement of models [3, 6–8]. For instance, an adiabatic temperature profile with three distinct layers, a rocky core, an inner layer rich in water, ammonia, and methane, and an outer layer rich in H₂ and He is proposed [1, 6, 9–14]. These relatively simple models have density discontinuities at the boundaries between the three layers, which were assumed to keep the number of degrees of freedom as low as possible. Nevertheless, alternative classes of models of Uranus and Neptune with a continuous density profile were also developed [15, 16]. In general, adiabatic interior models cannot explain the thermal evolution and very different brightnesses of Uranus and Neptune [17, 18], which hints towards much more complex interior structures being present in ice-giants [19]. Any credible planetary model needs to be based on a reliable thermophysical material database for the equation of state and phase diagram of the constituent mixture of compounds. For instance, an immiscibility region of H₂ and H₂O in the interior of Uranus and Neptune could indeed lead to layer formation accompanied by density discontinuities in the planets’ interiors [1, 6, 10, 11, 20]. The demixing process would also inhibit heat transport by convection, invalidating the assumption of an adiabatic interior and necessitating non-adiabatic models. Several non-adiabatic models have already been proposed by, e.g., Nettelmann *et al.* [14] and Scheibe *et al.* [18], to explain thermal evolution and brightness, assuming that primordial heat is trapped inside the planet. Recently, Bailey and Stevenson [21] discussed the impact of an H₂-H₂O miscibility gap in Uranus and Neptune. They found that the partial immiscibility of hydrogen and water could offer a solution to questions regarding

the structure, magnetic field, and thermal evolution of ice-giant planets.

In a different context, Bali *et al.* [22] pointed out that demixing in hydrogen and water could also decrease oxygen fugacity in Earth’s mantle, making the formation of super-reducing mineral associations plausible. Additionally, it has been suggested that a miscibility gap between water and hydrogen had caused rapid upper mantle oxidation [22–24].

Therefore, the determination of the miscibility gap in mixtures of hydrogen and water under high-pressure and high-temperature conditions is of paramount importance for better understanding the interior and evolution of ice-giant planets [14, 16–18, 21] but also plays a vital role in the evolution of Earth and Earth-like extrasolar planets [22].

So far, three experimental studies have investigated the immiscibility region in water and hydrogen: In 1981, Seward and Franck [25] performed experiments in pressure vessels and determined immiscibility up to pressures of 2.3 kbar and temperatures of 650 K. In 2013, Bali *et al.* [22] used Raman spectroscopy to determine whether hydrogen and water entrapments in silicates can demix. They explored the respective miscibility gap at temperatures between 1000 K and 1500 K and pressures between 17 kbar and 25 kbar. In 2023, Vlasov *et al.* [24] used a similar experimental technique and confirmed the experimental findings of Bali *et al.* [22].

Interestingly, the experiments by Bali *et al.* [22] and Vlasov *et al.* [24] resulted in a demixing line with an upward curvature, which would lead to a very large demixing region extending to temperatures of several 1000 K when extrapolated. However, fundamental thermodynamics of mixtures requires termination of any demixing region at some temperature as the entropy rises [26, 27], which occurs probably at pressure conditions that cannot be reached within current experimental setups. Such limitations of achievable pressures and temperatures in experiments necessitate a theoretical investigation of

this demixing process using state-of-the-art techniques of computational many-particle physics [28–30].

Up to now, two contradicting theoretical predictions regarding the immiscibility of H₂ and H₂O are available. In 2015, Soubiran and Militzer [31] predicted H₂ and H₂O mixtures to be completely miscible by calculating the free enthalpy of mixing. They combined density functional theory (DFT) with molecular dynamics (MD). The coupling-constant integration technique [32] (CCI) was used to determine the non-ideal entropy of the H₂-H₂O mixtures.

Recently, Bergermann *et al.* [36] conducted Gibbs ensemble Monte-Carlo (GEMC) simulations using analytical two-body interaction potentials to describe the interaction between the molecular species H₂ and H₂O. A demixing diagram was predicted at pressures below 150 kbar and temperatures of 1000K < T < 2000 K. Notably, the isentropes of Neptune and Uranus and the archean geotherms are within the demixing region predicted by Bergermann *et al.* [36].

In this work, we reinvestigate the miscibility diagram of hydrogen and water using *ab initio* simulations based on density functional theory combined with molecular dynamics (DFT-MD). We calculate the free enthalpy of mixing at temperatures between 1000 and 2000 K and pressures between 40 and 300 kbar. The CCI method [32] was used to determine the non-ideal entropy, similarly to Soubiran and Militzer [31]. We consider nuclear quantum corrections (NQC) of the ionic motion using a post-processing method designed by Berens *et al.* [38, 39]. This procedure influences the results significantly, as the immiscibility region is widened, which is shown below. A detailed explanation of the numerical techniques used is given in the Supplemental Material. In contrast to Soubiran and Militzer [31], our simulations provide strong evidence for a miscibility gap in mixtures of hydrogen and water under high-pressure and high-temperature conditions, in agreement with the experimental findings and the GEMC simulations.

Methods: We calculate the miscibility of hydrogen and water by evaluating differences in the free enthalpy in dependence on the water concentration. By doing so, we can determine whether the two substances are likely to form a homogeneous mixture or separate into two distinct phases. The free enthalpy per molecule g of the mixture is given by:

$$\frac{G}{N_{H_2} + N_{H_2O}} = g = u + pv - Ts, \quad (1)$$

where u is the internal energy per molecule, p is the pressure, v is the volume per molecule, T is the temperature, and s is the entropy per molecule, G is the total free enthalpy, and N_{H_2} and N_{H_2O} are the numbers of hydrogen and water molecules, respectively. The free enthalpy of

mixing is defined as

$$\Delta g(p, T, x) = g(p, T, x) - xg(p, T, 1) - (1-x)g(p, T, 0), \quad (2)$$

where $g(p, T, x)$ is the free enthalpy of the mixture, $g(p, T, 1)$ the free enthalpy of pure water, and $g(p, T, 0)$ that of pure hydrogen. Herein, x defines the molecular water fraction as follows

$$x = \frac{N_{H_2O}}{N_{H_2} + N_{H_2O}}. \quad (3)$$

A concave region suggests that the mixture is unstable and demixes into two phases with different concentrations [31, 33–35, 40]. By fitting $\Delta g(T, p, x)$ using a Redlich-Kister ansatz [41] and applying a double-tangent construction to $\Delta g(T, p, x)$, the concentrations of the water-poor and water-rich regions of the demixed fluid can be determined [27, 34, 35, 40].

The thermodynamic variables p , T , u , and v are a direct output of our DFT-MD simulations. In contrast, the entropy is not directly available from the DFT-MD simulations. Unfortunately, the simplest approximation, the ideal molecular entropy of mixing, is insufficient for this purpose [34]. Therefore, we use the CCI method to calculate the nonideal entropy of the system of interacting molecules. Furthermore, we augment our simulation data for classical particles with the correction procedure of Berens *et al.* [39] to take into account NQC to the ionic motion. A more detailed description of the methods is given in the Supplemental Material.

Fig. 1 illustrates the influences of the nonideal entropy and of NQC, two aspects that counteract with each other on results for the free enthalpy of mixing Δg , at 120 kbar and 1000 K. Using the ideal molecular mixing entropy and no NQC (grey dashed line), we found a small miscibility region for water concentrations of $0.1 < x < 0.6$. The dotted lines represent the constructed double tangents. Using the nonideal entropy instead generally decreases the free enthalpy of mixing and reduces the concave section, which enhances the tendency of hydrogen and water to mix. Therefore, only slight indications for demixing are visible when nuclei are treated as classical particles (red dashed line). By including the NQC (solid red line), however, the concave region is widened, and we find a sizeable immiscibility region for water concentrations of $0.1 < x < 0.85$.

The trends explained above are similar to what was found in earlier work on hydrogen-helium mixtures, where Schöttler *et al.* [34, 35] observed that NQC contributed significantly to Δg and enhanced the immiscibility in the molecular regime. For certain conditions, Schöttler *et al.* [34, 35], did not find any indication for demixing without the NQC either. These results underline the importance of the NQC when calculating the miscibility gap in molecular mixtures. Microscopically, NQC originate mainly from changes in the vibrational properties of the molecules with x in our method.

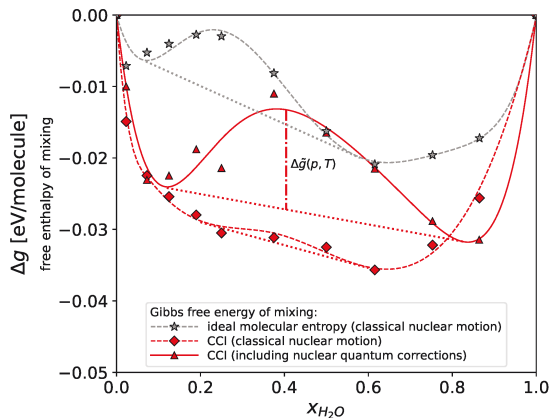


FIG. 1. Free enthalpy of mixing Δg as function of the water fraction $x_{\text{H}_2\text{O}}$ for 1000 K and 120 kbar. Results from classical nuclear motion using the ideal molecular entropy: grey stars. Results calculated with the CCI method are shown in red, specifically: using the classical nuclear motion as red diamonds, by including the NQC as red triangles. The double-tangent constructions are depicted as dotted lines in all cases. The dash-dotted line quantifies the size of the free enthalpy salient (concave section) $\Delta\tilde{g}(p, T)$, see Eq. (4).

Our results contradict the findings of Soubiran and Militzer [31], who found no demixing at all, partially because they did not take into account NQC. Furthermore, they applied less stringent convergence criteria in their DFT-MD simulation parameters. We were able to use up to two times more particles, two times more concentrations, up to two times more λ -integration points, and up to ten times longer simulation runs to diminish fluctuations and to obtain more precise results. A detailed overview of the simulation parameters and comparison with results by Soubiran and Militzer [31] is given in the Supplemental Material.

Results for the Demixing Region: Our main results for Δg at nine different p - T conditions are shown in Fig. 2. The free enthalpy of mixing is smallest for the lowest temperature (1000 K, left) and the lowest pressure (40 kbar). Increasing the temperature leads to a general decrease in Δg , a typical sign of temperature-enhanced solubility of water and hydrogen in each other. The same behaviour occurs as the pressure is decreased, which reduces the influence of molecular interactions and effectively increases the ideality of the mixture.

At four conditions (1000 K: 80 kbar and 120 kbar; 1500 K: 120 kbar and 200 kbar), the free enthalpies of mixing show very pronounced concave behaviours, which implies that water and hydrogen are demixed there.

At the remaining five conditions (1000 K: 40 kbar; 1500: 40 kbar; 2000 K: 120 kbar, 200 kbar, and 300 kbar), we deem the numerical precision of the data points may

not be sufficient to warrant the deduction of a significant concave region, although Redlich-Kister fit curves with slightly concave sections can be derived. Especially at the highest temperature of 2000 K (right panel in Fig. 2), the relatively straight sections in the Redlich-Kister fits indicate that this temperature is close to the highest one at which demixing can be expected in the pressure range between 120 and 300 kbar. The same holds for the condition of 1500 K and 40 kbar.

We did not calculate the free enthalpy for $p > 300$ kbar because these conditions intersect with the melting line of water [42–49]. The treatment of melting is not feasible within the present simulations approach. Likewise, it was not feasible to calculate the free enthalpy of mixing at pressures below 40 kbar because the DFT-MD simulations would have been computationally too expensive to obtain sufficiently precise results for Δg .

In general, the behaviour of Δg in p - T space indicates that increasing the temperature reduces the miscibility gap in hydrogen-water mixtures. According to our data, hydrogen and water tend to become completely miscible above 2000 K between 40 and 300 kbar.

To quantify the demixing region, i.e., to determine the demixing line $T_d(p)$ which separates the miscible region from potentially demixed states, we quantify the size of the concave sections in our nine free enthalpy by determining the differences between $\Delta g(p, T, x)$ and the respective double tangent $\Delta g_t(p, T, x)$ at each value $x_i(p, T)$ where both functions have the same slope:

$$\Delta\tilde{g}(p, T) = \Delta g(p, T, x_i) - \Delta g_t(p, T, x_i), \quad (4)$$

see also Fig. 1 for an illustrative example. The quantity $\Delta\tilde{g}(p, T)$ shows a systematic behaviour with p and T , see Fig. 3. The following functional form,

$$\Delta\tilde{g}(p, T) = a + bp + (c + ep)T^d, \quad (5)$$

where a, b, c, d, e are coefficients given in Tab. I, allows for an accurate mathematical representation of $\Delta\tilde{g}(p, T)$, see Fig. 3.

The zero of $\Delta\tilde{g}(p, T)$ naturally defines the lowest pressure $p(T)$ at which demixing occurs in the p - T plane. These values represent the demixing line $T_d(p)$ that is shown as green line in Fig. 4.

Fig. 4, also includes experimental results for demixing [22, 24, 25] and planetary isentropes [12, 17]. Our demixing region is close to experimental results of Bali *et al.* [22] (blue line) and Vlasov *et al.* [24] (cyan line), deviating only by ≈ 2.5 kbar between 1000 and 1500 K and has a similarly steep slope as those from the experiments. However, at pressures above 50 kbar, our demixing line bends to the right and becomes nearly constant in temperature above 100 kbar. Interestingly, earlier results obtained from GEMC simulations which use classical pair potentials [36] (red circles) are also in the vicinity of the present results.

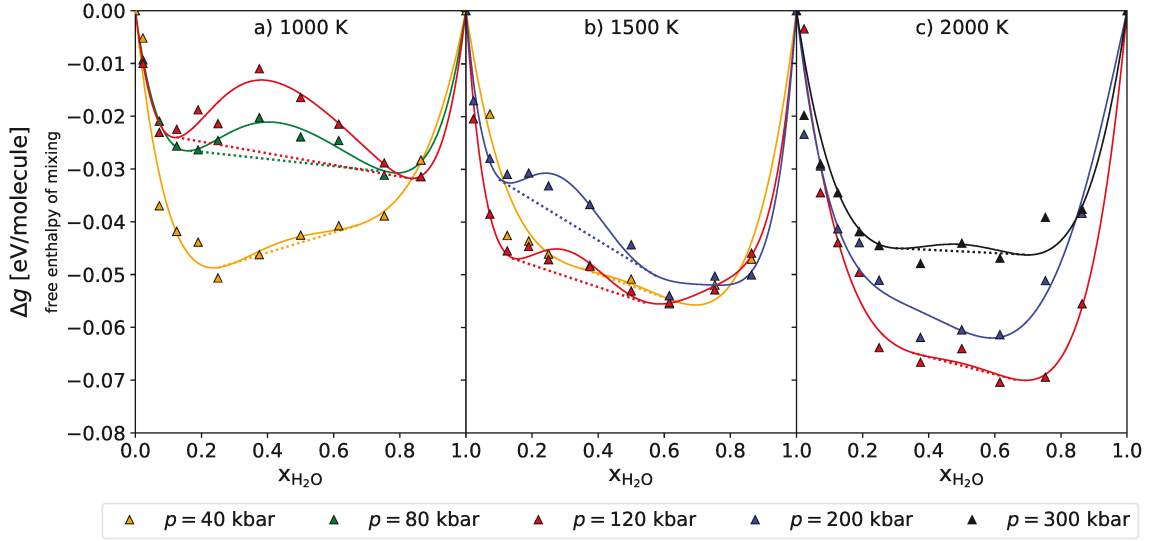


FIG. 2. Gibbs free energy of mixing Δg for different p - T conditions. Panel a), b), and c) show Δg for $T = 1000$, 1500 , and 2000 K, respectively. We considered five pressures: $p = 40$ kbar (orange), $p = 80$ kbar (green), $p = 120$ kbar (red), $p = 200$ kbar (blue), and $p = 300$ kbar (black). Our raw data are given by colored triangles. The solid lines are respective Redlich-Kister fits [41]. The dashed lines represent the subsequent double tangent constructions.

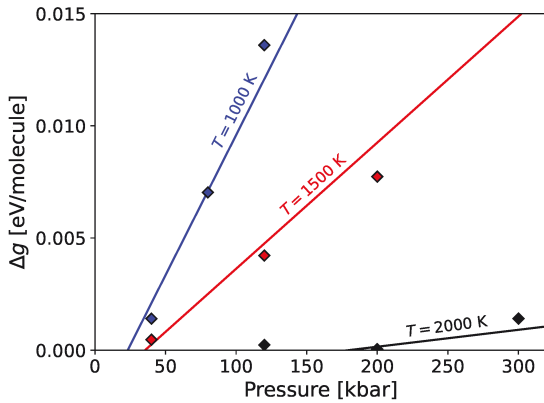


FIG. 3. Results for $\Delta\hat{g}(p, T)$ at 1000 K (blue), 1500 K (red), and 2000 K (black). The solid lines represent the corresponding fit from Eq. (5), which has a linear pressure dependence.

Concluding this section, our results agree with the experimentally known immiscibility region and extend this region by one order of magnitude in pressure. For pressures above 100 kbar, we predict the highest temperature where demixing occurs to be almost constant. Thus, hydrogen and water become completely miscible above 2000 K.

Impact on ice giants The p - T diagram of water-

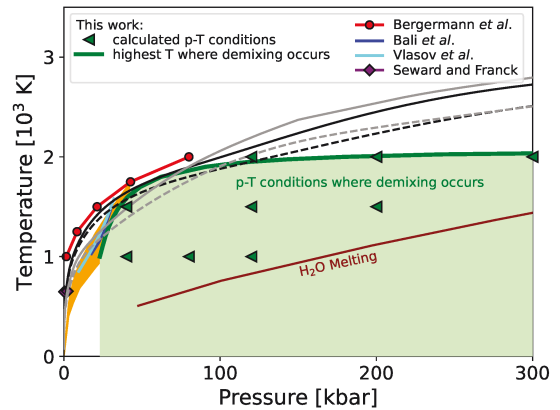


FIG. 4. T - p diagram with all conditions for which we calculated Δg (green triangles). The green demixing line $T_d(p)$ shows the lowest pressure and highest temperatures where demixing occurs according to the condition $\Delta\hat{g}(p, T) = 0$, see Eq. (5). For comparison we show GEMC results of Bergermann *et al.* [36] (red circles), experiments by Bali *et al.* [22] (blue line), experiments by Seward and Franck [25] (purple diamonds), and experiments by Vlasov *et al.* [24] (cyan line). The melting line of water is shown in dark-red [51]. Predicted T - p profiles along Uranus' and Neptune's radius are shown by solid and dashed lines, respectively: Scheibe *et al.* [17] (black) and Nettelmann *et al.* [12] (model N1: grey). We also added Earth's archaic geotherms as given by Mareschal and Jaupart [52] (orange shaded area).

TABLE I. Coefficients for the fit formula, Eq. 5.

a [eV]	b [eV/kbar]	c [eV/K]	d	e [eV/(K×kbar)]
-3.1119382	0.2364756	3.0937059	0.0007158	-0.235185

hydrogen mixtures shown in Fig. 4 indicates that the thermal profiles through the ice giants Uranus and Neptune intersect the demixing area calculated in this work. Therefore, we expect hydrogen and water to be immiscible in the ice-giants in our Solar System.

According to the planetary model N1 for Neptune by Nettelmann *et al.* [12], immiscibility of hydrogen and water can occur at radii between $r_N = 0.86R_N$ and $r_N = 0.93R_N$, where $R_N = 24622$ km denotes the radius of Neptune. They predict a jump in density at $r_{N\rho} = 0.86R_N$ which is within our demixing region. For the planetary model of Uranus [12] immiscibility of hydrogen and water can occur at radii between $r_U = 0.83R_U$ and $r_U = 0.87R_U$, where $R_U = 25362$ km denotes the radius of Uranus. The jump in density is predicted at $r_{U\rho} = 0.77R_U$ and therefore very close to our demixing region. Note, however, that a certain minimum concentration of water is required to cause demixing of hydrogen and water, which depends nonlinearly on p and T . Fig. 2 indicates that demixing occurs when the water fraction reaches approximately $\approx 15\%$ at temperatures of 1000 K and 1500 K. Furthermore, demixing of hydrogen and water may likewise occur in Neptune-like exoplanets [53, 54], especially in older and, therefore, cooler ice giants or in those with similarly large orbits as Uranus and Neptune.

The miscibility gap of hydrogen and water supports the assumption of density discontinuities inside ice-giant planets. Therefore, more complex planetary models than the adiabatic interior assumption are required to explain heat transport from the warm-to-hot center towards the cool surface [15]. For example, Nettelmann *et al.* [12] proposed a model with a boundary at about $p = 100$ kbar and $T = 2000$ K. At these T - p conditions, hydrogen and water might be immiscible, resulting in a stably stratified layer with a density jump. Therefore, heat transport by convection would be inhibited, leading to primordial heat trapped inside the planet, while the relatively thin outer layer is cooling rapidly, see Scheibe *et al.* [18] for a detailed study. This could explain why Uranus has already reached the equilibrium temperature with the Sun.

Furthermore, our demixing curve intersects with Earth's Archean geotherms as well. Therefore, our results support the assumption of the formation of super-reducing mineral associations and rapid upper mantle oxidation [22–24] and subsequently influence the evolution of Earth and Earth-like exoplanets.

In conclusion, our work provides novel predictions for the miscibility gap of hydrogen and water mixtures at

pressures and temperatures, and especially quantifies the p - T region in which the demixing terminates in the interior. These findings will help to better understand giant ice planets like Neptune and Uranus but also Neptune-like exoplanets, which is a very common class of exoplanets. Our findings provide valuable insights that will aid in developing new planetary models capable of addressing long-standing scientific questions regarding the structure and evolution of Uranus and Neptune and influence future space missions [4]. Additionally, the hydrogen and water miscibility gap significantly influences our understanding of Earth and Earth-like extrasolar planets' evolution.

We thank Ludwig Scheibe, Gerd Steinle-Neumann, Nadine Nettelmann, and Hanns-Peter Liermann for fruitful discussions. This work was supported by the North German Supercomputing Alliance (HLRN), the ITMZ of the University of Rostock, the Deutsche Forschungsgemeinschaft (DFG) via the Research Unit FOR 2440, the Evangelische Studienwerk Villigst, and by DESY Hamburg via the Center for Molecular Water Science (CMWS).

-
- [1] W. B. Hubbard and J. J. MacFarlane, *J. Geophys. Res.* **85**, 225 (1980).
 - [2] W. B. Hubbard, *Science* **214**, 145 (1981).
 - [3] J. J. Fortney and N. Nettelmann, *Space Sci. Rev.* **152**, 423 (2010).
 - [4] C. Arridge, N. Achilleos, J. Agarwal, C. Agnor, R. Ambrosi, N. André, S. Badman, K. Baines, D. Banfield, M. Barthélémy, M. Bisi, J. Blum, T. Bocanegra-Bahamon, B. Bonfond, C. Bracken, P. Brandt, C. Briand, C. Briois, S. Brooks, J. Castillo-Rogez, T. Cavalié, B. Christophe, A. Coates, G. Collinson, J. Cooper, M. Costa-Sitja, R. Courtin, I. Daglis, I. de Pater, M. Desai, D. Dirkx, M. Dougherty, R. Ebert, G. Filacchione, L. Fletcher, J. Fortney, I. Gerth, D. Grassi, D. Grodent, E. Grün, J. Gustin, M. Hedman, R. Helled, P. Henri, S. Hess, J. Hillier, M. Hofstadter, R. Holme, M. Horanyi, G. Hospodarsky, S. Hsu, P. Irwin, C. Jackman, O. Karatekin, S. Kempf, E. Khalisi, K. Konstantinidis, H. Krüger, W. Kurth, C. Labianidis, V. Lainey, L. Lamy, M. Laneuville, D. Lucchesi, A. Luntzer, J. MacArthur, A. Maier, A. Masters, S. McKenna-Lawlor, H. Melin, A. Milillo, G. Moragas-Klostermeyer, A. Morschhauser, J. Moses, O. Mousis, N. Nettelmann, F. Neubauer, T. Nordheim, B. Noyelles, G. Orton, M. Owens, R. Peron, C. Plainaki, F. Postberg, N. Rambaux, K. Retherford, S. Reynaud, E. Roussos, C. Russell, A. Rymer, R. Sallantin, A. Sánchez-Lavega, O. Santolik, J. Saur, K. Sayanagi, P. Schenk, J. Schubert, N. Ser-

- gis, E. Sittler, A. Smith, F. Spahn, R. Srama, T. Stalard, V. Sterken, Z. Sternovsky, M. Tiscareno, G. Tobie, F. Tosi, M. Trieloff, D. Turrini, E. Turtle, S. Vinatier, R. Wilson, and P. Zarka, *Planetary and Space Science* **104**, 122 (2014).
- [5] A. Masters, N. Achilleos, C. Agnor, S. Campagnola, S. Charnoz, B. Christophe, A. Coates, L. Fletcher, G. Jones, L. Lamy, F. Marzari, N. Nettelmann, J. Ruiz, R. Ambrosi, N. Andre, A. Bhardwaj, J. Fortney, C. Hansen, R. Helled, G. Moragas-Klostermeyer, G. Orton, L. Ray, S. Reynaud, N. Sergis, R. Srama, and M. Volwerk, *Planetary and Space Science* **104**, 108 (2014).
- [6] R. Helled, N. Nettelmann, and T. Guillot, *Space S. Rev.* **216**, 38 (2020).
- [7] R. Helled and T. Guillot, in *Handbook of Exoplanets* (Springer International Publishing, 2018) pp. 167–185.
- [8] T. Guillot, *Experimental Astronomy* **54**, 1027 (2022).
- [9] W. B. Hubbard, W. B., W. J. Nellis, W. J., A. C. Mitchell, A. C., N. C. Holmes, N. C., S. S. Limaye, and P. C. McCandless, *Science* **253**, 648 (1991).
- [10] M. S. Marley, P. Gómez, and M. Podolak, *J. Geophys. Res.* **100**, 23349 (1995).
- [11] M. Podolak, A. Weizman, and M. Marley, *Planet. and Space Sci.* **43**, 1517 (1995).
- [12] N. Nettelmann, R. Helled, J. Fortney, and R. Redmer, *Planet. and Space Sci.* **77**, 143 (2013).
- [13] M. Bethkenhagen, E. R. Meyer, S. Hamel, N. Nettelmann, M. French, L. Scheibe, C. Ticknor, L. A. Collins, J. D. Kress, J. J. Fortney, and R. Redmer, *Astrophys. J.* **848**, 67 (2017).
- [14] N. Nettelmann, K. Wang, J. Fortney, S. Hamel, S. Yellamilli, M. Bethkenhagen, and R. Redmer, *Icarus* **275**, 107 (2016).
- [15] M. Podolak, R. Helled, and G. Schubert, *Mon. Not. R. Astron. Soc.* **487**, 2653 (2019).
- [16] R. Helled and J. J. Fortney, *Philosophical Transactions of the Royal Society A: Mathematical, Physical and Engineering Sciences* **378**, 20190474 (2020).
- [17] L. Scheibe, N. Nettelmann, and R. Redmer, *Astron. Astrophys.* **632**, A70 (2019).
- [18] L. Scheibe, N. Nettelmann, and R. Redmer, *A&A* **650**, A200 (2021).
- [19] M. French and N. Nettelmann, *The Astrophysical Journal* **881**, 81 (2019).
- [20] M. Podolak, J. Podolak, and M. Marley, *Planet. and Space S.* **48**, 143 (2000).
- [21] E. Bailey and D. J. Stevenson, *The Planetary Science Journal* **2**, 64 (2021).
- [22] E. Bali, A. Audétat, and H. Keppler, *Nature* **495**, 220 (2013).
- [23] Z. D. Sharp, F. M. McCubbin, and C. K. Shearer, *Earth and Planetary Science Letters* **380**, 88 (2013).
- [24] K. Vlasov, A. Audétat, and H. Keppler, *Contrib. to Mineral. Petrol.* **178**, 36 (2023).
- [25] T. M. Seward and E. U. Franck, *Berichte der Bunsengesellschaft für physikalische Chemie* **85**, 2 (1981).
- [26] S. M. Walas, *Phase Equilibria in Chemical Engineering* (Butterworth-Heinemann, 1985).
- [27] M. de Oliveira, *Equilibrium Thermodynamics*, Graduate Texts in Physics (Springer Berlin Heidelberg, 2014).
- [28] D. Marx and J. Hutter, *Ab initio molecular dynamics: basic theory and advanced methods* (Cambridge Univ. Press, Cambridge, 2009).
- [29] M. J. Gillan, D. Alfè, J. Brodholt, L. Vočadlo, and G. D. Price, *Rep. Prog. Phys.* **69**, 2365 (2006).
- [30] F. Graziani, M. Desjarlais, R. Redmer, and S. Trickey, *Frontiers and Challenges in Warm Dense Matter*, Lecture Notes in Computational Science and Engineering (Springer International Publishing, 2014).
- [31] F. Soubiran and B. Militzer, *Astrophys. J.* **806**, 1 (2015).
- [32] J. G. Kirkwood, *The Journal of Chemical Physics* **3**, 300 (1935).
- [33] M. A. Morales, S. Hamel, K. Caspersen, and E. Schwegler, *Phys. Rev. B* **87**, 174105 (2013).
- [34] M. Schöttler and R. Redmer, *Phys. Rev. Lett.* **120**, 115703 (2018).
- [35] M. Schöttler and R. Redmer, *J. Plasma Phys.* **85**, 945850201 (2019).
- [36] A. Bergermann, M. French, and R. Redmer, *Phys. Chem. Chem. Phys.* **23**, 12637 (2021).
- [37] M. French, *New Journal of Physics* **21**, 023007 (2019).
- [38] M. Bethkenhagen, M. French, and R. Redmer, *The Journal of Chemical Physics* **138**, 234504 (2013).
- [39] P. H. Berens, D. H. J. Mackay, G. M. White, and K. R. Wilson, *J. Chem. Phys.* **79**, 2375 (1983).
- [40] W. Lorenzen, B. Holst, and R. Redmer, *Phys. Rev. Lett.* **102**, 115701 (2009).
- [41] O. Redlich and A. T. Kister, *Industrial & Engineering Chemistry* **40**, 345 (1948).
- [42] T. Kimura and M. Murakami, *The Journal of Chemical Physics* **158**, 134504 (2023).
- [43] J.-F. Lin, E. Gregoryanz, V. V. Struzhkin, M. Somayazulu, H.-k. Mao, and R. J. Hemley, *Geophysical Research Letters* **32** (2005).
- [44] E. Schwegler, M. Sharma, F. Gygi, and G. Galli, *Natl. Acad. Sci. Lett.* **39**, 14779 (2008).
- [45] R. Redmer, T. R. Mattsson, N. Nettelmann, and M. French, *Icarus* **211**, 798 (2011).
- [46] J.-A. Queyroux, J.-A. Hernandez, G. Weck, S. Ninet, T. Plisson, S. Klotz, G. Garbarino, N. Guignot, M. Mezouar, M. Hanfland, J.-P. Itié, and F. Datchi, *Phys. Rev. Lett.* **125**, 195501 (2020).
- [47] B. Schwager, L. Chudinovskikh, A. Gavriluk, and R. Boehler, *Journal of Physics: Condensed Matter* **16**, S1177 (2004).
- [48] B. Schwager and R. Boehler, *High Pressure Research* **28**, 431 (2008).
- [49] T. Kimura, Y. Kuwayama, and T. Yagi, *The Journal of Chemical Physics* **140**, 074501 (2014).
- [50] M. A. Morales, E. Schwegler, D. Ceperley, C. Pierleoni, S. Hamel, and K. Caspersen, *Proc. Natl. Acad. Sci.* **106**, 1324 (2009).
- [51] L. Zhang, H. Wang, R. Car, and W. E, *Phys. Rev. Lett.* **126**, 236001 (2021).
- [52] J.-C. Mareschal and C. Jaupart, *Washington DC American Geophysical Union Geophysical Monograph Series* **164**, 61 (2006).
- [53] E. A. Petigura, A. W. Howard, and G. W. Marcy, *Proc. Natl. Acad. Sci. U.S.A.* **110**, 19273 (2013).
- [54] L. Zeng, S. B. Jacobsen, D. D. Sasselov, M. I. Petaev, A. Vanderburg, M. Lopez-Morales, J. Perez-Mercader, T. R. Mattsson, G. Li, M. Z. Heising, A. S. Bonomo, M. Damasso, T. A. Berger, H. Cao, A. Levi, and R. D. Wordsworth, *Proc. Natl. Acad. Sci. U.S.A.* **116**, 9723 (2019).
- [55] G. Kresse and J. Hafner, *Phys. Rev. B* **47**, 558 (1993).
- [56] G. Kresse and J. Hafner, *Phys. Rev. B* **49**, 14251 (1994).

- [57] G. Kresse and J. Furthmüller, Phys. Rev. B **54**, 11169 (1996).
- [58] G. Kresse and J. Furthmüller, Comput. Mater. Science **6**, 15 (1996).
- [59] J. Hafner, J. Comput. Chem. **29**, 2044 (2008).
- [60] J. P. Perdew, K. Burke, and M. Ernzerhof, Phys. Rev. Lett. **77**, 3865 (1996).
- [61] O. Sugino and R. Car, Phys. Rev. Lett. **74**, 1823 (1995).
- [62] M. A. Morales, C. Pierleoni, E. Schwegler, and D. M. Ceperley, Proc. Natl. Acad. Sci. U.S.A. **107**, 12799 (2010).
- [63] S. Nosé, Prog. Theo. Phys. Supp. **103**, 1 (1991).
- [64] W. G. Hoover, Phys. Rev. A **31**, 1695 (1985).
- [65] F. Soubiran and B. Militzer, *10th International Conference on High Energy Density Laboratory Astrophysics*, High Energy Density Phys. **17**, 157 (2015).

SIMULATION METHODS

Our computational method is a combination of density functional theory (DFT) with molecular dynamics (MD) simulations, commonly referred to as DFT-MD. It is based on the Born-Oppenheimer approximation and allows us to calculate the electronic structure of the system with DFT, while the classical motion of the ions is calculated through MD simulations with forces derived self-consistently from the DFT.

DFT-MD simulations

All DFT-MD simulations were performed using the Vienna Ab-initio Simulation Package (VASP) [55–59]. The Perdew, Burke, and Ernzerhof (PBE) exchange-correlation functional [60] was used for all simulations. DFT-MD simulations allow the calculation of the thermodynamic variables p^{DFT-MD} , and u^{DFT-MD} straightforwardly when v , T , and x are defined as input quantities.

The electron-ion interaction was described with projector augmented wave (PAW) potentials for the hydrogen (PAW_PBE H.h 06Feb2004) and oxygen (PAW_PBE O.h 06Feb2004) atoms as implemented in VASP. We used a plane wave cutoff of 1100 eV and the Baldereschi mean value point to sample the Brillouin zone. We calculated 12 different H₂-H₂O concentrations using the following ratios of $N_{\text{H}_2}:N_{\text{H}_2\text{O}}$ molecules in our simulation boxes: 128:0, 128:3, 128:10, 128:18, 128:30, 108:36, 48:80, 64:64, 40:64, 21:64, 10:64, 0:64.

We used the Nosé-Hoover thermostat [63, 64] to control and maintain the system’s temperature in the NVT ensemble. Based on previous studies [34, 37, 65] and our own testing, a timestep length of 0.3 – 0.4 fs was determined to be appropriate for this system. The thermostat’s coupling time was set to a sufficiently high value of approximately $\tau_{\text{coupling}} \approx 200$ steps. We compared our results using these settings to a constant temperature calculation using velocity rescaling and found no significant differences.

Pressures and energies stayed correlated for a long time at the lowest p - T conditions. Therefore, very long simulation times up to 300 ps were necessary to obtain well-converged and sufficiently ergodic results. For higher temperatures and pressures the correlation times were significantly smaller and typical simulation times amounted to $10 < \tau < 15$ ps.

Coupling Constant Integration to calculate the entropy

Since the entropy of the mixture is not directly accessible with DFT-MD, we also use the coupling-constant-

integration (CCI) method [32], also known as thermodynamic integration. In this method, two different systems are coupled using an artificial coupling parameter λ . The difference in free energy ΔF between system 0 and system 1 can be calculated as follows:

$$\Delta F = F_1 - F_0 = \int_0^1 \langle V_1 - V_0 \rangle_\lambda d\lambda, \quad (6)$$

where ΔF is the difference in free energy, F_1 and F_0 are the free energies of system 0 and 1, respectively. V_0 and V_1 are the potential energies of systems 0 and 1. To apply the CCI method in practice, a reference system must be chosen for which the F_0 is exactly known (here the ideal gas, indexed with 0).

For technical reasons, we use the CCI method to compute the difference in free energy between the ideal gas and the fully interacting DFT-MD system by performing the simulation in two distinct steps [61]. First, the difference in free energy between the ideal gas system and a system interacting with reflected Yukawa potentials [62] is calculated using classical Monte-Carlo (MC) simulations. Secondly, the difference in free energy between the reflected Yukawa potentials and the fully interacting DFT-MD system is calculated using DFT-MD simulations. Thus, the total free energy is given by:

$$F(V, T, x) = F_{\text{id}} + \Delta F_{\text{id} \rightarrow \text{RY}} + \Delta F_{\text{RY} \rightarrow \text{DFT-MD}}. \quad (7)$$

Several authors have used this procedure to calculate immiscibility in mixtures of hydrogen and helium [33–35, 40].

The forces of the reflected Yukawa potential become more influential as the DFT forces with decreasing λ . Because the reflected Yukawa potential is fully repulsive, the water- and hydrogen molecules dissociate at certain λ values. At $\lambda = 0$, the system is fully dissociated, and the DFT forces do not contribute any more to the MD simulation. We always start with pure DFT-MD simulation ($\lambda = 1$). Simulations with lower λ are performed consecutively using equilibrated configurations from a simulation with higher λ . This procedure leads to continuous dissociation of molecules within the DFT-MD simulation.

Depending on the p - T conditions, we choose 6 to 11 λ points to do the CCI between the reflected Yukawa potentials and the fully interacting DFT-MD system as given by formula 6. Especially under the lowest temperature and pressure conditions, we need 11 λ points to converge our results sufficiently. To demonstrate the λ -point convergence, we varied the number of integration points for the different concentrations. The results are shown in Fig. 5, taking a temperature of $T = 1000$ K and a pressure of $p = 40$ kbar as example.

At higher temperature and pressure conditions, the CCI can be done with 6 λ points without loss of accuracy.

The classical MC simulations for the second branch of the integration are several orders of magnitude faster

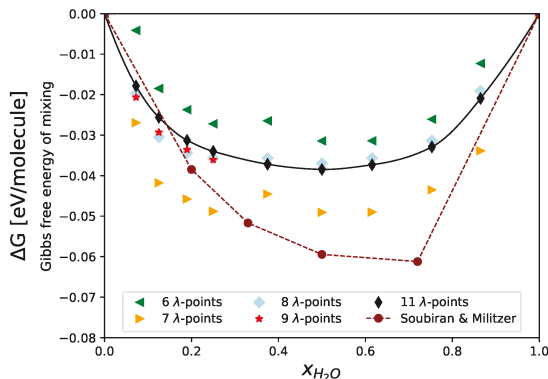


FIG. 5. Results of the CCI at a temperature of $T = 1000$ K and a pressure of $p = 40$ kbar using different sets of integration (λ) points. For pure hydrogen and water concentrations we did the integration always with the highest number of λ points, respectively. The purple diamonds have been calculated by only using 5 λ points for the CCI.

TABLE II. Coefficients for the reflected Yukawa pair potentials.

	a [eV·Å]	b [Å ⁻¹]	L [Å]
H - H	2.484	0.1	9
H - O	1.988	0.1	9
O - O	1.658	0.1	9

than the DFT-MD simulations. Therefore, we used 40 λ points to converge the integration between the non-interacting system (ideal gas) and the reflected Yukawa potentials.

The reflected Yukawa potential is defined as:

$$V_{RY}^{ij}(r_{ij}) = \begin{cases} a \left(\frac{e^{-br}}{r_{ij}} + \frac{e^{-b(L-r_{ij})}}{L-r_{ij}} - 4 \frac{e^{-bL/2}}{L} \right) & r_{ij} < L/2, \\ 0, & r_{ij} > L/2, \end{cases} \quad (8)$$

where a , b and L are coefficients given in Tab. II.

The potential parameters of the reflected Yukawa potential have to be chosen with caution. On the one hand, the potentials have to be sufficiently repulsive to dissociate the molecules while switching from the fully interacting DFT-MD system to the reflected Yukawa system. If the reflected Yukawa potentials are not repulsive enough, the molecules dissociate suddenly at $\lambda \ll 0.1$. Then, a very large amount of λ points would be necessary to fit the data to an Akima Spline and perform the CCI. Additionally, the atoms may come too close to each other, and the DFT-MD cycle would not converge anymore. However, if the reflected Yukawa potentials are too repulsive, the opposite problem might occur and the molecules dissociate rapidly at $\lambda \gg 0.9$.

Quantum Corrections

We take nuclear quantum effects into account by applying the correction formulas of Berens *et al.* [39] on our DFT-MD simulations. This post-processing method calculates a correction to the free energy F^{QC} corresponding to the difference between the quantum harmonic and the classical oscillator for each frequency interval in the power spectrum of the nuclear motion. The correction formula reads:

$$F^{QC} = \frac{3Nk_B T}{2\pi} \int_0^\infty d\omega \mathcal{S}(\omega, V, T, x) \left[W_F^Q(\omega) - W_F^C(\omega) \right], \quad (9)$$

where k_B is the Boltzmann constant, V is the volume, N is the total number of nuclei, ω is the frequency, and $\mathcal{S}(\omega, V, T, x)$ is the power spectrum of the nuclear motion, [34, 35, 39]. $W_F^{Q,C}$ are the weighting functions for the quantum and classical harmonic oscillator, respectively, and are given by:

$$W_F^Q(\omega) = \ln [1 - \exp(-\beta\hbar\omega)] + \frac{\beta\hbar\omega}{2} \quad (10)$$

and

$$W_F^C(\omega) = \ln(\beta\hbar\omega), \quad (11)$$

where $\beta = 1/k_B T$ and \hbar the Planck constant. The power spectrum of the nuclear motion is defined as: [38, 39]

$$\mathcal{S}(\omega, V, T, x) = \sum_a \frac{4N_a m_a}{3Nk_B T} \int_0^\infty dt \cos(\omega t) \langle \vec{v}_a(t) \cdot \vec{v}_a(0) \rangle, \quad (12)$$

N_a and m_a are number and mass of nuclear species a , respectively [38]. The volume-dependent spectrum $\mathcal{S}(\omega, V, T, x)$ introduces a volume dependence in $F^{QC}(V, T, x)$, which, in turn, leads to the following quantum correction for the pressure:

$$p^{QC}(V, T, x) = - \left(\frac{\partial F^{QC}}{\partial V} \right)_{T, x}. \quad (13)$$

Thus, the quantum correction to the free enthalpy is:

$$G^{QC}(V, T, x) = F^{QC}(V, T, x) + p^{QC}(V, T, x)V. \quad (14)$$

Finally, this relation needs to be inverted to have the pressure $p = p^{QC} + p^{DFT}$ as independent variable. A quadratic fit to $V(p^{DFT+QC}, T, x)$ was used to perform the inversion of $G(V, T, x)$ to $G(p^{DFT+QC}, T, x)$ each with three data points per T and x .

Comparison with results from Soubiran et al.

A comparison of our results and the results calculated by Soubiran and Militzer [31] is shown in Fig. 6. They

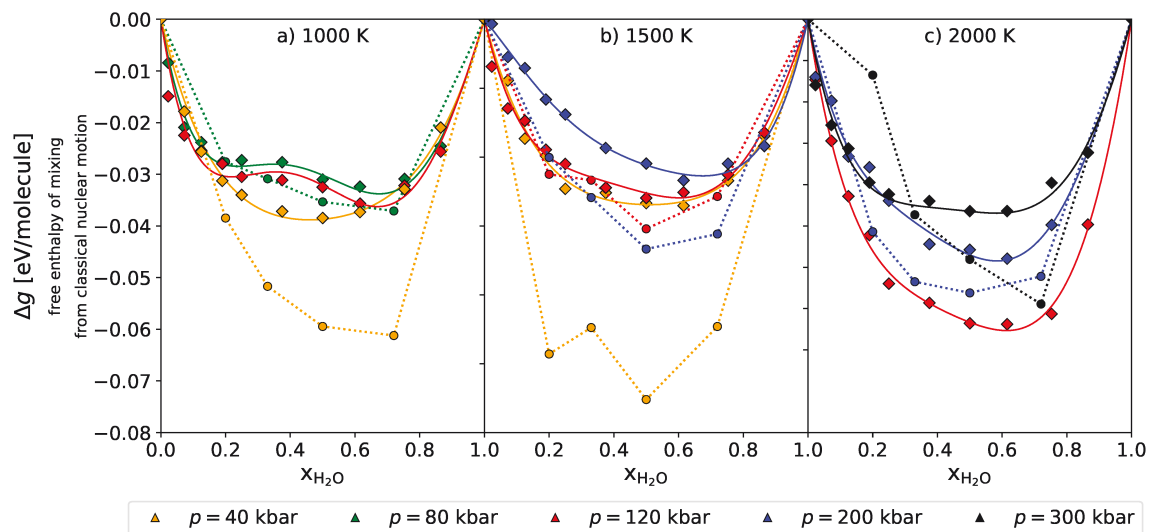


FIG. 6. Free enthalpy of mixing Δg for different p-T conditions. Panel a), b), and c) show ΔG for $T = 1000, 1500,$ and 2000 K, respectively. Our results are given by colored diamonds and the results of Soubiran and Militzer are given by colored circles.

calculated 6 different hydrogen and water concentrations using the following $N_{\text{H}_2}:N_{\text{H}_2\text{O}}$ ratios: 92:0, 64:16, 48:24, 32:32, 16:40, 0:48. Their DFT-MD simulations were performed for 0.5 ps up to 7 ps. Soubiran and Militzer used time step of $\tau = 0.2$ fs. To conduct the CCI between the fully interacting DFT-MD system and the classical system, 5 to 7 λ integration points were used.

Especially, for the lowest calculated pressure of 40 kbar, we found significant deviations. The Nosé-Hoover thermostat [63, 64] introduces a large bias for pure hydrogen if one chooses the standard coupling fre-


quency as predefined by the used simulation code VASP. This issue, however, causes Δg to shift to lower values. Adopting the parameters of Soubiran and Militzer [31], i.e. a time step of $\tau = 0.2$ fs and a coupling time of 40 fs for the thermostat in test simulations, we were able to reproduce their free enthalpies within statistical fluctuations. Finally, because of our longer simulation times, more λ integration points, twice as many water concentrations, and higher particle numbers we were able to reduce the statistical uncertainties significantly which has led to our prediction for a demixing region in the $\text{H}_2\text{-H}_2\text{O}$ system.

6.4. Nonmetal-to-metal transition in dense fluid nitrogen at high pressure

Author contributions:

- **A. Bergemann:** Preparation of the manuscript, DFT-MD simulations and conductivity calculations, interpretation of the results
- **R. Redmer:** Supervision of the project, preparation of the manuscript, DFT-MD simulations, interpretation of the results

Nonmetal-to-metal transition in dense fluid nitrogen at high pressure

Armin Bergermann and Ronald Redmer *Institut für Physik, Universität Rostock, D-18051 Rostock, Germany*

(Received 2 May 2023; revised 17 July 2023; accepted 19 July 2023; published 1 August 2023)

We calculate the electrical conductivity and the equation of state of dense fluid nitrogen for high pressures up to several megabars by using *ab initio* molecular dynamics simulations. We determine the instability region of a first-order liquid-liquid phase transition which results from an abrupt dissociation of nitrogen molecules. This transition is accompanied by a nonmetal-to-metal transition (metallization) of the fluid and corresponding structural changes from a molecular to a polymeric phase. We compare our new data with earlier theoretical results and available experiments.

DOI: [10.1103/PhysRevB.108.085101](https://doi.org/10.1103/PhysRevB.108.085101)

I. INTRODUCTION

The high-pressure phase diagram of *solid* nitrogen is extremely rich: 12 molecular phases, two nonmolecular phases, and an amorphous one have been reported so far [1]. Nitrogen molecules consist of two atoms strongly triple bonded so that corresponding phases can be considered inert. If exposed to high pressure, however, intramolecular bonding becomes weaker, so that double and single bonds also appear. Accordingly, the structural and electronic properties change so that nitrogen passes through several intermediate phases with increasing pressure before covalency is completely lost [2].

Recent molecular dynamics (MD) simulations on dense *fluid* nitrogen using density functional theory (DFT) [3–7] [8,9] predict a first-order liquid-liquid phase transition (LL-PT) at about a megabar. The crossover from a molecular to a polymeric phase is driven by an electronic transition from a molecular semiconducting fluid to a polymeric one with metalliclike conductivity, which has been observed in multiple shock-wave experiments [10].

Excitation, dissociation, and ionization processes are also observed in other shock-compressed diatomic fluids, such as O₂ and CO (which is isoelectronic with N₂); for a review, see Refs. [2,11]. Most interesting is the metallization in hydrogen (or deuterium) at few megabars [12–15], which, e.g., governs the interior structure, thermal evolution, and dynamo action (magnetic-field generation) of gas giant planets, such as Jupiter and Saturn [16].

In the polymeric phase, each nitrogen atom has single chemical bonds with three surrounding atoms so that this phase could store several times more energy than any known material [2]. This would make polymeric nitrogen an exciting high-energy-density material for corresponding applications.

Numerous high-pressure experiments were performed using diamond anvil cells (DACs) to reveal the high-pressure phase diagram of solid nitrogen and the properties of the different phases; see, e.g., Refs. [2,17,18]. Higher temperatures are generated in shock-wave compression experiments so that dense fluid nitrogen can be probed; see, e.g., Refs. [10, 19–24]. The interesting effect of *shock cooling* due to the dissociation of nitrogen molecules along shock compression

has been predicted by Radousky *et al.* [21] in 1985. The corresponding *P-T* conditions are relevant for the interior of ice giant planets, such as Uranus and Neptune. The equation of state (EOS) data in this range are, thus, important for modeling the interior, evolution, and magnetic field of ice giant planets; see, e.g., Refs. [25–32].

Given these important applications, we have reassessed the behavior of dense fluid nitrogen and performed extensive DFT-MD simulations to determine the EOS for temperatures in the range of 2000 K $\leq T \leq$ 10 000 K and densities of 1.1 g/cm³ $\leq \rho \leq$ 4.0 g/cm³. Analysis of our EOS data shows a systematic shift to higher pressures for given temperatures and densities compared with some earlier studies [3,5]. This trend can be traced back to the use of a higher particle number (256 nitrogen atoms with five electrons each in our calculations versus 64 in Refs. [3,5]), enabled by the enormous progress in computational power over the past decade. The differences are pronounced in the dissociation region so that a new prediction for the instability region of the first-order LL-PT can be given.

We have determined the pair distribution function (PDF) and the coordination number so that the structural changes along the transition can be analyzed as function of density and temperature.

Furthermore, the electrical conductivity was calculated for the entire density-temperature range mentioned above in order to locate the nonmetal-to-metal transition in the *P-T- ρ* space. The electrical conductivity increases over about seven orders of magnitude from an almost insulating behavior at the lowest densities and temperatures to values typical for metals at higher densities and temperatures. In these DFT calculations, we have applied the Heyd-Scuseria-Ernzerhof (HSE) hybrid functional [33–36] to determine realistic band gaps, which is essential along the metallization transition. Our results give new insight into the nature of this combined thermodynamic (liquid-liquid, first order) and electronic (metallization) transition in dense fluid nitrogen.

The outline of our paper is as follows. First, we summarize details of the DFT-MD simulations for dense fluid nitrogen in Sec. II. Results for the EOS data are shown in Sec. III, and the structural changes along compression are discussed in Sec. IV

using the pair distribution function. An update of the high-pressure phase diagram is shown in Sec. V. The calculation of the electrical conductivity via the Kubo-Greenwood formula [37,38] is outlined in Sec. VI where we also discuss the nonmetal-to-metal transition in dense fluid nitrogen. Finally, we summarize our results in Sec. VII.

II. DFT-MD SIMULATIONS

The DFT-MD simulations were performed using the Vienna *Ab initio* simulation package (VASP) [39–43]. The Born-Oppenheimer approximation is used to describe the electron system with DFT at finite temperatures [44–48] and to treat the ions classically via MD simulations. The projector-augmented wave (PAW) potential as implemented in VASP, PAW_PBE N_h 06Feb2004, (where PBE represents Perdew, Burke, and Ernzerhof) was used. We used a plane-wave cutoff of 1000 eV, which is considerably higher as in earlier studies. All simulations are performed within the NVT ensemble by using the Nosé-Hoover thermostat [49,50].

We made extensive convergence tests with respect to particle number and chose $N = 256$ for all DFT-MD simulations for temperatures in the range of $2000 \text{ K} \leq T \leq 5000 \text{ K}$ and densities of $2.4 \text{ g/cm}^3 \leq \rho \leq 4.0 \text{ g/cm}^3$. The first-order LL-PT occurs in this temperature-density range. We found characteristic fluctuations close to the instability region so that large enough particle numbers had to be used. For conditions further away from the LL-PT, our simulations are already converged with $N = 64$. The MD simulations were performed with up to 100 000 time steps of 0.6 fs duration, i.e., the chosen NVT ensemble ran up to 60 ps.

We used the exchange-correlation (XC) functional of PBE [51] for all MD runs. Additionally, we employed the HSE hybrid functional [33–36] to evaluate the Kubo-Greenwood formula. The calculation of the electrical conductivity along the nonmetal-to-metal transition required the use of a hybrid functional, such as HSE, which reproduces band gaps and, in particular, their closing with increasing pressure more realistically than PBE; see, e.g., Refs. [52–54].

III. RESULTS FOR THE EOS

We present the thermal EOS, i.e., the pressure as a function of the density for given temperatures as derived from our DFT-MD simulations in Fig. 1. For clarity, isotherms between $2000 \text{ K} \leq T \leq 4000 \text{ K}$ are shown in the upper panel, and those between $4000 \text{ K} \leq T \leq 10000 \text{ K}$ in the lower panel, respectively. In accordance with Boates and Bonev [3] and Driver and Militzer [5], we observe an instability region in the dense fluid for lower temperatures, which is highlighted in the inset in the upper panel; see Sec. V.

Our pressures are systematically higher by 10–20% than those of Boates and Bonev [3], which can be attributed to the use of higher particle numbers in our simulations: 256 nitrogen atoms (with five electrons each) compared with 64–128 atoms in their calculations. The higher particle number was necessary to get converged results, particularly, near the dissociation transition. Boates and Bonev [3] used the Γ point, whereas, we used the Baldereschi mean value point (BMVP) [55] to sample the Brillouin zone. Note that Boates

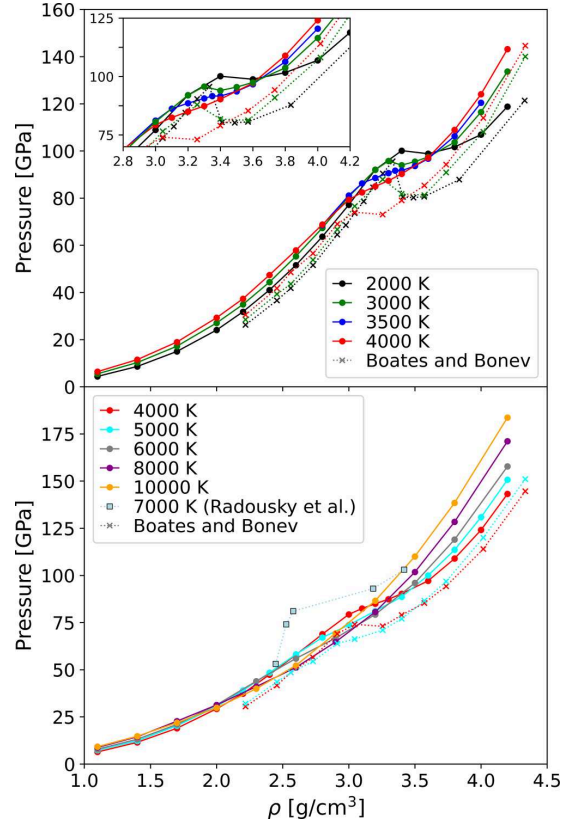


FIG. 1. The pressure of nitrogen is shown as a function of density for temperatures between 2000 and 4000 K (upper panel) and 4000 and 10 000 K (lower panel). We compare our DFT-MD results (solid colored lines with dots) with those of Boates and Bonev [3] (dotted lines with crosses, same color code). Pressures derived from double-shock experiments of Radousky *et al.* [21] are shown as light blue boxes in the lower panel for which a temperature of $T \approx 7000 \text{ K}$ was reported.

and Bonev [3] predict the stability region above 4000–5000 K, whereas, we derive a critical temperature of $T_c = 3500 \text{ K}$, see Sec. V.

In 1985, Radousky *et al.* [21] dynamically compressed fluid nitrogen by using a gas gun. In single-shock experiments, i.e., along the Hugoniot curve, they measured temperatures between $4000 \text{ K} < T < 14000 \text{ K}$ and pressures in the range of $18 \text{ GPa} < P < 90 \text{ GPa}$. By performing double-shock experiments, they reported pressures between $60 \text{ GPa} < P < 90 \text{ GPa}$ at an almost constant temperature of about $T \approx 7000 \text{ K}$. The results of these double-shock experiments shown in the lower panel of Fig. 1 as light blue boxes are substantially higher than our results for all temperatures between 4000 and 10000 K in the density range between 2.4 and 3.2 g/cm^3 . Radousky *et al.* [21] inferred the temperature by measuring the spectral radiance of the light emitted from the shocked sample. The vast differences between our *ab initio* results and

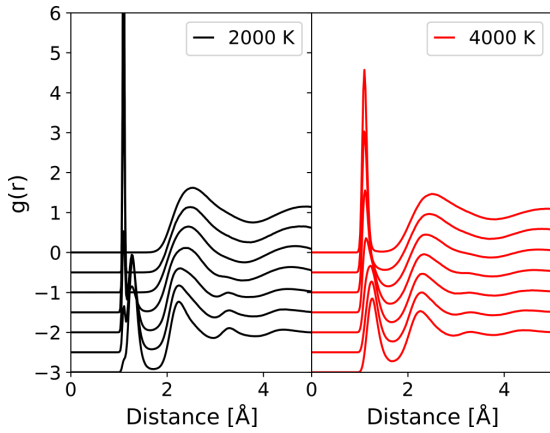


FIG. 2. Pair distribution function in fluid nitrogen for densities of $\rho = 2.8, 3.0, 3.2, 3.4, 3.6, 3.8,$ and 4.0 g/cm^3 . The lines are shifted downwards by -0.5 with increasing density. Left panel (black): $T = 2000 \text{ K}$, right panel (red): $T = 4000 \text{ K}$.

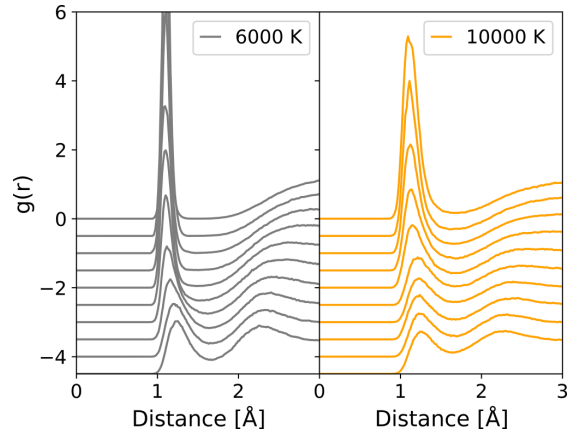


FIG. 3. Pair distribution function in fluid nitrogen for densities of $\rho = 2.8, 3.0, 3.2, 3.4, 3.6, 3.8,$ and 4.0 g/cm^3 . The lines are shifted downwards by -0.5 with increasing density. Left panel (gray): $T = 6000 \text{ K}$, right panel (orange): $T = 10000 \text{ K}$.

their P - T data in that density range should be resolved by new shock-compression experiments.

At higher temperatures, the dissociation of nitrogen molecules leads to a reversal of the order of the pressure isotherms above 1.5 g/cm^3 , see lower panel of Fig. 1. The isotherms return to the usual temperature order only above 3.5 g/cm^3 in this higher temperature regime. It is interesting to note that the crossing of the isotherms occurs in a much narrower density region for the lower temperatures (upper panel of Fig. 1), i.e., between 2.7 and 3.7 g/cm^3 . The different isotherms clearly show the interplay of thermally and pressure-driven dissociation in dense fluid nitrogen. For higher temperatures, thermally driven dissociation dominates but does not lead to an instability region. In comparison, dissociation occurs more abruptly for lower temperatures, leading to a first-order LL-PT, such as in hydrogen [14,15].

IV. RESULTS FOR THE PAIR DISTRIBUTION FUNCTIONS

The PDFs are shown in Figs. 2 and 3, whereas, the coordination number is displayed in Fig. 4. These results can be used to study the structural changes in the fluid as a function of temperature T and density ρ .

Figure 2 shows the PDF for 2000 K (left panel) and 4000 K (right panel) for various densities. For 2000 K , a pronounced molecular peak appears at 1.1 \AA at lower densities. For densities $\rho > 3.4 \text{ g/cm}^3$ a second peak at 1.3 \AA appears, which can be attributed to the transition from a molecular to a polymeric phase, accompanied by a first-order LL-PT. Several authors have already described this behavior [3–7]. At the higher temperature of 4000 K , a shift of the first peak of the PDF from 1.1 to 1.3 \AA is observed, which proceeds continuously. This shift indicates that the CP of the first-order LL-PT is located below 4000 K , in accordance with the EOS data, see Sec. V. In Fig. 3, the PDF is shown for higher temperatures of 6000 K (left panel) and 10000 K (right panel). Interestingly, the molecular peak at 1.3 \AA is still visible even at these

high temperatures, which indicates that nitrogen transforms gradually to an atomic liquid with increasing density as discussed above.

By integrating the PDF in spherical coordinates up to the first minimum, according to

$$n(r') = 4\pi\rho \int_0^{r'} g(r)r^2 dr, \quad (1)$$

the coordination number is obtained. This quantity indicates how many molecules are found in the range of each coordination sphere by integrating from 0 to the first minimum r' in the PDF. Therefore, the coordination number signals structural changes in the dense fluid upon compression.

For 2000 K , the coordination number is just 1 for densities $\rho < 3.2 \text{ g/cm}^3$ describing a molecular fluid composed of triple bonded N_2 molecules. For higher densities, a rapid increase in the coordination number up to 2 and above occurs,

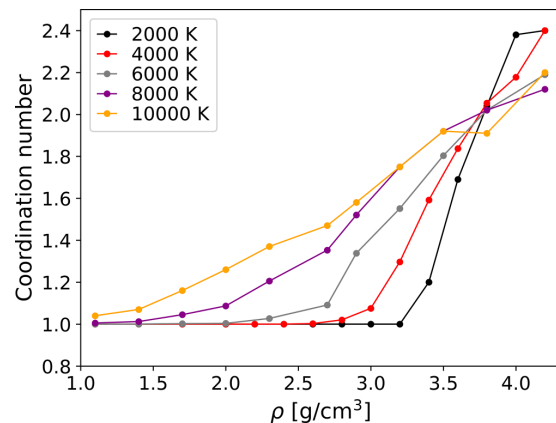


FIG. 4. Coordination number according to Eq. (1) as function of the density for several temperatures: $T = 2000, 4000, 6000, 8000,$ and 10000 K .

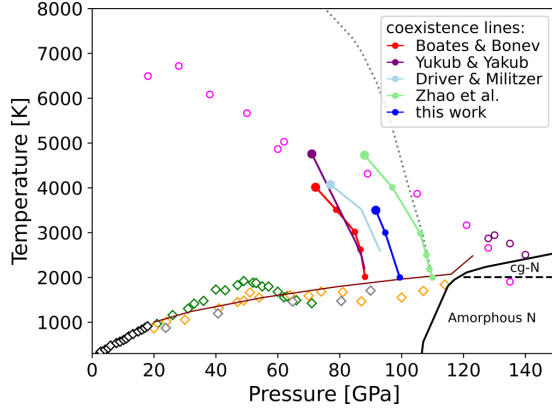


FIG. 5. Phase diagram of nitrogen according to Boates and Bonev [3]. Melting line (diamonds: black [57], green [58], orange [59], gray [60]), polymeric solid phases labeled amorphous and cubic gauche (cg-N). The dark-red line represents experimental data for the melting line of Weck *et al.* [61]. Our prediction for the LL-PT (blue line) is compared with that of Boates and Bonev [3] (red line), Yakub and Yakub [56] (purple line), Driver and Militzer [5] (light blue line), and Zhao *et al.* [9] (light green line). Magenta (violet) circles indicate the onset of absorption (reflection) observed in laser-heated DAC experiments [6]. The dotted line represents the phase boundary as predicted by the chemical model of Ross and Rogers [62].

which indicates the transition to the polymeric regime. As seen in the PDF, nitrogen stays molecular even for high temperatures. The increase in the coordination number becomes more gradual with increasing temperature in accordance with the EOS results.

V. HIGH-PRESSURE PHASE DIAGRAM

The thermodynamic stability condition $(\partial P/\partial \rho)_T \geq 0$ is violated below 3500 K so that a van der Waals loop occurs, which has to be treated by a Maxwell construction. Our numerical results indicate that the critical point for the corresponding LL-PT is located at about $T_c = 3500$ K, $\rho_c = 3.4$ g/cm³, and $P_c = 90$ GPa, i.e., the critical temperature is lower than earlier predicted. The coexistence line of the first-order LL-PT is shown as a blue line in Fig. 5, the high-pressure phase diagram adapted from Boates and Bonev [3] with experimental data for the melting line and polymeric solid phases (amorphous and cubic gauche).

According to the EOS data shown in Fig. 1, the coexistence line of the LL-PT is shifted by about 10 GPa towards higher pressures compared with their curve (red line). Yakub and Yakub [56] used the *ab initio* calculations of Boates and Bonev [3] to calibrate an advanced polymerization model. Their prediction for the coexistence line of the LL-PT is shown for comparison (purple line). The prediction of Driver and Militzer [5] for the coexistence line (light blue line) is also based on DFT-MD simulations and located between our result and that of Boates and Bonev [3]. Driver and Militzer [5] have performed their DFT-MD simulations with 64 atoms as Boates and Bonev [3]. The prediction of Zhao *et al.* [9] (green line) is based on DFT-MD simulations using the strongly constrained

TABLE I. Input used in DFT-MD simulations for dense fluid nitrogen. Compared are the XC functional, the number of atoms N , and the point set for the evaluation of the Brillouin zone (BZ).

Ref.	XC functional	N (atoms)	BZ sampling
Boates and Bonev [3]	PBE	64–128	Γ
Driver and Militzer [5]	PBE	64	Γ
Zhao <i>et al.</i> [9]	SCAN	64	Γ
Fu <i>et al.</i> [7]	PBE	54	Γ
Mazevet <i>et al.</i> [63]	PW91	32	Γ
Present paper	PBE and HSE	64–256	BMVP

and appropriately normed (SCAN) meta-generalized gradient approximation functional with 64 atoms. Their LL-PT line lies about 10% above our results in P - T space. All earlier studies employed the Gamma (Γ) point to evaluate the Brillouin zone, whereas, we used the BMVP. We summarize the main input into different DFT-MD simulations performed for dense fluid nitrogen in Table I.

Drastic changes in the optical properties of dense fluid nitrogen upon compression were observed in laser-heated DAC experiments. Jiang *et al.* [6] find an onset of absorption (magenta points in Fig. 5) that agrees qualitatively with the continuous transition between the molecular and dissociated fluid above the critical point. The onset of reflection (violet points) indicates the transition to a metallic state at pressures well above a megabar. This transition can be explained by means of the electrical conductivity, which is discussed in the next section.

We also show the prediction of the dissociation model of Ross and Rogers [62] for the molecular-to-polymeric phase transition in the dense fluid (dotted line). They used the experimental data of Refs. [19,21] and calculated the Grüneisen parameter. The corresponding transition pressure is higher than the results of some of the DFT-MD simulations [3,5] including ours but agrees with the SCAN results [9]. The LL-PT line has a different slope for higher temperatures. This behavior is similar to that of the EOS data of Radousky *et al.* [21] shown in the lower panel of Fig. 1. Note that predictions of chemical models have to be treated with caution in the warm dense matter region. The key quantity, the shift in the dissociation energy with density and temperature, is usually treated within simple models which neglect, e.g., effects of disorder (ion structure) and the formation of electronic bands, which are important in this dense fluid regime.

VI. ELECTRICAL CONDUCTIVITY

The dynamic conductivity $\sigma(\omega)$ is derived from the Kubo-Greenwood formula, [37,38,64–66],

$$\sigma(\omega) = \frac{2\pi e^2}{3\omega\Omega} \sum_{\mathbf{k}} W(\mathbf{k}) \sum_{j=1}^N \sum_{i=1}^N \sum_{\alpha=1}^3 [F(\epsilon_{i,\mathbf{k}}) - F(\epsilon_{j,\mathbf{k}})] \times |\langle \Psi_{j,\mathbf{k}} | \vec{v} | \Psi_{i,\mathbf{k}} \rangle|^2 \delta(\epsilon_{j,\mathbf{k}} - \epsilon_{i,\mathbf{k}} - \hbar\omega), \quad (2)$$

where e is the electron charge, m is its mass, ω is the frequency, and Ω is the volume of the simulation box. $\epsilon_{i,k}$ and $F(\epsilon_{i,k})$ are the energy eigenvalue and Fermi occupation number of the Bloch state $|\Psi_{i,k}\rangle$ calculated from DFT, and $\langle\Psi_{j,k}|\vec{v}|\Psi_{i,k}\rangle$ are matrix elements with the velocity operator calculated with the optical routines of VASP [39–43]. The discrete spectrum of eigenvalues is caused by the periodic boundary conditions of the simulation box, so the δ function has to be broadened to a finite width for which we use a Gaussian function. Summation over the Brillouin zone is performed by using special k point sets with weighting factors $W(\mathbf{k})$; for details, see Refs. [66–69].

For temperatures $T \leq 4000$ K, we evaluated the Kubo-Greenwood formula (2) for 100 snapshots of the MD simulation selected at constant time intervals and used the BMVP to evaluate the Brillouin zone. Performing the simulations with 256 nitrogen atoms, we found the BMVP sufficient to sample the Brillouin zone with the required accuracy. A comparison with Monkhorst-Pack (MP) $2 \times 2 \times 2$ or $3 \times 3 \times 3$ point sets revealed no significant differences for our conductivity calculations. This convergence enabled us to calculate the electrical conductivity using the hybrid functional HSE [33–36], which is computationally much more demanding than the PBE XC functional. For higher temperatures $T > 4000$ K, we used 64 atoms and calculated the conductivity by averaging 20 snapshots. To converge the electrical conductivity at these conditions, we calculated the snapshots with MP 3^3 point sets. We used the PBE XC functional for those higher temperatures since the electrical conductivity already has metalliclike values in this range due to the nonmetal-to-metal transition.

The results for the static electrical conductivity are shown in Fig. 6 and compared with those of Boates and Bonev [4]. The calculated densities are the same as given in the EOS, see Fig. 1. In the pressure region between 75 and 100 GPa, we find a substantial increase in the conductivity over several orders of magnitude from values typical for semiconductors up to metal-like conductivities. Below the critical temperature of $T_c = 3500$ K, the conductivity jumps as a function of pressure from the value of the semiconducting fluid at the low-density branch of the coexistence curve to metal-like values at the high-density branch, which is typical for a first-order phase transition.

Furthermore, we find a strong influence of the XC functional on the conductivity values in the semiconducting fluid. It is well known that the hybrid HSE functional yields more realistic band gaps than PBE [52–54]. The corresponding conductivities are lower by one to two orders of magnitude, dependent on temperature. However, this difference becomes negligible for higher temperatures $T \geq 6000$ K so that we determined the conductivity solely with PBE in this range. In general, we find a good agreement of our PBE conductivities with those of Boates and Bonev [4].

In 2003, Mazevet *et al.* [63] performed DFT-MD simulations for fluid nitrogen and calculated the conductivity along the Hugoniot curve as well as for the 5000-K isotherm; the latter is shown as cyan diamonds in Fig. 6. They used 32 nitrogen atoms in the simulation cell, the Vanderbilt ultrasoft pseudopotential schema [70], and the Perdew-Wang 91 (PW91)

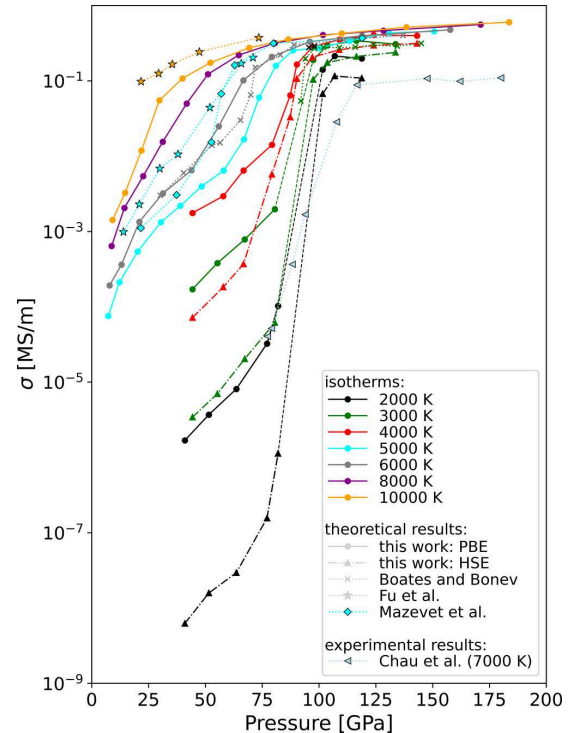


FIG. 6. Static electrical conductivity of dense fluid nitrogen as function of pressure for various temperatures (color coded). PBE functional (this paper): squares, HSE functional (this paper): triangles up. Earlier results based on DFT-MD methods: Boates and Bonev [4]: crosses, Fu *et al.* [7]: stars, and Mazevet *et al.* [63]: diamonds. Experimental data of Chau *et al.* [10] are shown by light-blue triangles left.

parametrization of the generalized gradient approximation [71]. Although we have used more nitrogen atoms in our simulations ($N = 256$) and a different exchange-correlation functional (PBE), we find reasonable agreement. In 2019, Fu *et al.* [7] evaluated the Kubo-Greenwood formula using DFT-MD simulations. They used the PBE functional, the Γ point to sample the Brillouin zone, and 54 nitrogen atoms in the simulation cell. Both studies yield higher conductivities compared to our findings. These deviations can be attributed to higher particle numbers in our simulations and different XC functionals; see Table I.

We also show the conductivities reported by Chau *et al.* [10] derived from double shock-wave experiments using a gas gun in Fig. 6. These data show qualitatively a continuous transition from a semiconducting fluid at lower pressures to a conducting fluid at high pressures, as predicted by the DFT-MD simulations for super critical temperatures $T \geq T_c$. Compared to our results, the transition pressure of Chau *et al.* [10] shifts towards higher pressures of $P \approx 100$ GPa. Furthermore, they assign a temperature of 7000 K to their entire curve, which does not fit at all in the temperature systematics of the DFT-MD simulations. Note that strong doubts have been raised that the treatment of dissociation in the evaluation

of Chau *et al.* is adequate for the dense fluid regime so that their estimate for the dissociation fraction and, consequently, the temperature might be inaccurate [72].

VII. CONCLUSIONS

We have calculated the EOS data, the structural properties, and the electrical conductivity of dense fluid nitrogen for a wide range of densities and temperatures by using extensive DFT-MD simulations. The enormous increase in computational power enabled us to use significantly higher particle numbers and more advanced XC functionals. We find a first-order LL-PT and locate the corresponding critical point at about $T_c = 3500$ K, $\rho_c = 3.4$ g/cm³, and $P_c = 90$ GPa. The electrical conductivity was derived from the Kubo-Greenwood formula using the hybrid HSE functional for temperatures $T \lesssim 4000$ K and the PBE functional for higher temperatures. We observe a nonmetal-to-metal transition in the dissociation region with jumps for the electrical conductivity in the instability region as characteristic of a first-order phase transition. The substantially increased computational cost using the hybrid HSE functional pays off since we could determine the electrical conductivity in the semi-conducting molecular fluid at lower temperatures reliably for the first time. The corresponding HSE values are one to two orders of magnitude lower than the predictions of the PBE functional.

Note that the nonmetal-to-metal transition, as observed in dense fluid nitrogen, is very similar to the behavior of

dense fluid hydrogen; see, e.g., Refs. [73,74]. Abrupt dissociation of molecules leads to a first-order LL-PT at lower temperatures. In comparison, the nonmetal-to-metal transition is more gradual at higher temperatures due to additional thermal excitations. The minimum metallic conductivity of $\sigma_{\min} \approx 2 \times 10^4$ S/m as proposed by Mott [75] originally for liquid mercury and later applied to other materials [76], is exceeded just in the transition region, see Fig. 6.

Our results will promote new experimental campaigns using DACs and/or shock waves to benchmark our predictions for the EOS data and the location of the first-order LL-PT in dense fluid nitrogen. In particular, such experiments will also be performed using DACs and ultrashort and intense x-ray beams provided by free electron laser (FEL) facilities, such as the Linear Coherent Light Source at SLAC Stanford or the European XFEL; see, e.g., Refs. [77,78]. The results presented in this paper underline the importance of new experiments to understand better the behavior of warm dense matter, in general, and of dense fluid nitrogen, in particular.

ACKNOWLEDGMENTS

We thank M. Preising, M. French, and A. Roy for many helpful discussions and technical support. This work was supported by the North German Supercomputing Alliance (HLRN) and the ITMZ of the University of Rostock as well as by the Deutsche Forschungsgemeinschaft (DFG) via the Research Unit FOR 2440. A.B. thanks the Evangelische Studienwerk e.V. for support.

-
- [1] R. Turnbull, M. Hanfland, J. Binns, M. Martinez-Canales, M. Frost, M. Marques, R. T. Howie, and E. Gregoryanz, Unusually complex phase of dense nitrogen at extreme conditions, *Nat. Commun.* **9**, 4717 (2018).
 - [2] L. N. Yakub, Polymerization in highly compressed nitrogen (review article), *Low Temp. Phys.* **42**, 1 (2016).
 - [3] B. Boates and S. A. Bonev, First-Order Liquid-Liquid Phase Transition in Compressed Nitrogen, *Phys. Rev. Lett.* **102**, 015701 (2009).
 - [4] B. Boates and S. A. Bonev, Electronic and structural properties of dense liquid and amorphous nitrogen, *Phys. Rev. B* **83**, 174114 (2011).
 - [5] K. P. Driver and B. Militzer, First-principles equation of state calculations of warm dense nitrogen, *Phys. Rev. B* **93**, 064101 (2016).
 - [6] S. Jiang, N. Holtgrewe, S. S. Lobanov, F. Su, M. F. Mahmood, R. S. McWilliams, and A. F. Goncharov, Metallization and molecular dissociation of dense fluid hydrogen, *Nat. Commun.* **9**, 2624 (2018).
 - [7] Z. Fu, Q. Chen, Z. Li, J. Tang, W. Zhang, W. Quan, J. Li, J. Zheng, and Y. Gu, Ab initio study of the structures and transport properties of warm dense nitrogen, *High Energy Density Phys.* **31**, 52 (2019).
 - [8] Y.-S. Lan, Z.-Q. Wang, L. Liu, G.-J. Li, H.-Y. Sun, Z.-J. Fu, Y.-J. Gu, G. Yang, L.-N. Li, Z.-G. Li, Q.-F. Chen, and X.-R. Chen, First-order liquid-liquid phase transition in nitrogen-oxygen mixtures, *Phys. Rev. B* **103**, 144105 (2021).
 - [9] G. Zhao, H. Wang, M. C. Ding, X. G. Zhao, H. Y. Wang, and J. L. Yan, Stability line of liquid molecular nitrogen based on the SCAN meta-GGA density functional, *Phys. Rev. B* **98**, 184205 (2018).
 - [10] R. Chau, A. C. Mitchell, R. W. Minich, and W. J. Nellis, Metallization of Fluid Nitrogen and the Mott Transition in Highly Compressed Low-Z Fluids, *Phys. Rev. Lett.* **90**, 245501 (2003).
 - [11] W. J. Nellis, Dynamic compression of materials: Metallization of fluid hydrogen at high pressures, *Rep. Prog. Phys.* **69**, 1479 (2006).
 - [12] E. Wigner and H. B. Huntington, On the possibility of a metallic modification of hydrogen, *J. Chem. Phys.* **3**, 764 (1935).
 - [13] S. T. Weir, A. C. Mitchell, and W. J. Nellis, Metallization of Fluid Molecular Hydrogen at 140 GPa (1.4 Mbar), *Phys. Rev. Lett.* **76**, 1860 (1996).
 - [14] M. D. Knudson, M. P. Desjarlais, A. Becker, R. W. Lemke, K. R. Cochrane, M. E. Savage, D. E. Bliss, T. R. Mattsson, and R. Redmer, Direct observation of an abrupt insulator-to-metal transition in dense liquid hydrogen, *Science* **348**, 1455 (2015).
 - [15] P. M. Celliers, M. Millot, S. Brygoo, R. S. McWilliams, D. E. Fratanduono, J. R. Rygg, A. F. Goncharov, P. Loubeyre, J. H. Eggert, J. L. Peterson, N. B. Meezan, S. Le Pape, G. W. Collins, R. Jeanloz, and R. J. Hemley, Insulator-metal transition in dense fluid deuterium, *Science* **361**, 677 (2018).
 - [16] R. Helled, G. Mazzola, and R. Redmer, Understanding dense hydrogen at planetary conditions, *Nat. Rev. Phys.* **2**, 562 (2020).

- [17] M. I. Eremets, A. G. Gavriluk, I. A. Trojan, D. A. Dzivenko, and R. Boehler, Single-bonded cubic form of nitrogen, *Nature Mater.* **3**, 558 (2004).
- [18] P. Cheng, X. Yang, X. Zhang, Y. Wang, S. Jiang, and A. F. Goncharov, Polymorphism of polymeric nitrogen at high pressures, *J. Chem. Phys.* **152**, 244502 (2020).
- [19] W. J. Nellis, H. B. Radousky, C. Hamilton, A. C. Mitchell, N. C. Holmes, K. B. Christianson, and M. van Thiel, Equation-of-state, shock-temperature, and electrical-conductivity data of dense fluid nitrogen in the region of the-dissociative phase transition, *J. Chem. Phys.* **94**, 2244 (1991).
- [20] Y.-J. Kim, B. Militzer, B. Boates, S. Bonev, P. M. Celliers, G. W. Collins, K. P. Driver, D. E. Fratanduono, S. Hamel, R. Jeanloz, J. R. Rygg, D. C. Swift, J. H. Eggert, and M. Millot, Evidence for Dissociation and Ionization in Shock Compressed Nitrogen to 800 GPa, *Phys. Rev. Lett.* **129**, 015701 (2022).
- [21] H. B. Radousky, W. J. Nellis, M. Ross, D. C. Hamilton, and A. C. Mitchell, Molecular Dissociation and Shock-Induced Cooling in Fluid Nitrogen at High Densities and Temperatures, *Phys. Rev. Lett.* **57**, 2419 (1986).
- [22] M. A. Mochalov, M. V. Zhernokletov, R. I. Il'kaev, A. L. Mikhailov, V. E. Fortov, V. K. Gryaznov, I. L. Iosilevskiy, A. B. Mezhevov, A. E. Kovalev, S. I. Kirshanov, Y. A. Grigor'eva, M. G. Novikov, and A. Shuikin, Measurement of density, temperature, and electrical conductivity of a shock-compressed nonideal nitrogen plasma in the megabar pressure range, *J. Exp. Theo. Phys.* **110**, 67 (2010).
- [23] G. L. Schott, M. S. Shaw, and J. D. Johnson, Shocked states from initially liquid oxygen-nitrogen systems, *J. Chem. Phys.* **82**, 4264 (1985).
- [24] W. J. Nellis and A. C. Mitchell, Shock compression of liquid argon, nitrogen, and oxygen to 90 GPa (900 kbar), *J. Chem. Phys.* **73**, 6137 (1980).
- [25] S. Stanley and J. Bloxham, Convective-region geometry as the cause of Uranus' and Neptune's unusual magnetic fields, *Nature (London)* **428**, 151 (2004).
- [26] S. Stanley and J. Bloxham, Numerical dynamo models of Uranus' and Neptune's magnetic fields, *Icarus* **184**, 556 (2006).
- [27] R. Redmer, T. R. Mattsson, N. Nettelmann, and M. French, The phase diagram of water and the magnetic fields of Uranus and Neptune, *Icarus* **211**, 798 (2011).
- [28] N. Nettelmann, R. Helled, J. Fortney, and R. Redmer, New indication for a dichotomy in the interior structure of Uranus and Neptune from the application of modified shape and rotation data, *Planet. Space Sci.* **77**, 143 (2013).
- [29] L. Scheibe, N. Nettelmann, and R. Redmer, Thermal evolution of Uranus and Neptune. I. Adiabatic models, *Astron. Astrophys.* **632**, A70 (2019).
- [30] A. Vazan and R. Helled, Explaining the low luminosity of Uranus: a self-consistent thermal and structural evolution, *Astron. Astrophys.* **633**, A50 (2020).
- [31] L. Scheibe, N. Nettelmann, and R. Redmer, Thermal evolution of Uranus and Neptune. II. Deep thermal boundary layer, *Astron. Astrophys.* **650**, A200 (2021).
- [32] E. Bailey and D. J. Stevenson, Thermodynamically governed interior models of Uranus and Neptune, *Planet. Sci. J.* **2**, 64 (2021).
- [33] J. Heyd, G. E. Scuseria, and M. Ernzerhof, Hybrid functionals based on a screened coulomb potential, *J. Chem. Phys.* **118**, 8207 (2003).
- [34] J. Heyd and G. E. Scuseria, Assessment and validation of a screened coulomb hybrid density functional, *J. Chem. Phys.* **120**, 7274 (2004).
- [35] J. Heyd and G. E. Scuseria, Efficient hybrid density functional calculations in solids: Assessment of the heyd-scuseria-ernzerhof screened coulomb hybrid functional, *J. Chem. Phys.* **121**, 1187 (2004).
- [36] J. Heyd, J. E. Peralta, G. E. Scuseria, and R. L. Martin, Energy band gaps and lattice parameters evaluated with the heyd-scuseria-ernzerhof screened hybrid functional, *J. Chem. Phys.* **123**, 174101 (2005).
- [37] R. Kubo, Statistical-mechanical theory of irreversible processes. I. General theory and simple applications to magnetic and conduction problems, *J. Phys. Soc. Jpn.* **12**, 570 (1957).
- [38] D. A. Greenwood, The Boltzmann equation in the theory of electrical conduction in metals, *Proc. Phys. Soc., London* **71**, 585 (1958).
- [39] G. Kresse and J. Hafner, Ab initio molecular dynamics for liquid metals, *Phys. Rev. B* **47**, 558 (1993).
- [40] G. Kresse and J. Hafner, Ab initio molecular-dynamics simulation of the liquid-metal-amorphous-semiconductor transition in germanium, *Phys. Rev. B* **49**, 14251 (1994).
- [41] G. Kresse and J. Furthmüller, Efficient iterative schemes for ab initio total-energy calculations using a plane-wave basis set, *Phys. Rev. B* **54**, 11169 (1996).
- [42] G. Kresse and J. Furthmüller, Efficiency of ab-initio total energy calculations for metals and semiconductors using a plane-wave basis set, *Comput. Mater. Sci.* **6**, 15 (1996).
- [43] J. Hafner, Ab-initio simulations of materials using VASP: Density-functional theory and beyond, *J. Comput. Chem.* **29**, 2044 (2008).
- [44] P. Hohenberg and W. Kohn, Inhomogeneous electron gas, *Phys. Rev.* **136**, B864 (1964).
- [45] W. Kohn and L. J. Sham, Self-consistent equations including exchange and correlation effects, *Phys. Rev.* **140**, A1133 (1965).
- [46] N. D. Mermin, Thermal properties of the inhomogeneous electron gas, *Phys. Rev.* **137**, A1441 (1965).
- [47] M. Weinert and J. W. Davenport, Fractional occupations and density-functional energies and forces, *Phys. Rev. B* **45**, 13709 (1992).
- [48] R. M. Wentzcovitch, J. L. Martins, and P. B. Allen, Energy versus free-energy conservation in first-principles molecular dynamics, *Phys. Rev. B* **45**, 11372 (1992).
- [49] S. Nosé, Constant temperature molecular dynamics methods, *Prog. Theor. Phys. Suppl.* **103**, 1 (1991).
- [50] W. G. Hoover, Canonical dynamics: Equilibrium phase-space distributions, *Phys. Rev. A* **31**, 1695 (1985).
- [51] J. P. Perdew, K. Burke, and M. Ernzerhof, Generalized Gradient Approximation Made Simple, *Phys. Rev. Lett.* **77**, 3865 (1996).
- [52] M. French, A. Becker, W. Lorenzen, N. Nettelmann, M. Bethkenhagen, J. Wicht, and R. Redmer, *Ab initio* simulations for the material properties along Jupiter's adiabat, *Astrophys. J. Suppl. Ser.* **202**, 5 (2012).
- [53] M. Preising, W. Lorenzen, A. Becker, R. Redmer, M. D. Knudson, and M. P. Desjarlais, Equation of state and optical

- properties of warm dense helium, *Phys. Plasmas* **25**, 012706 (2018).
- [54] M. Guarguaglini, J.-A. Hernandez, T. Okuchi, P. Barroso, A. Benuzzi-Mounaix, M. Bethkenhagen, R. Bolis, E. Brambrink, M. French, Y. Fujimoto, R. Kodama, M. Koenig, F. Lefevre, K. Miyanishi, N. Ozaki, R. Redmer, T. Sano, Y. Umeda, T. Vinci, and A. Ravasio, Multishock comparison of dense gaseous H₂+He mixtures up to 30 GPa, *Sci. Rep.* **9**, 10155 (2019).
- [55] A. Baldereschi, Mean-value point in the Brillouin zone, *Phys. Rev. B* **7**, 5212 (1973).
- [56] E. S. Yakub and L. N. Yakub, Equation of state and second critical point of highly compressed nitrogen, *Fluid Phase Equilib.* **351**, 43 (2013).
- [57] D. A. Young, C.-S. Zha, R. Boehler, J. Yen, M. Nicol, A. S. Zinn, D. Schiferl, S. Kinkead, R. C. Hanson, and D. A. Pinnick, Diatomic melting curves to very high pressure, *Phys. Rev. B* **35**, 5353 (1987).
- [58] G. D. Mukherjee and R. Boehler, High-Pressure Melting Curve of Nitrogen and the Liquid-Liquid Phase Transition, *Phys. Rev. Lett.* **99**, 225701 (2007).
- [59] A. F. Goncharov, J. C. Crowhurst, V. V. Struzhkin, and R. J. Hemley, Triple Point on the Melting Curve and Polymorphism of Nitrogen at High Pressure, *Phys. Rev. Lett.* **101**, 095502 (2008).
- [60] D. Donadio, L. Spanu, I. Duchemin, F. Gygi, and G. Galli, Ab initio investigation of the melting line of nitrogen at high pressure, *Phys. Rev. B* **82**, 020102(R) (2010).
- [61] G. Weck, F. Datchi, G. Garbarino, S. Ninet, J.-A. Queyroux, T. Plisson, M. Mezouar, and P. Loubeyre, Melting Curve and Liquid Structure of Nitrogen Probed by X-ray Diffraction to 120 GPa, *Phys. Rev. Lett.* **119**, 235701 (2017).
- [62] M. Ross and F. Rogers, Polymerization, shock cooling, and the high-pressure phase diagram of nitrogen, *Phys. Rev. B* **74**, 024103 (2006).
- [63] S. Mazevet, J. D. Kress, L. A. Collins, and P. Blottiau, Quantum molecular-dynamics study of the electrical and optical properties of shocked liquid nitrogen, *Phys. Rev. B* **67**, 054201 (2003).
- [64] M. French and R. Redmer, Electronic transport in partially ionized water plasmas, *Phys. Plasmas* **24**, 092306 (2017).
- [65] M. Gajdoš, K. Hummer, G. Kresse, J. Furthmüller, and F. Bechstedt, Linear optical properties in the projector-augmented wave methodology, *Phys. Rev. B* **73**, 045112 (2006).
- [66] B. Holst, M. French, and R. Redmer, Electronic transport coefficients from ab initio simulations and application to dense liquid hydrogen, *Phys. Rev. B* **83**, 235120 (2011).
- [67] B. Holst, R. Redmer, and M. P. Desjarlais, Thermophysical properties of warm dense hydrogen using quantum molecular dynamics simulations, *Phys. Rev. B* **77**, 184201 (2008).
- [68] D. Knyazev and P. Levashov, Ab initio calculation of transport and optical properties of aluminum: Influence of simulation parameters, *Comput. Mater. Sci.* **79**, 817 (2013).
- [69] M. French, G. Röpke, M. Schörner, M. Bethkenhagen, M. P. Desjarlais, and R. Redmer, Electronic transport coefficients from density functional theory across the plasma plane, *Phys. Rev. E* **105**, 065204 (2022).
- [70] D. Vanderbilt, Soft self-consistent pseudopotentials in a generalized eigenvalue formalism, *Phys. Rev. B* **41**, 7892 (1990).
- [71] J. P. Perdew, P. Ziesche, and H. Eschrig, *Electronic Structure of Solids' 91* (Akademie Verlag, Berlin, 1991).
- [72] M. Bastea, Comment on Metallization of Fluid Nitrogen and the Mott Transition in Highly Compressed Low-Z Fluids, *Phys. Rev. Lett.* **92**, 129601 (2004).
- [73] W. Lorenzen, B. Holst, and R. Redmer, First-order liquid-liquid phase transition in dense hydrogen, *Phys. Rev. B* **82**, 195107 (2010).
- [74] J. M. McMahon, M. A. Morales, C. Pierleoni, and D. M. Ceperley, The properties of hydrogen and helium under extrem conditions, *Rev. Mod. Phys.* **84**, 1607 (2012).
- [75] N. F. Mott, The electrical properties of liquid mercury, *Philos. Mag.* **13**, 989 (1966).
- [76] P. P. Edwards, M. T. J. Lodge, F. Hensel, and R. Redmer, '... a metal conducts and a non-metal doesn't', *Phil. Trans. R. Soc., A* **368**, 941 (2010).
- [77] U. Zastrau, The high energy density scientific instrument at the European XFEL, *J. Synchrotron. Rad.* **28**, 1393 (2021).
- [78] R. Husband, A MHz X-ray diffraction set-up for dynamic compression experiments in the diamond anvil cell, *J. Synchrotron Rad.* **30**, 671 (2023).

Appendix A.

Convergence

The robustness and accuracy of numerical simulations are paramount studying of complex physical systems. This chapter discusses the convergence tests done to guarantee the rigour and credibility of our results. In Sec. A.1, we analyse the convergence of GEMC simulations for hydrogen and helium mixtures with respect to the particle number. The convergence of the DFT-MD simulations is analysed in Sec. A.2 with respect to the particle number, the plane wave energy cutoff, and the k-point sampling.

A.1. Convergence of the GEMC simulations for hydrogen and helium

If conducting GEMC simulations to simulate the miscibility of hydrogen and helium the convergence must be carefully checked. Using too low particle numbers results in swapping identities from hydrogen-rich to helium-rich between the two boxes several times; besides, vast fluctuations occur. This identity change occurs especially close to the lowest pressure at which demixing occurs. The convergence for different particle numbers is depicted in Fig. A.1. For only 512 particles, significant deviations occur. The results are well converged with only 2048 particles for pressures above 280 kbar. At the lowest pressure of 260 kbar, the 8192 particles used in our simulations are necessary to converge the results.

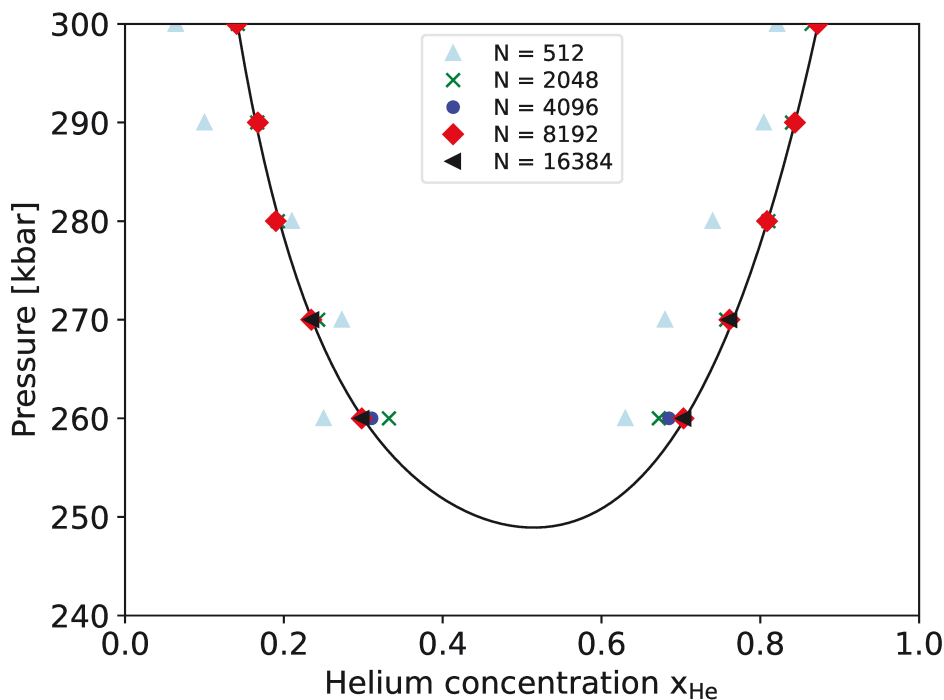


Fig. A.1.: GEMC simulations for hydrogen and helium mixtures using different particle number (color coded). The binodal curve, fitted to the converged results, is given by a black solid line.

A.2. Convergence of the DFT-MD simulations

Conducting DFT-MD simulations to explore the behaviour of hydrogen, water, and nitrogen necessitates rigorous convergence tests. Given that the primary results of these simulations are the EOS data, the pressure and the internal energy are of main interest. For pressure, which has well-defined absolute values, we examine the relative deviation $\frac{\Delta P}{P} = \frac{P_{\text{current}} - P}{P}$ between the current pressure P_{current} and the pressure P at the optimal settings. Achieving a value better than 1% is considered desirable. On the contrary, energy does not have an absolute defined value. Hence, we analyze only the absolute deviation $\Delta U = U_{\text{current}} - U$. A convergence target of better than a few meV/atom is aimed for these calculations.

A.2.1. Mixtures of hydrogen and water

We conducted convergence tests with respect to the particle number at 1000 and 2000 K. At 1000 K, the tests had been conducted at 0.4367 g/cm^3 for pure water, at 0.33 g/cm^3 for a mixture of $x_{\text{H}_2\text{O}} = 0.5$, and at 0.18 g/cm^3 for pure hydrogen. At 2000 K, the tests had been conducted at 1.984 g/cm^3 for pure water, at 1.394 g/cm^3 for a mixture of $x_{\text{H}_2\text{O}} = 0.5$, and at 0.392 g/cm^3 for pure hydrogen. The convergence tests are depicted in Fig. A.2 and Fig. A.3.

For 1000 K, the pressure for pure hydrogen is converged with 128 hydrogen molecules compared to 192 hydrogen molecules. The pressure of the mixture of $x_{\text{H}_2\text{O}} = 0.5$ is converged

with 64:64 H₂:H₂O molecules using 96:96 H₂:H₂O molecules as a reference. At 1000 K, we compared the results obtained by using the BMVP with a MP $2 \times 2 \times 2$ set to sample the Brillouin zone and did not find significant differences. We decided to use the following ratios of N_{H₂}:N_{H₂O} molecules in our simulation boxes: 128:0, 128:3, 128:10, 128:18, 128:30, 108:36, 48:80, 64:64, 40:64, 21:64, 10:64, 0:64. For the higher densities and temperatures our simulations would be converged with significant less particles. For simplification, however, we used the same particle number for every ρ -T condition.

We computed the pressure and internal energy employing plane wave cutoffs ranging from 700 eV to 1300 eV, and our analysis revealed that a cutoff of 1100 eV is sufficient for accurate results. The corresponding outcomes are illustrated in Fig. A.4 and Fig. A.5. It is important to note that we specifically tested the plane wave cutoff for hydrogen and water mixtures with a composition of $x_{\text{H}_2\text{O}} = 0.5$. This choice is based on the observation that the convergence behaviour with respect to the plane wave cutoff remains consistent across different concentrations.

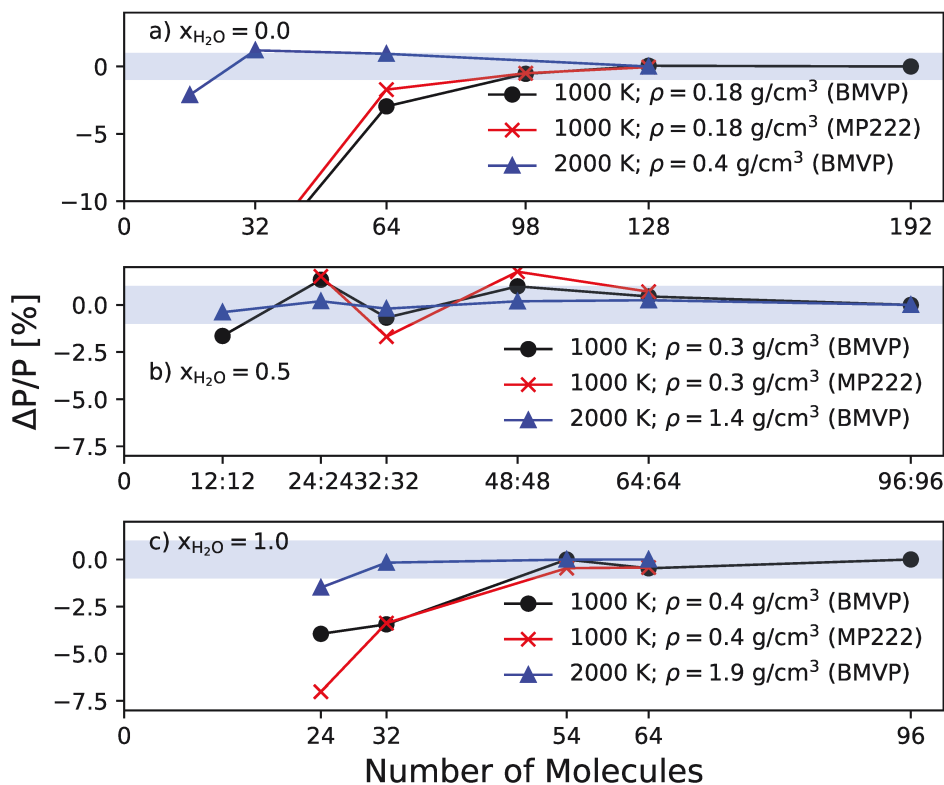


Fig. A.2.: Pressure convergence for hydrogen and water. Panel a) shows the results for pure hydrogen, panel b) for a mixture of $x_{H_2O} = 0.5$, and panel c) for pure water. The light blue area marks the converge better than 1.0%.

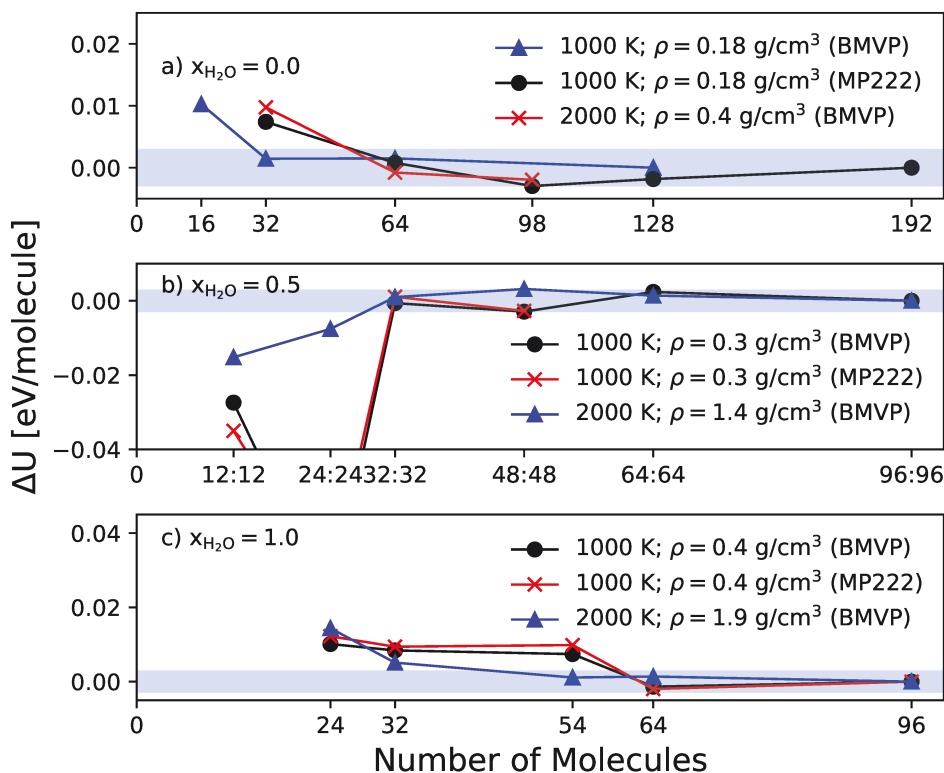


Fig. A.3.: Energy convergence for hydrogen and water. Panel a) shows the results for pure hydrogen, panel b) for a mixture of $x_{H_2O} = 0.5$, and panel c) for pure water. The light blue area marks convergence better than 0.003 eV.

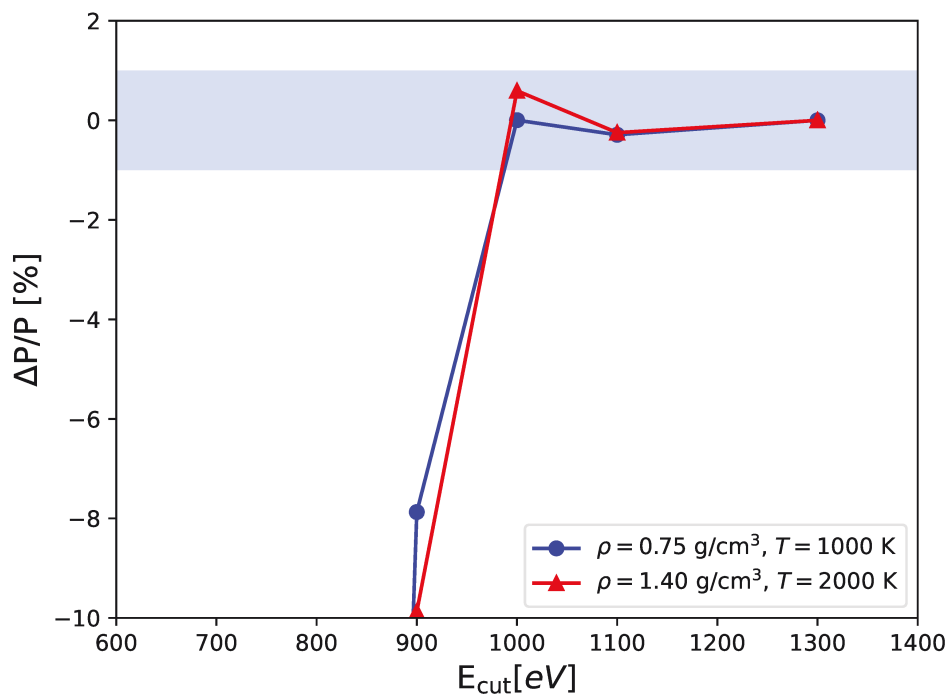


Fig. A.4.: Convergence of pressure concerning the plane wave cutoff is assessed at two temperatures and densities. The shaded blue region signifies achieved convergence better than 1%.

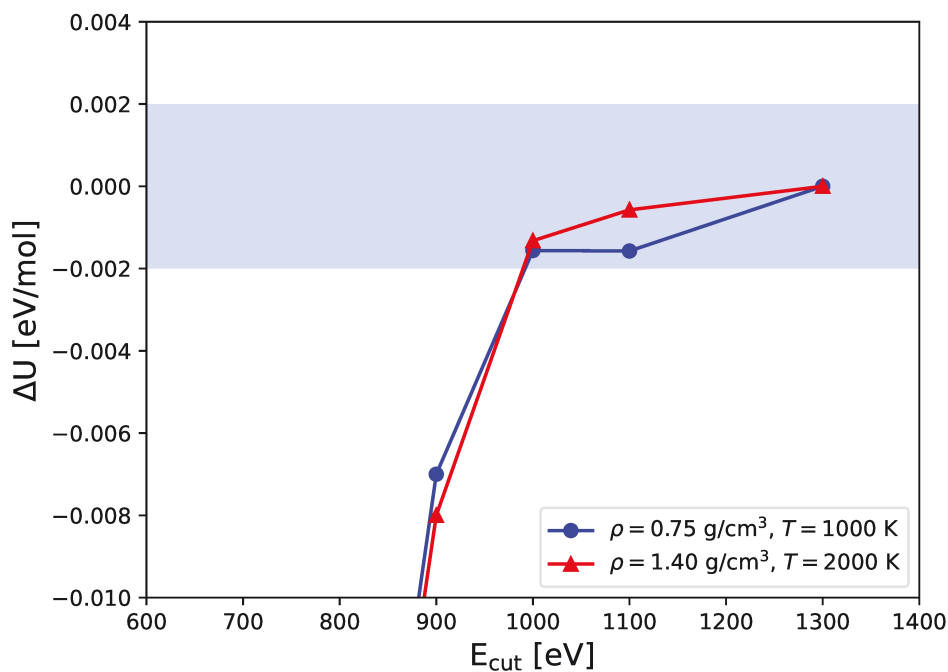


Fig. A.5.: Convergence of energy concerning the plane wave cutoff is assessed at two temperatures and densities. The shaded blue region signifies achieved convergence better than 2 meV per molecule.

A.2.2. Nitrogen

This section shows convergence tests for dense fluid nitrogen. We check pressure and energy convergence with respect to the plane wave cutoff. By investigating a phase transition, the convergence of the transition pressure needs to be checked very carefully, not only at one single density and temperature condition. Additionally, the convergence of the electrical conductivity with respect to the k -point set and particle number is analysed.

Convergence of the DFT-MD simulations for nitrogen

We calculated the LL-PT at a temperature of 2000 K for particle numbers between 64 and 512 nitrogen atoms using the BMVP or an MP $2 \times 2 \times 2$ set to sample the Brillouin zone. The results are shown in Fig. A.6. The simulations with 128 particles and an MP $2 \times 2 \times 2$ set are converged. However, we used 256 particles and the BMVP to converge the transition pressure fully. Conducting simulations with better \mathbf{k} -point sampling, e.g. an MP $4 \times 4 \times 4$ set, might lead to converged results even with lower particle numbers. However, this simulation scheme is computationally very inefficient.

Moreover, we checked the convergence of the plane-wave cutoff with respect to pressure and energy, see Fig. A.7 and A.8, respectively. A plane wave cutoff of 1000 eV leads to very good convergence of better than 1% and 2 meV, respectively.

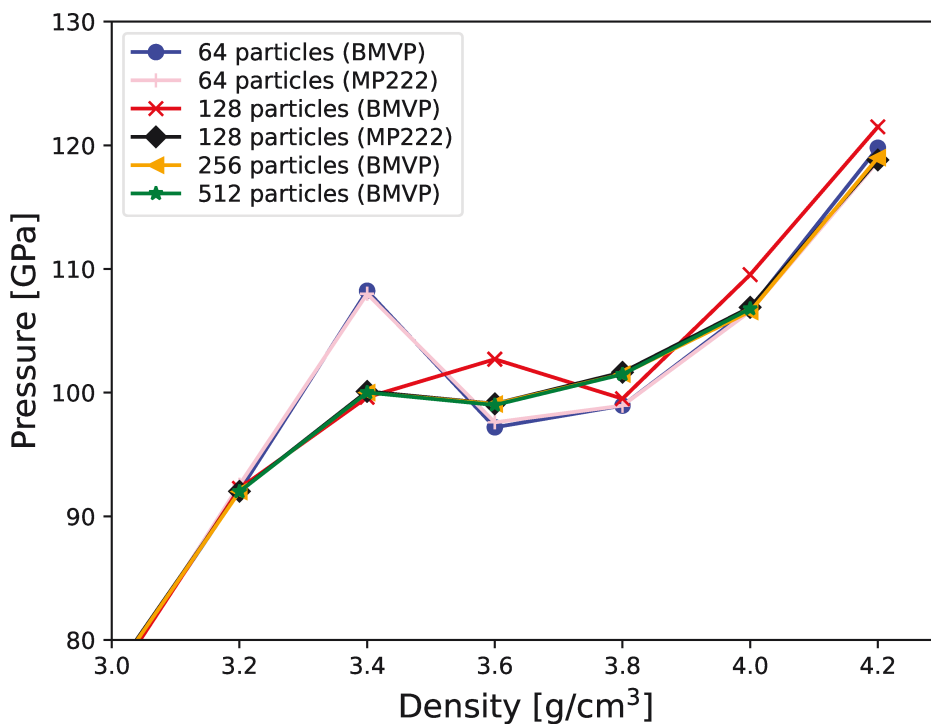


Fig. A.6.: LL-PT for dense fluid nitrogen at 2000 K calculated using DFT-MD simulations with different particle numbers and k -point sets (color coded).

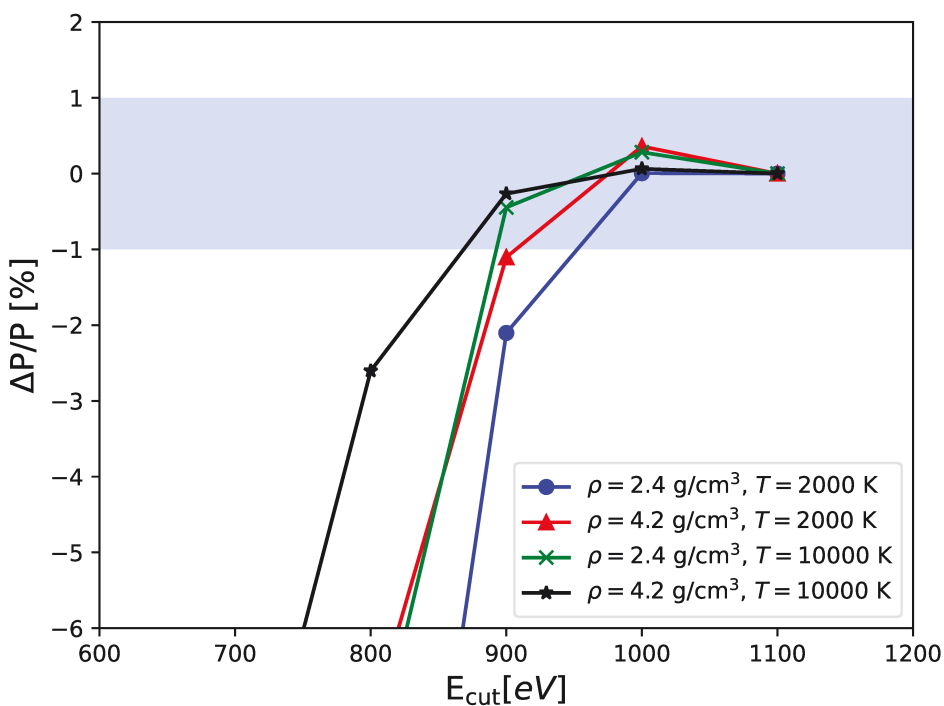


Fig. A.7.: Convergence of pressure concerning the plane wave cutoff is assessed at temperatures of 2000 and 10000 K, considering two distinct densities. The shaded blue region signifies achieved convergence better than 1%.

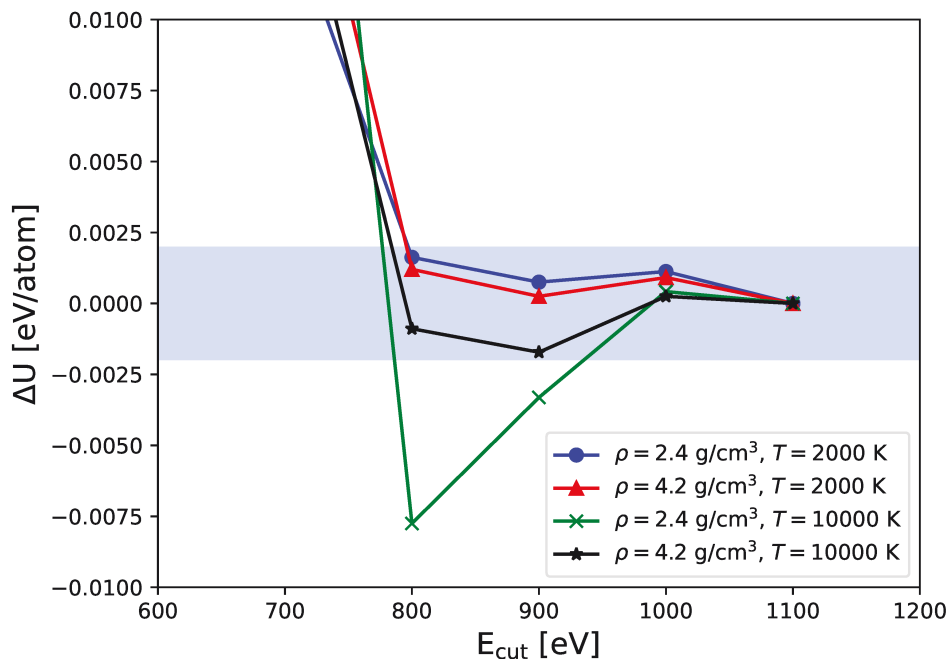


Fig. A.8.: Convergence of energy concerning to the plane wave cutoff at is assessed at temperatures of 2000 K and 10000 K, considering two distinct densities. The shaded blue region signifies achieved convergence better than 2 meV per atom.

Convergence of the electrical conductivity for nitrogen

The convergence patterns of conductivity with respect to both k-points and particle number may differ from those observed for thermodynamic quantities. Consequently, supplementary convergence tests are essential. The relative deviation of the static conductivity at the current setting is compared to the best result using the relation $\frac{\Delta\sigma}{\sigma} = \frac{\sigma_{current} - \sigma}{\sigma}$. The best result, also called reference value, is always calculated with 256 particles and MP $3 \times 3 \times 3$. In Fig. A.9, the results for 3000 K and densities of 2.4 and 4.2 g/cm³ are shown in blue and red, respectively. For 64 particles, the results are converged using an MP $2 \times 2 \times 2$ set but not using the BMVP to sample the Brillouin zone. For an MP $1 \times 1 \times 1$ set, which corresponds to the Γ point, vast deviations occur. Additionally, the results are converged using the BMVP and 256 particles. We used 256 particles and the BMVP to calculate the conductivities using the computationally more expensive HSE functional. This procedure allowed to calculate the band gap closure accurately. The convergence tests at 10000 K are depicted in Fig. A.10. Again, for an MP $1 \times 1 \times 1$ set, vast deviations occur. At higher temperatures, the conductivities already have metallic-like values. Hence, we used the PBE functional and only 64 particles and a MP $3 \times 3 \times 3$ set, yielding well-converged results compared to the reference value.

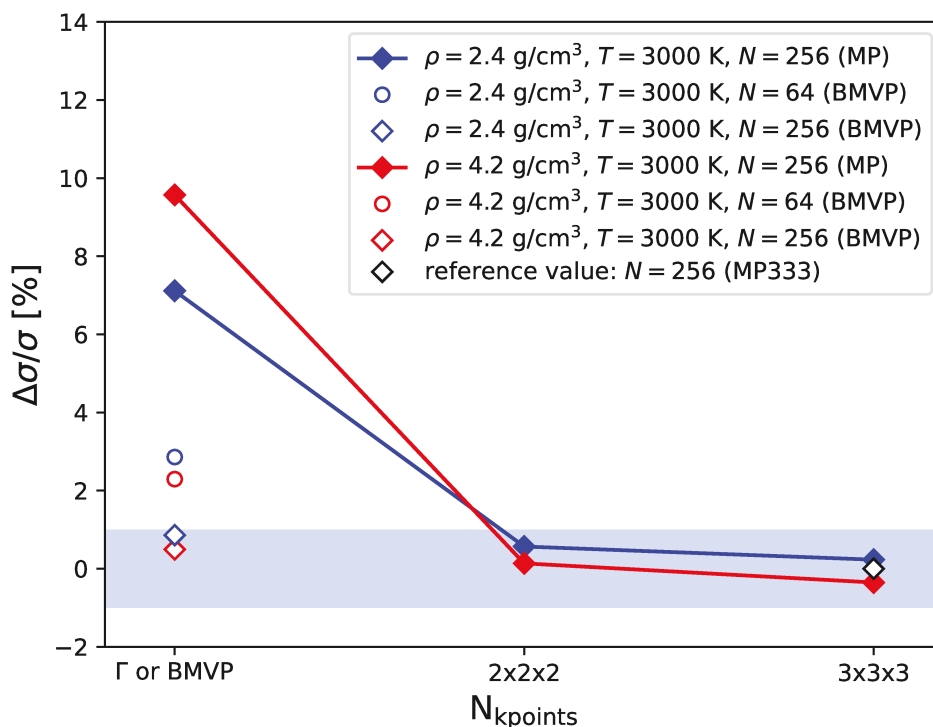


Fig. A.9.: Convergence analysis of electrical conductivity concerning the number of particles and k -point sampling at 3000 K. The blue color represents a density of 2.4 g/cm^3 , while the red color corresponds to a density of 4.2 g/cm^3 . Results obtained using MP: filled symbols; BMVP: open symbols. Results with 256 particles: colored diamonds, 64 particles: colored circles. The blue shaded area indicates convergence better than 1%.

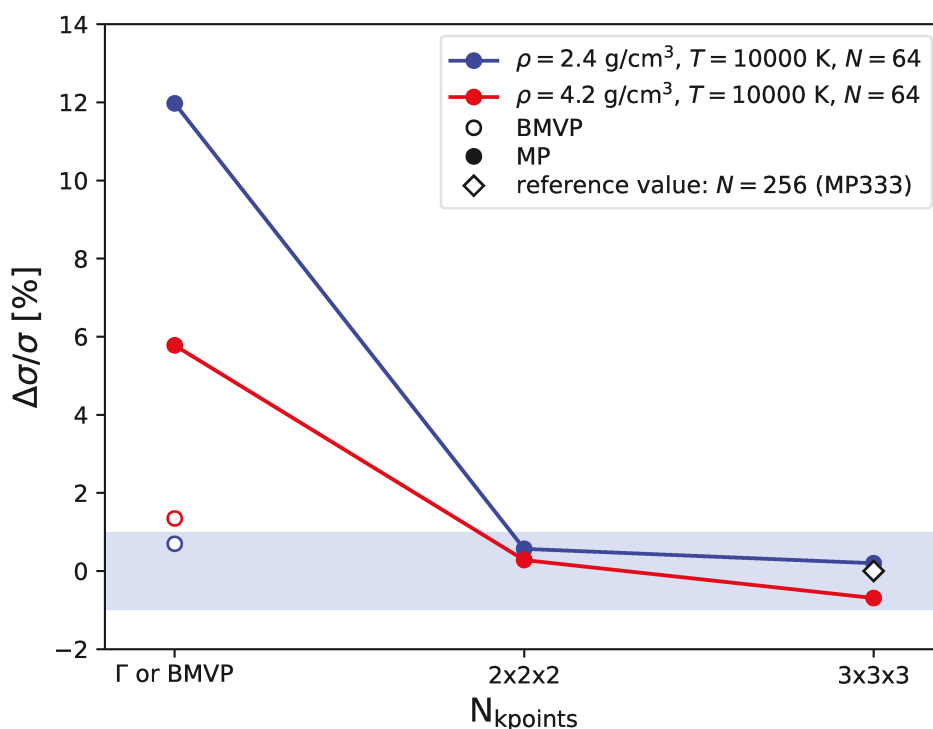


Fig. A.10.: Convergence analysis of electrical conductivity concerning the number of particles and k -point sampling at 10000 K. The blue color represents a density of 2.4 g/cm^3 , while the red color corresponds to a density of 4.2 g/cm^3 . Results obtained using MP: filled symbols; BMVP: open symbols. The blue shaded area indicates convergence better than 1%.

Bibliography

- [1] R. Helled, N. Nettelmann, and T. Guillot, *Space Sci. Rev.* **216** (2020).
- [2] E. C. Stone and A. L. Lane, *Science* **204**, 945 (1979).
- [3] E. C. Stone and A. L. Lane, *Science* **206**, 925 (1979).
- [4] T. Guillot, *Science* **286**, 72 (1999).
- [5] J. M. Greer and G. H. Gudfinnsson, *The Earth's Mantle: Composition, Structure, and Evolution* (American Geophysical Union, 2009).
- [6] J. L. Vago, F. Westall, L. S. S. W. G. Pasteur Instrument Teams, O. Contributors, A. J. Coates, R. Jaumann, O. Korablev, V. Ciarletti, I. Mitrofanov, J.-L. Josset, M. C. De Sanctis, J.-P. Bibring, F. Rull, F. Goesmann, H. Steininger, W. Goetz, W. Brinckerhoff, C. Szopa, F. Raulin, H. G. M. Edwards, L. G. Whyte, A. G. Fairén, J. Bridges, E. Hauber, G. G. Ori, S. Werner, D. Loizeau, R. O. Kuzmin, R. M. E. Williams, J. Flahaut, F. Forget, D. Rodionov, H. Svedhem, E. Sefton-Nash, G. Kminek, L. Lorenzoni, L. Joudrier, V. Mikhailov, A. Zashchirinskiy, S. Alexashkin, F. Calantropio, A. Merlo, P. Poulakis, O. Witasse, O. Bayle, S. Bayón, U. Meierhenrich, J. Carter, J. M. García-Ruiz, P. Baglioni, A. Haldermann, A. J. Ball, A. Debus, R. Lindner, F. Haessig, D. Monteiro, R. Trautner, C. Volland, P. Rebeyre, D. Gouly, F. Didot, S. Durrant, E. Zekri, D. Koschny, A. Toni, G. Visentin, M. Zwick, M. van Winnendael, M. Azkarate, C. Carreau, and the ExoMars Project Team, *Astrobiology* **17**, 471 (2017).
- [7] S. C. Dermott, *Planetary Ring Systems* (Cambridge University Press, 1999).
- [8] M. Dougherty, L. Esposito, and K. L.M., *Saturn after Cassini-Huygens* (Springer, 2019).
- [9] A. P. Ingersoll, *Voyages of Discovery: The Missions of the Space Age* (Harvard University Press, 2014).
- [10] L. Scheibe, N. Nettelmann, and R. Redmer, *Astron. Astrophys.* **632**, A70 (2019).
- [11] M. Bethkenhagen, E. R. Meyer, S. Hamel, N. Nettelmann, M. French, L. Scheibe, C. Ticknor, L. A. Collins, J. D. Kress, J. J. Fortney, and R. Redmer, *Astrophys. J.* **848**, 67 (2017).
- [12] J. J. Fortney and W. B. Hubbard, *Icarus* **164**, 228 (2003).
- [13] R. Helled and T. Guillot, *Internal Structure of Giant and Icy Planets: Importance of Heavy Elements and Mixing* (Springer International Publishing, Cham, 2018).
- [14] J. J. Fortney and N. Nettelmann, *Space Sci. Rev.* **152**, 423 (2010).
- [15] T. Guillot, *Exp. Astron.* **54**, 1027 (2022).

- [16] S. X. Hu, B. Militzer, V. N. Goncharov, and S. Skupsky, *Phys. Rev. B* **84**, 224109 (2011).
- [17] A. B. Zylstra, O. A. Hurricane, D. A. Callahan, A. L. Kritcher, J. E. Ralph, H. F. Robey, J. S. Ross, C. V. Young, K. L. Baker, D. T. Casey, T. Döppner, L. Divol, M. Hohenberger, S. Le Pape, A. Pak, P. K. Patel, R. Tommasini, S. J. Ali, P. A. Amendt, L. J. Atherton, B. Bachmann, D. Bailey, L. R. Benedetti, L. Berzak Hopkins, R. Betti, S. D. Bhandarkar, J. Biener, R. M. Bionta, N. W. Birge, E. J. Bond, D. K. Bradley, T. Braun, T. M. Briggs, M. W. Bruhn, P. M. Celliers, B. Chang, T. Chapman, H. Chen, C. Choate, A. R. Christopherson, D. S. Clark, J. W. Crippen, E. L. Dewald, T. R. Dittrich, M. J. Edwards, W. A. Farmer, J. E. Field, D. Fittinghoff, J. Frenje, J. Gaffney, M. Gatu Johnson, S. H. Glenzer, G. P. Grim, S. Haan, K. D. Hahn, G. N. Hall, B. A. Hammel, J. Harte, E. Hartouni, J. E. Heebner, V. J. Hernandez, H. Herrmann, M. C. Herrmann, D. E. Hinkel, D. D. Ho, J. P. Holder, W. W. Hsing, H. Huang, K. D. Humbird, N. Izumi, L. C. Jarrott, J. Jeet, O. Jones, G. D. Kerbel, S. M. Kerr, S. F. Khan, J. Kilkenny, Y. Kim, H. Geppert Kleinrath, V. Geppert Kleinrath, C. Kong, J. M. Koning, J. J. Kroll, M. K. G. Kruse, B. Kustowski, O. L. Landen, S. Langer, D. Larson, N. C. Lemos, J. D. Lindl, T. Ma, M. J. MacDonald, B. J. MacGowan, A. J. Mackinnon, S. A. MacLaren, A. G. MacPhee, M. M. Marinak, D. A. Mariscal, E. V. Marley, L. Masse, K. Meaney, N. B. Meezan, P. A. Michel, M. Millot, J. L. Milovich, J. D. Moody, A. S. Moore, J. W. Morton, T. Murphy, K. Newman, J.-M. G. Di Nicola, A. Nikroo, R. Nora, M. V. Patel, L. J. Pelz, J. L. Peterson, Y. Ping, B. B. Pollock, M. Ratledge, N. G. Rice, H. Rinderknecht, M. Rosen, M. S. Rubery, J. D. Salmonson, J. Sater, S. Schiaffino, D. J. Schlossberg, M. B. Schneider, C. R. Schroeder, H. A. Scott, S. M. Sepke, K. Sequoia, M. W. Sherlock, S. Shin, V. A. Smalyuk, B. K. Spears, P. T. Springer, M. Stadermann, S. Stoupin, D. J. Strozzi, L. J. Suter, C. A. Thomas, R. P. J. Town, E. R. Tubman, C. Trosseille, P. L. Volegov, C. R. Weber, K. Widmann, C. Wild, C. H. Wilde, B. M. Van Wonterghem, D. T. Woods, B. N. Woodworth, M. Yamaguchi, S. T. Yang, and G. B. Zimmerman, *Nature* **601**, 542 (2022).
- [18] R. Redmer, *Phys. Rep.* **282**, 35 (1997).
- [19] W. Lorenzen, B. Holst, and R. Redmer, *Phys. Rev. B* **82**, 195107 (2010).
- [20] L. N. Yakub, *Low Temp. Phys.* **42**, 1 (2016).
- [21] W.-D. Kraeft, D. Kremp, W. Ebeling, and G. Röpke, *Quantum Statistics of Charged Particle Systems* (Akademie-Verlag Berlin, 1986).
- [22] D. Kremp, V. Bezukrovniy, W. D. Kraeft, and M. Schlanges, *Contrib. Plasma Phys.* **45**, 266 (2005).
- [23] R. Boehler, *Rev. of Geophys.* **38**, 221 (2000).
- [24] C. Cavazzoni, G. L. Chiarotti, S. Scandolo, E. Tosatti, M. Bernasconi, and M. Parrinello, *Science* **283**, 44 (1999).

- [25] F. Graziani, M. Desjarlais, R. Redmer, and S. Trickey, *Frontiers and Challenges in Warm Dense Matter* (Springer International Publishing, 2014).
- [26] A. Szabo and N. Ostlund, *Modern Quantum Chemistry: Introduction to Advanced Electronic Structure Theory* (Dover Publications, 1996).
- [27] C. J. Cramer, *Essentials of Computational Chemistry* (John Wiley & Sons, Ltd., Chichester, 2002).
- [28] B. Militzer and D. M. Ceperley, *Phys. Rev. Lett.* **85**, 1890 (2000).
- [29] F. Lin, M. A. Morales, K. T. Delaney, C. Pierleoni, R. M. Martin, and D. M. Ceperley, *Phys. Rev. Lett.* **103**, 256401 (2009).
- [30] C. Pierleoni, M. A. Morales, G. Rillo, and D. M. Ceperley, *Proceedings of the National Academy of Sciences* **113**, 4953 (2016).
- [31] D. M. Ceperley, *Rev. Minera. and Geochem.* **71**, 129 (2010).
- [32] Z. He, M. Rödel, J. Lütgert, A. Bergermann, M. Bethkenhagen, D. Chekrygina, T. E. Cowan, A. Descamps, M. French, E. Galtier, A. E. Gleason, G. D. Glenn, S. H. Glenzer, Y. Inubushi, N. J. Hartley, J.-A. Hernandez, B. Heuser, O. S. Humphries, N. Kamimura, K. Katagiri, D. Khaghani, H. J. Lee, E. E. McBride, K. Miyanishi, B. Nagler, B. Ofori-Okai, N. Ozaki, S. Pandolfi, C. Qu, D. Ranjan, R. Redmer, C. Schoenwaelder, A. K. Schuster, M. G. Stevenson, K. Sueda, T. Togashi, T. Vinci, K. Voigt, J. Vorberger, M. Yabashi, T. Yabuuchi, L. M. V. Zinta, A. Ravasio, and D. Kraus, *Sci. Adv.* **8**, eabo0617 (2022).
- [33] D. Kraus, N. J. Hartley, S. Frydrych, A. K. Schuster, K. Rohatsch, M. Rödel, T. E. Cowan, S. Brown, E. Cunningham, T. van Driel, L. B. Fletcher, E. Galtier, E. J. Gamboa, A. Laso Garcia, D. O. Gericke, E. Granados, P. A. Heimann, H. J. Lee, M. J. MacDonald, A. J. MacKinnon, E. E. McBride, I. Nam, P. Neumayer, A. Pak, A. Pelka, I. Prencipe, A. Ravasio, R. Redmer, A. M. Saunders, M. Schölmerich, M. Schörner, P. Sun, S. J. Turner, A. Zettl, R. W. Falcone, S. H. Glenzer, T. Döppner, and J. Vorberger, *Phys. Plas.* **25**, 056313 (2018).
- [34] R. Betti and O. A. Hurricane, *Nature Phys.* **12**, 435 (2016).
- [35] A. B. Zylstra, A. L. Kritcher, O. A. Hurricane, D. A. Callahan, J. E. Ralph, D. T. Casey, A. Pak, O. L. Landen, B. Bachmann, K. L. Baker, L. Berzak Hopkins, S. D. Bhandarkar, J. Biener, R. M. Bionta, N. W. Birge, T. Braun, T. M. Briggs, P. M. Celliers, H. Chen, C. Choate, D. S. Clark, L. Divol, T. Döppner, D. Fittinghoff, M. J. Edwards, M. Gatu Johnson, N. Gharibyan, S. Haan, K. D. Hahn, E. Hartouni, D. E. Hinkel, D. D. Ho, M. Hohenberger, J. P. Holder, H. Huang, N. Izumi, J. Jeet, O. Jones, S. M. Kerr, S. F. Khan, H. Geppert Kleinrath, V. Geppert Kleinrath, C. Kong, K. M. Lamb, S. Le Pape, N. C. Lemos, J. D. Lindl, B. J. MacGowan, A. J. Mackinnon, A. G. MacPhee, E. V. Marley,

- K. Meaney, M. Millot, A. S. Moore, K. Newman, J.-M. G. Di Nicola, A. Nikroo, R. Nora, P. K. Patel, N. G. Rice, M. S. Rubery, J. Sater, D. J. Schlossberg, S. M. Sepke, K. Sequoia, S. J. Shin, M. Stadermann, S. Stoupin, D. J. Strozzi, C. A. Thomas, R. Tommasini, C. Trosseille, E. R. Tubman, P. L. Volegov, C. R. Weber, C. Wild, D. T. Woods, S. T. Yang, and C. V. Young, *Phys. Rev. E* **106**, 025202 (2022).
- [36] A. G. Opp, *Science* **188**, 447 (1975).
- [37] S. K. Ocker, J. M. Cordes, S. Chatterjee, D. A. Gurnett, W. S. Kurth, and S. R. Spangler, *Nature Astron.* **5**, 761 (2021).
- [38] R. D. T. Strauss, *Nature Astron.* **3**, 963 (2019).
- [39] D. Meltzer, A. Eichblatt, and F. C. Monteiro, *Space Sci. Rev.* **215**, 123 (2019).
- [40] T. V. Johnson and D. L. Matson, *Science* **257**, 635 (1992).
- [41] S. J. Bolton, A. Adriani, V. Adumitroaie, M. Allison, J. Anderson, S. Atreya, T. Becker, T. Becker, D. T. Blewett, M. Bushroo, G. Clark, A. Coradini, R. A. De Boy, T. Economou, R. Espiritu, M. Felici, S. Glenn, A. Hains, J. Hayes, N. Hinners, L. Horn, A. P. Ingersoll, M. Janssen, T. V. Johnson, H. Korth, C. Little, P. Mahaffy, B. Mauk, M. McIntyre, R. McNutt, E. Melin, M. Milazzo, G. Orton, T. Owen, M. Patrick, G. Rogers, E. Roelof, M. Sataric, B. Selvin, A. L. Sprague, F. Stefano, A. I. Stewart, D. F. Strobel, J. R. Szalay, A. Szmant, H. Throop, P. Valek, B. Wallis, K. Warfield, S. Watanabe, J. Wilson, and X. Zhang, *Space Sci. Rev.* **156**, 671 (2010).
- [42] S. J. Bolton, J. Lunine, D. Stevenson, J. E. P. Connerney, S. Levin, T. C. Owen, F. Bagenal, D. Gautier, A. P. Ingersoll, G. S. Orton, T. Guillot, W. Hubbard, J. Bloxham, A. Coradini, S. K. Stephens, P. Mokashi, R. Thorne, and R. Thorpe, *Space Sci. Rev.* **213**, 5 (2017).
- [43] K. E. Mandt, *Science* **379**, 640 (2023).
- [44] C. R. Mankovich and J. J. Fortney, *Astrophys. J.* **889**, 51 (2020).
- [45] R. Püstow, N. Nettelmann, W. Lorenzen, and R. Redmer, *Icarus* **267**, 323 (2016).
- [46] J. J. Fortney and W. B. Hubbard, *Astrophys. J.* **608**, 1039 (2004).
- [47] J. Leconte and G. Chabrier, *Astro. & Astrophys.* **540**, 13 (2012).
- [48] M. Schöttler, *Miscibility gap of hydrogen-helium mixtures at high pressures and temperatures*, Ph.D. thesis, University of Rostock (2018).
- [49] M. Schöttler and R. Redmer, *Phys. Rev. Lett.* **120**, 115703 (2018).
- [50] M. Schöttler and R. Redmer, *Journal of Plasma Physics* **85**, 945850201 (2019).
- [51] M. A. Morales, J. M. McMahon, C. Pierleoni, and D. M. Ceperley, *Phys. Rev. Lett.* **110**, 065702 (2013).

- [52] D. J. Stevenson, *Annu. Rev. Earth Planet. Sci.* **10**, 257 (1982).
- [53] H. F. Wilson and B. Militzer, *The Astrophysical Journal* **745**, 54 (2011).
- [54] T. Guillot, D. J. Stevenson, W. B. Hubbard, and D. Saumon, in *Jupiter*, edited by F. Bagenal, T. E. Dowling, and W. B. McKinnon (Cambridge Univ. Press, 2004).
- [55] M. Bethkenhagen, M. French, and R. Redmer, *J. Chem. Phys.* **138**, 234504 (2013).
- [56] M. S. Marley, P. Gómez, and M. Podolak, *J. Geophys. Res.* **100**, 23349 (1995).
- [57] M. Podolak, A. Weizman, and M. Marley, *Planet. Space Sci.* **43**, 1517 (1995).
- [58] N. Nettelmann, R. Helled, J. Fortney, and R. Redmer, *Planet. Space Sci.* **77**, 143 (2013).
- [59] N. Nettelmann, K. Wang, J. Fortney, S. Hamel, S. Yellamilli, M. Bethkenhagen, and R. Redmer, *Icarus* **275**, 107 (2016).
- [60] N. A. Teanby, P. G. J. Irwin, J. I. Moses, and R. Helled, *Philos. Trans. Royal Soc. A* **378**, 20190489 (2020).
- [61] L. Scheibe, N. Nettelmann, and R. Redmer, *Astron. Astrophys.* **650**, A200 (2021).
- [62] M. French, *New J. Phys.* **21**, 023007 (2019).
- [63] B. J. Conrath, D. Gautier, R. A. Hanel, and J. S. Hornstein, *Astrophys. J., Part 1* **282**, 807 (1984).
- [64] B. J. Conrath and D. Gautier, *Icarus* **144**, 124 (2000).
- [65] T. Koskinen and S. Guerlet, *Icarus* **307**, 161 (2018).
- [66] R. K. Achterberg and F. M. Flasar, *Planet. Sci. J.* **1**, 30 (2020).
- [67] D. J. Stevenson and E. E. Salpeter, *Astrophys. J. Suppl. Ser.* **35**, 221 (1977).
- [68] C. R. Mankovich and J. Fuller, *Nature Astronomy* **5**, 1103 (2021).
- [69] S. Brygoo, P. Loubeyre, M. Millot, J. R. Rygg, P. M. Celliers, J. H. Eggert, R. Jeanloz, and G. W. Collins, *Nature* **593**, 517 (2021).
- [70] P. Loubeyre, R. Le Toullec, and J. P. Pinceaux, *Phys. Rev. B* **36**, 3723 (1987).
- [71] E. Bailey and D. J. Stevenson, *Planet. Sci. J.* **2**, 64 (2021).
- [72] M. Podolak, J. Podolak, and M. Marley, *Planet. Space Sci.* **48**, 143 (2000).
- [73] M. Podolak, R. Helled, and G. Schubert, *Mon. Not. R. Astron. Soc.* **487**, 2653 (2019).
- [74] N. Nettelmann, J. Fortney, U. Kramm, and R. Redmer, *Astrophys. J.* **733**, 2 (2011).
- [75] A. Vazan and R. Helled, *Astron. Astrophys.* **633**, A50 (2020).

- [76] K. Vlasov, A. Audétat, and H. Keppler, *Contrib. to Mineral. Petrol.* **178**, 36 (2023).
- [77] E. Bali, A. Audétat, and H. Keppler, *Nature* **495**, 220 (2013).
- [78] M. J. de Oliveira, *Equilibrium Thermodynamics*, Graduate Texts in Physics (Springer, 2017).
- [79] W. Nolting, *Theoretical Physics 5: Thermodynamics* (Springer International Publishing, 2017).
- [80] F. Weinhold, *Classical and Geometrical Theory of Chemical and Phase Thermodynamics* (John Wiley & Sons, Inc., 2008).
- [81] D. Young, *Phase Diagrams of the Elements* (University of California Press, 2023).
- [82] A. A. Bartlett, *The Physics Teacher* **13**, 545 (1975).
- [83] J.-A. Korell, M. French, G. Steinle-Neumann, and R. Redmer, *Phys. Rev. Lett.* **122**, 086601 (2019).
- [84] E. Kim and M. H. W. Chan, *Science* **305**, 1941 (2004).
- [85] O. Penrose and L. Onsager, *Phys. Rev.* **104**, 576 (1956).
- [86] E. Ising, *Zeitschrift für Physik* **31**, 253 (1925).
- [87] L. D. Landau, *Zhurnal Eksperimental'noi i Teoreticheskoi Fiziki* **7**, 19 (1937).
- [88] R. B. Potts, *Math. Proc. Camb. Philos. Soc.* **48**, 106 (1952).
- [89] V. L. Ginzburg and L. D. Landau, *Zhurnal Eksperimental'noi i Teoreticheskoi Fiziki* **20**, 1064 (1950).
- [90] J. M. Kosterlitz and D. J. Thouless, *Journal of Physics C: Solid State Physics* **6**, 1181 (1973).
- [91] K. G. Wilson, *Physical Review B* **4**, 3174 (1971).
- [92] M. D. Knudson, M. P. Desjarlais, A. Becker, R. W. Lemke, K. R. Cochrane, M. E. Savage, D. E. Bliss, T. R. Mattsson, and R. Redmer, *Science* **348**, 1455 (2015).
- [93] G. Weck, F. Datchi, G. Garbarino, S. Ninet, J.-A. Queyroux, T. Plisson, M. Mezouar, and P. Loubeyre, *Phys. Rev. Lett.* **119**, 235701 (2017).
- [94] M. Preising and R. Redmer, *Phys. Rev. B* **100**, 184107 (2019).
- [95] J. Shi, Z. Liang, J. Wang, S. Pan, C. Ding, Y. Wang, H.-T. Wang, D. Xing, and J. Sun, *Phys. Rev. Lett.* **131**, 146101 (2023).
- [96] H. Stanley, *Introduction to Phase Transitions and Critical Phenomena*, International series of monographs on physics (Clarendon Press, 1971).

- [97] J. Yeomans, *Statistical Mechanics of Phase Transitions* (Clarendon Press, 1992).
- [98] G. Jaeger, Arch. Hist. Exact Sci. **53**, 51 (1998).
- [99] M. E. Fisher, Physics Physique Fizika **3**, 255 (1967).
- [100] G. Mazzola, R. Helled, and S. Sorella, Phys. Rev. Lett. **120**, 025701 (2018).
- [101] P. M. Celliers, M. Millot, S. Brygoo, R. S. McWilliams, D. E. Fratanduono, J. R. Rygg, A. F. Goncharov, P. Loubeyre, J. H. Eggert, J. L. Peterson, N. B. Meezan, S. L. Pape, G. W. Collins, R. Jeanloz, and R. J. Hemley, Science **361**, 677 (2018).
- [102] K. Ohta, K. Ichimaru, M. Einaga, S. Kawaguchi, K. Shimizu, T. Matsuoka, N. Hirao, and Y. Ohishi, Sci. Rep. **5**, 1 (2015).
- [103] J. Hinz, V. V. Karasiev, S. X. Hu, M. Zaghoo, D. Mejía-Rodríguez, S. B. Trickey, and L. Calderín, Phys. Rev. Res. **2**, 032065(R) (2020).
- [104] M. Zaghoo, A. Salamat, and I. F. Silvera, Phys. Rev. B **93**, 155128 (2016).
- [105] A. Tirelli, G. Tenti, K. Nakano, and S. Sorella, Phys. Rev. B **106**, L041105 (2022).
- [106] K. P. Driver and B. Militzer, Phys. Rev. B **93**, 064101 (2016).
- [107] B. Boates and S. A. Bonev, Phys. Rev. Lett. **102**, 015701 (2009).
- [108] B. Boates and S. A. Bonev, Phys. Rev. B **83**, 174114 (2011).
- [109] E. S. Yakub and L. N. Yakub, Fluid Ph. Equilib. **351**, 43 (2013).
- [110] M. Ross and F. Rogers, Phys. Rev. B **74**, 024103 (2006).
- [111] G. Zhao, H. Wang, M. C. Ding, X. G. Zhao, H. Y. Wang, and J. L. Yan, Phys. Rev. B **98**, 184205 (2018).
- [112] B. Militzer, F. m. c. Gygi, and G. Galli, Phys. Rev. Lett. **91**, 265503 (2003).
- [113] D. A. Young, C.-S. Zha, R. Boehler, J. Yen, M. Nicol, A. S. Zinn, D. Schiferl, S. Kinkead, R. C. Hanson, and D. A. Pinnick, Phys. Rev. B **35**, 5353 (1987).
- [114] G. D. Mukherjee and R. Boehler, Phys. Rev. Lett. **99**, 225701 (2007).
- [115] A. F. Goncharov, J. C. Crowhurst, V. V. Struzhkin, and R. J. Hemley, Phys. Rev. Lett. **101**, 095502 (2008).
- [116] D. Donadio, L. Spanu, I. Duchemin, F. Gygi, and G. Galli, Phys. Rev. B **82**, 020102 (2010).
- [117] S. Ulam and J. von Neumann, J. Am. Stat. Assoc. **44**, 335 (1949).

- [118] P. Glasserman, *Monte Carlo Methods in Financial Engineering*, Vol. 10 (Elsevier, 2004) pp. 239–271.
- [119] M. E. J. Newman and G. T. Barkema, Clarendon Press (1999).
- [120] M. P. Allen and D. J. Tildesley, *Computer Simulation of Liquids* (Oxford Science Publications, 1987).
- [121] D. Frenkel and B. Smit, in *Understanding Molecular Simulation (Second Edition)* (Academic Press, 2002).
- [122] N. Metropolis, A. W. Rosenbluth, M. N. Rosenbluth, A. H. Teller, and E. Teller, *J. Chem. Phys.* **21**, 1087 (1953).
- [123] W. Nolting, *Theoretical Physics 8: Statistical Physics* (Springer International Publishing, 2018).
- [124] A. Z. Panagiotopoulos, *Mol. Phys.* **61**, 813 (1987).
- [125] A. Z. Panagiotopoulos, N. Quirke, M. Stapleton, and D. Tildesley, *Mol. Phys.* **63**, 527 (1988).
- [126] A. Z. Panagiotopoulos, *Mol. Sim.* **9**, 1 (1992).
- [127] L. Zhang, Y. Yang, K. Yin, and Y. Liu, *Acta Geochim.* **42**, 409 (2023).
- [128] A. Bergermann, *Gibbs-ensemble Monte Carlo simulations for binary mixtures*, Masterarbeit, University of Rostock (2020).
- [129] Z. Li, C. Winisdoerffer, F. Soubiran, and R. Caracas, *Phys. Chem. Chem. Phys.* **23**, 311 (2021).
- [130] J. A. Schouten, A. de Kuijper, and J. P. J. Michels, *Phys. Rev. B* **44**, 6630 (1991).
- [131] E. Schrödinger, *Phys. Rev.* **28**, 1049 (1926).
- [132] W. Kohn, *Rev. Mod. Phys.* **71**, 1253 (1999).
- [133] P. Echenique and J. L. Alonso, *Mol. Phys.* **105**, 3057 (2007).
- [134] C. Pierleone, M. Morales, G. Rillo, M. Holzmann, and M. Ceperley, *Proc. Natl. Acad. Sci.* **85**, 1980 (2016).
- [135] W. Koch and M. C. Holthausen, “Front matter and index,” in *A Chemist’s Guide to Density Functional Theory* (John Wiley & Sons, Ltd, 2001).
- [136] M. Born and R. Oppenheimer, *Ann. Phys.* **389**, 457 (1927).
- [137] H. Hellmann, *Zeitschrift für Physik* **85**, 180 (1933).
- [138] R. P. Feynman, *Phys. Rev.* **56**, 340 (1939).

- [139] R. Car and M. Parrinello, *Phys. Rev. Lett.* **55**, 2471 (1985).
- [140] R. G. Parr and W. Yang, *Density-Functional Theory of Atoms and Molecules* (Oxford University Press, 1989).
- [141] R. M. Martin, *Electronic structure: basic theory and practical methods* (Cambridge Univ. Press, 2004).
- [142] R. M. Dreizler and E. K. U. Gross, *Density functional theory : an approach to the quantum many-body problem* (Springer, 1990).
- [143] J. Kohanoff, *Electronic structure calculations for solids and molecules: theory and computational methods* (Cambridge Univ. Press, 2006).
- [144] R. G. Parr, *Annu. Rev. Phys. Chem.* **34**, 631 (1983).
- [145] A. E. Mattsson, P. A. Schultz, M. P. Desjarlais, T. R. Mattsson, and K. Leung, *Model. Simul. Mater. Sci. Eng.* **13**, R1 (2005).
- [146] A. D. Becke, *J. Chem. Phys.* **140**, 18A301 (2014).
- [147] E. S. Kryachko and E. V. Ludeña, *Phys. Rep.* **544**, 123 (2014).
- [148] R. O. Jones and O. Gunnarsson, *Rev. Mod. Phys.* **61**, 689 (1989).
- [149] R. O. Jones, *Rev. Mod. Phys.* **87**, 897 (2015).
- [150] D. Marx and J. Hutter, *Ab initio molecular dynamics: basic theory and advanced methods* (Cambridge Univ. Press, Cambridge, 2009).
- [151] D. Rapaport, *The Art of Molecular Dynamics Simulation* (Cambridge Univ. Press, 2004).
- [152] V. H. Smith Jr. and I. Absar, *Isr. J. Chem.* **16**, 87 (1977).
- [153] P. Hohenberg and W. Kohn, *Phys. Rev.* **136**, B864 (1964).
- [154] W. Kohn and L. J. Sham, *Phys. Rev.* **140**, A1133 (1965).
- [155] N. D. Mermin, *Phys. Rev.* **137**, A1441 (1965).
- [156] J. M. Soler, E. Artacho, J. D. Gale, A. García, J. Junquera, P. Ordejón, and D. Sánchez-Portal, *J. Phys.: Condens. Matter* **14**, 2745 (2002).
- [157] V. Blum, R. Gehrke, F. Hanke, P. Havu, V. Havu, X. Ren, K. Reuter, and M. Scheffler, *Comput. Phys. Commun.* **180**, 2175 (2009).
- [158] G. Kresse and J. Hafner, *Phys. Rev. B* **47**, 558 (1993).
- [159] P. Giannozzi, S. Baroni, N. Bonini, M. Calandra, R. Car, C. Cavazzoni, D. Ceresoli, G. L. Chiarotti, M. Cococcioni, I. Dabo, A. Dal Corso, S. de Gironcoli, S. Fabris, G. Fratesi, R. Gebauer, U. Gerstmann, C. Gougoussis, A. Kokalj, M. Lazzeri, L. Martin-Samos,

- N. Marzari, F. Mauri, R. Mazzarello, S. Paolini, A. Pasquarello, L. Paulatto, C. Sbraccia, S. Scandolo, G. Sclauzero, A. P. Seitsonen, A. Smogunov, P. Umari, and R. M. Wentzcovitch, *J. Phys. Cond. Mat.* **21**, 395502 (2009).
- [160] X. Gonze, J.-M. Beuken, R. Caracas, F. Detraux, M. Fuchs, G.-M. Rignanese, L. Sindic, M. Verstraete, G. Zerah, F. Jollet, M. Torrent, A. Roy, M. Mikami, P. Ghosez, J.-Y. Raty, and D. Allan, *Comput. Mater. Sci.* **25**, 478 (2002).
- [161] M. D. Segall, P. J. D. Lindan, M. J. Probert, C. J. Pickard, P. J. Hasnip, S. J. Clark, and M. C. Payne, *J. Condens. Matter Phys.* **14**, 2717 (2002).
- [162] F. Bloch, *Zeitschrift für Physik* **52**, 555 (1929).
- [163] R. A. Evarestov and V. P. Smirnov, *Phys. Status Solidi B* **119**, 9 (1983).
- [164] A. Baldereschi, *Phys. Rev. B* **7**, 5212 (1973).
- [165] H. J. Monkhorst and J. D. Pack, *Phys. Rev. B* **13**, 5188 (1976).
- [166] P. E. Blöchl, *Phys. Rev. B* **50**, 17953 (1994).
- [167] G. Kresse and D. Joubert, *Phys. Rev. B* **59**, 1758 (1999).
- [168] N. Mardirossian and M. Head-Gordon, *Mol. Phys.* **115**, 2315 (2017).
- [169] U. Kleinschmidt, M. French, G. Steinle-Neumann, and R. Redmer, *Phys. Rev. B* **107**, 085145 (2023).
- [170] V. V. Karasiev, J. W. Dufty, and S. B. Trickey, *Phys. Rev. Lett.* **120**, 076401 (2018).
- [171] V. V. Karasiev, T. Sjostrom, J. Dufty, and S. B. Trickey, *Phys. Rev. Lett.* **112**, 076403 (2014).
- [172] A. Pribram-Jones, P. E. Grabowski, and K. Burke, *Phys. Rev. Lett.* **116**, 233001 (2016).
- [173] D. I. Mihaylov, V. V. Karasiev, and S. X. Hu, *Phys. Rev. B* **101**, 245141 (2020).
- [174] V. V. Karasiev, D. I. Mihaylov, and S. X. Hu, *Phys. Rev. B* **105**, L081109 (2022).
- [175] P. Cheng, X. Yang, X. Zhang, Y. Wang, S. Jiang, and A. F. Goncharov, *J. Chem. Phys.* **152**, 244502 (2020).
- [176] M. D. Knudson and M. P. Desjarlais, *Phys. Rev. Lett.* **118**, 035501 (2017).
- [177] A. Bergermann and R. Redmer, *Phys. Rev. B* **108**, 085101 (2023).
- [178] J. Heyd and G. E. Scuseria, *J. Chem. Phys.* **120**, 7274 (2004).
- [179] J. P. Perdew, K. Burke, and M. Ernzerhof, *Phys. Rev. Lett.* **77**, 3865 (1996).
- [180] J. Sun, A. Ruzsinszky, and J. P. Perdew, *Phys. Rev. Lett.* **115**, 036402 (2015).

- [181] J. Heyd, J. E. Peralta, G. E. Scuseria, and R. L. Martin, *J. Chem. Phys.* **123**, 174101 (2005).
- [182] J. Heyd, G. E. Scuseria, and M. Ernzerhof, *J. Chem. Phys.* **118**, 8207 (2003).
- [183] J. Heyd and G. E. Scuseria, *J. Chem. Phys.* **121**, 1187 (2004).
- [184] B. J. Alder and T. E. Wainwright, *J. Chem. Phys.* **27**, 1208 (1957).
- [185] B. J. Alder and T. E. Wainwright, *J. Chem. Phys.* **31**, 459 (1959).
- [186] S. Nosé, *J. Chem. Phys.* **81**, 511 (1984).
- [187] W. G. Hoover, *Phys. Rev. A* **31**, 1695 (1985).
- [188] W. Lorenzen, *Phase Transitions in Hydrogen-Helium Mixtures*, Ph.D. thesis, University of Rostock (2012).
- [189] G. Kresse and J. Hafner, *Phys. Rev. B* **49**, 14251 (1994).
- [190] G. Kresse and J. Furthmüller, *Phys. Rev. B* **54**, 11169 (1996).
- [191] G. Kresse and J. Furthmüller, *Comp. Mater. Sci.* **6**, 15 (1996).
- [192] P. P. Ewald, *Annalen der Physik* **369**, 253 (1921).
- [193] W. Nolting, *Theoretical Physics 1: Classical Mechanics* (Springer International Publishing, 2016).
- [194] M. E. Tuckerman, D. Marx, M. L. Klein, and M. Parrinello, *J. Chem. Phys.* **104**, 5579 (1996).
- [195] J. A. Barker, *J. Chem. Phys.* **70**, 2914 (2008).
- [196] P. H. Berens, D. H. J. Mackay, G. M. White, and K. R. Wilson, *J. Chem. Phys.* **79**, 2375 (1983).
- [197] J. G. Kirkwood, *J. Chem. Phys.* **3**, 300 (1935).
- [198] N. Nettelmann, A. Becker, B. Holst, and R. Redmer, *Astrophys. J.* **750**, 52 (2012).
- [199] S.-T. Lin, M. Blanco, and I. Goddard, William A., *J. Chem. Phys.* **119**, 11792 (2003).
- [200] M. French, M. P. Desjarlais, and R. Redmer, *Phys. Rev. E* **93**, 022140 (2016).
- [201] O. Sugino and R. Car, *Phys. Rev. Lett.* **74**, 1823 (1995).
- [202] M. A. Morales, C. Pierleoni, and D. M. Ceperley, *Phys. Rev. E* **81**, 021202 (2010).
- [203] D. Zubarev, V. Morozov, and G. Röpke, *Statistical Mechanics of Nonequilibrium Processes: Relaxation and hydrodynamic processes* (Akademie Verlag, 1996).

- [204] R. Kubo, *J. Phys. Soc. Jap.* **12**, 570 (1957).
- [205] R. Kubo, M. Yokota, and S. Nakajima, *J. Phys. Soc. Jap.* **12**, 1203 (1957).
- [206] D. A. Greenwood, *Proc. Phys. Soc.* **71**, 585 (1958).
- [207] B. Holst, M. French, and R. Redmer, *Phys. Rev. B* **83**, 235120 (2011).
- [208] J. Hafner, *J. Comput. Chem.* **29**, 2044 (2008).
- [209] M. Gajdoš, K. Hummer, G. Kresse, J. Furthmüller, and F. Bechstedt, *Phys. Rev. B* **73**, 045112 (2006).
- [210] M. French and R. Redmer, *Phys. Plasmas* **24**, 092306 (2017).
- [211] B. Holst, R. Redmer, and M. P. Desjarlais, *Phys. Rev. B* **77**, 184201 (2008).
- [212] D. Knyazev and P. Levashov, *Comp. Mater. Sci.* **79**, 817 (2013).
- [213] M. French, G. Röpke, M. Schörner, M. Bethkenhagen, M. P. Desjarlais, and R. Redmer, *Phys. Rev. E* **105**, 065204 (2022).
- [214] A. Bergermann, M. French, M. Schöttler, and R. Redmer, *Phys. Rev. E* **103**, 013307 (2021).
- [215] A. Bergermann, M. French, and R. Redmer, *Phys. Chem. Chem. Phys.* **23**, 12637 (2021).
- [216] A. Bergermann, M. French, and R. Redmer, “Ab initio calculation of the miscibility diagram for mixtures of hydrogen and water,” (2024), submitted to *Phys. Rev. Lett.*
- [217] U. von Zahn, D. M. Hunten, and G. Lehmacher, *J. Geophys. Res.* **103**, 0148 (1998).
- [218] M. Preising, W. Lorenzen, A. Becker, R. Redmer, M. D. Knudson, and M. P. Desjarlais, *Phys. Plasmas* **25**, 012706 (2018).
- [219] N. Nettelmann, B. Holst, A. Kietzmann, M. French, R. Redmer, and D. Blaschke, *Astrophys. J.* **683**, 1217 (2008).
- [220] W. B. Hubbard and B. Militzer, *Astrophys. J.* **820**, 80 (2016).
- [221] F. Soubiran and B. Militzer, *Astrophys. J.* **806**, 228 (2015).
- [222] H. M. Hulburt and J. O. Hirschfelder, *J. Chem. Phys.* **9**, 61 (1941).
- [223] W. H. Stockmayer, *J. Chem. Phys.* **9**, 398 (1941).
- [224] E. Schwegler, G. Galli, F. m. c. Gygi, and R. Q. Hood, *Phys. Rev. Lett.* **87**, 265501 (2001).

- [225] M. French, T. R. Mattsson, N. Nettelmann, and R. Redmer, *Phys. Rev. B* **79**, 054107 (2009).
- [226] O. Redlich and A. T. Kister, *Ind. Eng. Chem.* **40**, 345 (1948).
- [227] T. Kimura and M. Murakami, *J. Chem. Phys.* **158**, 134504 (2023).
- [228] J.-F. Lin, E. Gregoryanz, V. V. Struzhkin, M. Somayazulu, H.-k. Mao, and R. J. Hemley, *Geophys. Res. Lett.* **32** (2005).
- [229] E. Schwegler, M. Sharma, F. Gygi, and G. Galli, *Natl. Acad. Sci. Lett.* **39**, 14779 (2008).
- [230] R. Redmer, T. R. Mattsson, N. Nettelmann, and M. French, *Icarus* **211**, 798 (2011).
- [231] J.-A. Queyroux, J.-A. Hernandez, G. Weck, S. Ninet, T. Plisson, S. Klotz, G. Garbarino, N. Guignot, M. Mezouar, M. Hanfland, J.-P. Itié, and F. Datchi, *Phys. Rev. Lett.* **125**, 195501 (2020).
- [232] B. Schwager, L. Chudinovskikh, A. Gavriiliuk, and R. Boehler, *J. Phys. Condens. Matter* **16**, S1177 (2004).
- [233] B. Schwager and R. Boehler, *High Press. Res.* **28**, 431 (2008).
- [234] L. Zhang, H. Wang, R. Car, and W. E, *Phys. Rev. Lett.* **126**, 236001 (2021).
- [235] T. Kimura, Y. Kuwayama, and T. Yagi, *J. Chem. Phys.* **140**, 074501 (2014).
- [236] T. M. Seward and E. U. Franck, *Bunsenges. Phys. Chem.* **85**, 2 (1981).
- [237] J.-C. Mareschal and C. Jaupart, *Geophys. Monogr. Ser.* **164**, 61 (2006).
- [238] R. Turnbull, M. Hanfland, J. Binns, M. Martinez-Canales, M. Frost, M. Marques, R. T. Howie, and E. Gregoryanz, *Nature Commun.* **9**, 4717 (2018).
- [239] S. Jiang, N. Holtgrewe, S. S. Lobanov, F. Su, M. F. Mahmood, R. S. McWilliams, and A. F. Goncharov, *Nature Commun.* **9**, 2624 (2018).
- [240] Z. Fu, Q. Chen, Z. Li, J. Tang, W. Zhang, W. Quan, J. Li, J. Zheng, and Y. Gu, *High Energy Density Phys.* **31**, 52 (2019).
- [241] Y.-S. Lan, Z.-Q. Wang, L. Liu, G.-J. Li, H.-Y. Sun, Z.-J. Fu, Y.-J. Gu, G. Yang, L.-N. Li, Z.-G. Li, Q.-F. Chen, and X.-R. Chen, *Phys. Rev. B* **103**, 144105 (2021).
- [242] W. Lorenzen, B. Holst, and R. Redmer, *Phys. Rev. B* **84**, 235109 (2011).
- [243] S. Mazevet, J. D. Kress, L. A. Collins, and P. Blottiau, *Phys. Rev. B* **67**, 054201 (2003).
- [244] M. French, A. Becker, W. Lorenzen, N. Nettelmann, M. Bethkenhagen, J. Wicht, and R. Redmer, *Astrophys. J. Suppl. Ser.* **202**, 5 (2012).

- [245] M. Guarguaglini, J.-A. Hernandez, T. Okuchi, P. Barroso, A. Benuzzi-Mounaix, M. Bethkenhagen, R. Bolis, E. Brambrink, M. French, Y. Fujimoto, R. Kodama, M. Koenig, F. Lefevre, K. Miyanishi, N. Ozaki, R. Redmer, T. Sano, Y. Umeda, T. Vinci, and A. Rava-sio, *Scient. Rep.* **9**, 10155 (2019).
- [246] R. Chau, A. C. Mitchell, R. W. Minich, and W. J. Nellis, *J. Chem. Phys.* **114**, 1361 (2001).
- [247] M. Bastea, *Phys. Rev. Lett.* **92**, 129601 (2004).

Curriculum vitae

Education:

- 04.2020–present **P. hD.**, *University Rostock*
Supervisor: Prof. Dr. Ronald Redmer
- 2018–2020 **Master of Science in Physics**, *University of Rostock*, Final grade: 1.5,
Topic: Gibbs-Ensemble Monte-Carlo Simulations for Binary Mixtures
- 2017–2018 **Study abroad**, *University of Technology Sydney*
- 2013–2017 **Bachelor of Science in Physics**, *University of Rostock*, Final grade: 2.7,
Topic: Fiber Fuse
- 2010–2013 **Abitur**, *Cuno Berufskolleg*, Final grade: 1.6
- 2004–2010 **Realschule**, *St. Jacobus Realschule Breckerfeld*
- 2000–2004 **Grundschule**, *Grundschule Breckerfeld*

Teaching at the University of Rostock:

- 08.2023–present **Co-advisor of a master student (L. Kleindienst)**
Topic: Nonmetal-to-metal transition in hydrogen using density functional theory and the Heyd–Secuseria–Ernzerhof functional
- 04.2023–09.2023 **Co-advisor of a bachelor student (T. Wagner)**
Analysing the structure of *ab initio* simulations for water and ethanol mixtures at high pressure and temperature
- summer term 2023 **Seminar**, experimental physics II for teachers
- winter term 2022 **Lab course**, experimental physics for medicine students
- summer term 2022 **Seminar**, experimental physics II for teachers
- winter term 2021 **Seminar**, experimental physics I for teachers
- summer term 2021 **Seminar**, experimental physics II for teachers
- winter term 2020 **Seminar**, experimental physics I for teachers
- summer term 2020 **Seminar**, math for teachers
- winter term 2019 **Lab course**, experimental physics for medicine students
- winter term 2019 **Seminar**, experimental physics for medicine students
- summer term 2018 **Lab course**, experimental physics for chemist students
- winter term 2017 **Lab course**, experimental physics for medicine students
- winter term 2017 **Seminar**, experimental physics for medicine students

List of publications:

1. **Nonmetal-to-metal transition in dense fluid nitrogen at high pressure** (A. Bergermann and R. Redmer, Phys. Rev. B 108, 085101, 2023)
2. **Diamond formation kinetics in shock-compressed C-H-O samples recorded by small-angle x-ray scattering and x-ray diffraction** (Z. He, M. Rödel, J. Lüttger, A. Bergermann, M. Bethkenhagen, T. Cowan, M. French, E. Galtier, A. Gleason, G. Glenn, S. Glenzer, Y. Inubushi, N. Hartley, J. Hernandez, B. Heuser, O. Humphries, N. Kamimura, K. Katagiri, D. Khaghani, H. Lee, E. McBride, K. Miyanishi, B. Nagler, B. Ofori-Okai, N. Ozaki, S. Pandolfi, C. Qu, D. Ranjan, R. Redmer, C. Schoenwaelder, A. Schuster, M. Stevenson, K. Sueda, T. Togashi, T. Vinci, K. Voigt, J. Vorberger, M. Yabashi, T. Yabuuchi, L. Zinta, A. Ravasio, and D. Kraus, Science Advances 8, 35, 2022)
3. **Gibbs-ensemble Monte-Carlo simulation of H₂-He mixtures** (A. Bergermann, M. French, M. Schöttler, and R. Redmer, Phys. Rev. E 103, 013307, 2021)
4. **Gibbs-ensemble Monte-Carlo simulation of H₂-H₂O mixtures** (A. Bergermann, M. French, and R. Redmer, Phys. Chem. Chem. Phys., 12637-12643, 2021)
5. **Ab Initio Calculation of the Miscibility Diagram of Mixtures of Hydrogen and Water** (A. Bergermann, M. French, and R. Redmer, submitted to Phys. Rev. Lett.)
6. **Nanodiamond stability upon shock release from Hugoniot state of polyethylene terephthalate** (B. Heuser, A. Bergermann, M. Stevenson, D. Ranjan, Z. He, J. Lüttger, S. Schumacher, M. Bethkenhagen, A. Descamps, E. Galtier, A. Gleason, D. Khangani, G. Glenn, S. Glenzer, Y. Inubushi, N. Hartley, J. Hernandez, O. Humphries, N. Kamimura, K. Katagiri, H. Lee, E. McBride, K. Miyanishi, B. Nagler, B. Ofori-Okai, N. Ozaki, S. Pandolfi, C. Qu, R. Redmer, C. Schownälder, K. Sueda, T. Togashi, M. Yakashi, T. Yabuuchi, L. Zinta, A. Ravasio, and D. Kraus, submitted to Sci. Rep.)
7. **Mixture of Hydrogen and Methane under planetary interior conditions** (A. Roy, A. Bergermann, and R. Redmer, submitted to Phys. Chem. Chem. Phys.)

Conference contributions (talks):

1. **Demixing in binary mixtures under planetary temperature and pressure conditions**, USA: Rochester (NY) (2023)
2. **Miscibility gap in hydrogen and water mixtures**, USA: SLAC (2023)
3. **Miscibility gap in hydrogen and water mixtures**, Z-Workshop, USA: Albuquerque (2023)
4. **Miscibility gap in hydrogen and water mixtures**, Matter in extreme conditions, Israel: Jerusalem (2023)
5. ***Ab initio* simulations for hydrogen-water mixtures**, HP4 Meeting, Belgium: Brussels (2022)
6. ***Ab initio* simulations for hydrogen-water mixtures**, International DFT Workshop, CASUS, Görlitz (2022)
7. **Gibbs-ensemble Monte-Carlo simulations for binary mixtures**, CMWS Water Days, Hamburg (2022)
8. **Gibbs-ensemble Monte-Carlo simulations for hydrogen and water mixtures**, 17th International Conference on the Physics of Non-Ideal Plasmas, Dresden (2021)
9. **Gibbs-ensemble Monte-Carlo simulations for binary mixtures**, Graduate Network Workshop, Life, Light & Matter Department, Rostock (2021)

Conference contributions (poster):

1. **Miscibility gap in hydrogen and water mixtures**, HP4 Meeting, Rostock (2023)
2. **Miscibility gap in hydrogen and water mixtures**, CMWS Water Days, Hamburg (2023)

Acknowledgments

Während der Anfertigung meiner Promotionsarbeit haben mich viele großartige Menschen begleitet. Zuerst möchte ich meinem Doktorvater Prof. Dr. Ronald Redmer danken, der mir nicht nur die Möglichkeit zur Promotion eröffnete, sondern mich zu jedem Zeitpunkt hervorragend betreute. Neben seiner fachlichen Unterstützung möchte ich mich auch für viele bereichernde Gespräche über Hansa Rostock bedanken. Ein besonderer Dank gebührt ihm für die einzigartigen Gelegenheiten, nach Frankreich, Belgien, Israel und in die USA reisen zu dürfen.

Als nächstes möchte ich mich bei Martin French bedanken. Ohne sein umfassendes Wissen und seine wertvollen Inputs wäre die Bearbeitung eines so komplexen Themas nicht möglich gewesen. Martin Preising sei gedankt für die großartige Zeit im Adminbüro und sein Verständnis für mein gelegentliches Chaos. Ebenso möchte ich den anderen Mitgliedern der AG Max Schörner, Clemens Kellermann, Anna Julia Poser, Uwe Kleinschmidt, Argha Roy, Thomas Bornath, Wolf-Dietrich Kreft, Maik und Olesya Wissing, Mandy Bethkenhagen, Sandeep Kumar, Waltraud Dulinski und Peggy Preuß danken. Diese Menschen haben die Zeit zu einer besonderen gemacht. Ein weiterer Dank geht an Manuel Schöttler der mich während meiner Masterarbeit betreut hat und mich für diese Arbeit begeistern konnte.

Während der Arbeit benötigte ich eine immense Menge an Rechenleistung und machte Gebrauch von den Clustern Titan und Haumea des ITMZ sowie von der Rechenleistung des HLRN-Verbunds. Hier möchte ich mich besonders bei den vielen Administratoren bedanken, die sich um die Wartung der Cluster kümmerten.

Ein herzlicher Dank geht an das Evangelische Studienwerk, das mich nicht nur finanziell unterstützte, sondern mir auch ideell von unschätzbarem Wert zur Seite stand.

Meinen Freunden möchte ich ebenfalls danken. Wir haben nicht nur eine großartige Zeit miteinander verbracht, sondern ich konnte mich auch immer auf sie verlassen. Ein großer Dank gilt für die einzigartige Chance, ehrenamtlich im ambulanten Hospizdienst tätig zu sein. Dort habe ich nicht nur wertvolle Erfahrungen gesammelt, sondern auch Freunde gefunden, die immer für mich da waren und mich unterstützt haben.

Der letzte Dank gebührt meiner Familie. Sie haben nicht nur immer an mich geglaubt, sondern haben mich überhaupt erst in die Lage versetzt, zu promovieren.

Selbstständigkeitserklärung

Ich versichere hiermit, dass ich die vorliegende Arbeit selbstständig verfasst und keine anderen als die angegebenen Quellen und Hilfsmittel benutzt habe. Ich versichere, dass die eingereichte elektronische Fassung mit den gedruckten Exemplaren übereinstimmt.

Rostock, 09.01.2024